Evolution and appearance of the inner regions of circumbinary discs

Kieran Hirsh

Université Claude Bernard Lyon 1

N° d'ordre NNT: 2021LYSE1192

THÈSE DE DOCTORAT DE L'UNIVERSITÉ DE LYON

opérée au sein de

l'Université Claude Bernard Lyon 1

École Doctorale ED 52

Physique et Astrophysique (PHAST)

Spécialité de doctorat : Astrophysique

Soutenue publiquement le 30/09/2021, par:

Kieran HIRSH

Evolution and Appearance of the Inner Regions of Circumbinary Discs

Évolution et Apparence des Régions Internes de Disques Circumbinaires

---

Devant le jury composé de:

KLEY, Wilhelm	Rapporteur
MADDISON, Sarah	Rapporteure
BENISTY, Myriam	Examinatrice
COURTOIS, Hélène	Examinatrice, Présidente du jury
GONZALEZ, Jean-François	Directeur de thèse

Abstract

Stars are born in swirling discs of gas and dust, and roughly half of all stars exists in binary systems. The presence of a binary companion in a disc is known to open a large cavity in the inner region, however the exact nature of how this occurs is not fully known. Moreover, resolving a binary companion remains a challenging observational problem, and there exists a number of discs with observed cavities and as yet no resolved binary, leading to difficulties in inferring the presence of these companions.

To investigate the cavity opening process in a circumbinary disc I perform a suite of 3D Smoothed Particle Hydrodynamics simulations using the code `PHANTOM`. I alter the binary orbital eccentricity, binary mass ratio, disc scale height, and the mutual inclination between the binary and the disc to understand how each of these affect the cavity over the course of 1,000 binary orbits. I find that a cavity is quickly opened on a dynamical timescale while its long-term size is set on a viscous timescale, with the final size depending on both binary and disc properties.

I then compute synthetic observations using the 3D radiative transfer code MCFOST in an attempt to find observable signatures of the companion. I find that the radial motion imparted on the disc by the companion is detectable in the dynamic signatures. I also develop a metric to quantify the asymmetry in our observations and find that circumbinary discs are at least 3 times more asymmetric than single-star discs. Thus I have developed two methods to indirectly infer the presence of a binary companion in the case when it cannot be directly observed.

Résumé

Les étoiles naissent dans des disques tourbillonnants de gaz et de poussière, et environ la moitié de toutes les étoiles existent dans des systèmes binaires. La présence d'un compagnon binaire dans un disque est connue pour ouvrir une grande cavité dans la région interne, mais la nature exacte de la façon dont cela se produit n'est pas entièrement connue. De plus, la détection d'un compagnon binaire reste un problème d'observation difficile, et il existe un certain nombre de disques avec des cavités observées et encore aucune binaire détectée, ce qui pose des difficultés pour déduire la présence de ces compagnons.

Pour étudier le processus d'ouverture d'une cavité dans un disque circumbinaire, j'effectue une suite de simulations 3D utilisant le formalisme Smoothed Particle Hydrodynamics avec le code PHANTOM. Je modifie l'excentricité orbitale de la binaire, le rapport de masse des deux étoiles, l'échelle de hauteur du disque et l'inclinaison mutuelle entre la binaire et le disque pour comprendre comment chacun de ces paramètres affecte la cavité au cours de 1 000 orbites de la binaire. Je trouve qu'une cavité est rapidement ouverte sur une échelle de temps dynamique tandis que sa taille à long terme est définie sur une échelle de temps visqueuse, la taille finale dépendant à la fois des propriétés de la binaire et du disque.

Je calcule ensuite des observations synthétiques en utilisant le code de transfert radiatif 3D MCFOST pour tenter de trouver des signatures observables du compagnon. Je constate que le mouvement radial imprimé au disque par le compagnon est détectable dans les signatures dynamiques. Je développe également une métrique pour quantifier l'asymétrie dans nos observations et trouve que les disques circumbinaires sont au moins un demi-ordre de grandeur plus asymétriques que les disques autour d'une seule étoile. Ainsi, j'ai développé deux méthodes pour inférer indirectement la présence d'un compagnon binaire dans le cas où il ne peut pas être observé directement.

Contents

Acknowledgements

As this thesis represents the last major work of my career in astrophysics I want to thank everyone who helped me along this journey, starting with Milorad Cerovac, my high school physics teacher. Thanks, Milo, for having such passion for your work, for your support on so many after hours activities, and for making the astrophysics module the most enjoyable classes in all my time in high school. Were it not for those classes my life surely would've followed a different path. To Daniel Price, my undergraduate project honours supervisor. Thanks, Dan, for taking me on for that undergraduate project when I wasn't even sure I was up to the task. And to Jean-François Gonzalez, my PhD supervisor. Thanks, Jeff, for constantly forcing me out of my comfort zone, especially when if comes to presenting my work at conferences to an international crowd. This has helped me to become more confident in my own abilities and forced me to see the value in my work that I struggled to see before.

To anyone I've ever shared an office with these past 5 years, thank you for making the day to day work as enjoyable as possible. Thanks for all the coffee breaks, lunch breaks, and random walks, and sorry for being such a distraction.

To my family, thanks for always having my back and being supportive of all the decisions I've made along this journey, even when that decision was to move halfway across the world.

To all my Australian friends: The Sunday Crew, The Study Group, and my honours cohort. Thanks for reminding me during my time away that gone does not mean forgotten.

To all my French friends thanks for immediately making me feel welcome and for helping me with the infinite red tape upon arrival. To the Astro Bitches, thanks for all the free alcohol we won together. To everyone at the obs, thanks for all the games of babyfoot. To everyone at the ENS, thanks for making my weekly visits something to genuinely look forward too. And to Antoine, thanks for the countless games of Magic le Gathering.

Thank you to all the international friends I made during my PhD, the astrophysics community is truly what makes working in this field as enjoyable as it is. To the Italian team, thanks for making Milan the best European city outside of Lyon (until you all moved elsewhere). To everyone I met during workshops, conferences, and secondments, of which there are too many to name, thanks for making these events the most enjoyable part of my PhD. Be it a couple of days to a couple of months, I have enjoyed all my excursions away from Lyon and it is thanks to you. To Camilo, thanks for helping me find my feet upon arrival in Santiago, and extra thanks for everything you did during the most stressful week of my life as I tried to leave during the Covid outbreak.

To all the friends with whom I made it through the Covid lockdowns, thanks for pulling me through. To the REAL Gaming Club and Room 125 et al., thanks for the weekly games sessions that allowed me to leave my apartment without violating lockdown laws. And to the Jackal Den, thanks for being the best damn online community ever! I don't want to imagine what the past year would've been like had I not decided to do something different and join an unassuming discord server. Thanks for all the sessions of MtG, Jackbox, Gartic Phone, Slay the Spire, Apex, and more. Special thanks, of course, go to Binx, Duck & Fish, Daphne & Lily, Thespis, Scully, Figaro & Gemini, Aslan, Bandit, and Merry & Pippin.

Finally, to Arnaud, thanks for offering me warm water.

Chapter 1

Introduction

1.1 Star Formation

Molecular clouds are the birthplaces of stars. These large regions, up to ~ 100 parsecs across, are comprised mostly of gas, with a small fraction of dust, typically $\sim 1\%$ (Murray, 2011). The evolution of these clouds is driven by the gravitational force, which acts to collapse the cloud, and restorative forces, most notably thermal pressure. By considering the timescales at which these forces act Jeans (1902) was able to find the conditions in which a star can form. Material acting only under gravity falls on a free-fall time:

$$t_{\rm ff} \simeq \frac{1}{\sqrt{\mathrm{G}\rho}}, \tag{1.1}$$

where G is the gravitational constant and ρ is the density of the molecular cloud. Thermal pressure acts on a sound crossing time:

$$t_{\rm sound} \simeq \frac{R}{c_{\rm s}}, \tag{1.2}$$

where R is the radius over which the force is acting and $c_{\rm s}$ is the sound speed. When the free-fall time is less than the sound crossing time the cloud undergoes gravitational collapse. By setting $t_{\rm ff} < t_{\rm sound}$ we can find the Jeans length $\lambda_{\rm J}$, the length scale above which a cloud is unstable to gravity:

$$\lambda_{\rm J} \gtrsim \frac{c_{\rm s}}{\sqrt{\mathrm{G}\rho}}, \tag{1.3}$$

and corresponding Jeans mass $m_{\rm J}$, the mass scale above which a cloud is unstable to gravity:

$$M_{\rm J} \gtrsim \frac{c_{\rm s}^3}{\sqrt{\mathrm{G}^3\rho}}. \tag{1.4}$$

The collapsing material leads to an increasing density until thermonuclear fusion begins and a protostar, also known as a young stellar object (YSO), is formed. Conservation

of angular momentum implies that the system expands radially to compensate for the momentum lost by the in-falling material, leading to the formation of a thin accretion disc surrounding the protostar.

1.2 Classification of Young Stellar Objects

Historically, spatially resolved observations of YSOs was difficult, if not entirely impossible, so their classification was determined by their spectral energy distribution (SED), a measure of the flux as a function of wavelength or frequency. While the protostar emits light mainly in the visible spectrum any of this light that is absorbed by the surrounding gas and dust will be re-emitted in the infrared (IR). Hot material closest to the protostar will emit in the near-IR, while the cooler material at larger radii will emit at longer wavelengths, in the far-IR. Thus the slope of the SED spectrum in the IR can give information about the morphology and evolution of these YSOs. We can quantify the slope of the SED in the IR by the parameter

$$\alpha_{\rm IR} \equiv \frac{\Delta \log(\lambda F_\lambda)}{\Delta \lambda}, \tag{1.5}$$

the value of which can be used to classify the YSO as one of four classes (Lada and Wilking, 1984; Andre and Montmerle, 1994) (see Figure 1.1):

- **Class 0:** the SED lies fully in the far-IR part of the spectrum, with little to no emission within the near-IR and $\alpha_{\rm IR} = 0.0$.
- **Class I:** the SED in the near- and mid-IR is nearly flat, with $-0.3 \leq \alpha_{\rm IR} \leq 0.0$.
- **Class II:** the majority of the SED falls within the near- and mid-IR, with a steeper slope of $-1.5 \leq \alpha_{\rm IR} \leq -0.3$.
- **Class III:** the stellar photosphere is the only major contributor to the SED, which now has $\alpha_{\rm IR} < 1.6$.

Each of these classes corresponds to a different evolutionary stage of a YSO from a molecular cloud to a pre-main sequence star (Adams et al., 1987). Class 0 corresponds to the earliest stages of star formation, during which a star is deeply embedded in an optically thick cloud. At this stage neither the star nor the disc are visible at near- and mid-IR wavelengths, and the only contribution to the SED comes from the far-IR emissions of the envelope. The earliest detectable discs are class I sources. The disc is still embedded in a cloud of gas and dust, thus a significant far-IR emission from the envelope is still detectable. At this stage high velocity outflows, on the order of 100 km s^{-1}, are ejected

from close to the protostar as a consequence of the conservation of angular momentum. During the class II stage the envelope has been largely accreted and the remaining star and disc are clearly visible in observations. This corresponds to a classical T Tauri star (Joy, 1945), the archetypal protoplanetary disc, and it is this class which will be the focus of this thesis. It is during this stage that planet formation begins, so knowledge of the structures present in these discs is a highly active area of research. A number of theories of planet formation exist, such as gravitational instability (Toomre, 1964; Goldreich and Ward, 1973) and core accretion (Mizuno, 1980; Pollack et al., 1996) to name the two most prominent, however these are not the subject of this thesis. Over time the gas disc is depleted and all that's left is a pre-main sequence star and dust disc, also known as a debris disc. The emission from the dust is faint in these late stages, giving rise to the typical class III object SED as that of a pre-main sequence stellar photosphere.

1.3 Accretion Discs

1.3.1 Evolution of Surface Density

The evolution of an accretion disc was analysed by Lynden-Bell and Pringle (1974) & Pringle (1981) and can be understood by considering the conservation of mass and angular momentum. Working in cylindrical co-ordinates, the rate of change of mass within an annulus between radius R and $R + \Delta R$ is given by

$$\frac{\partial}{\partial t}(2\pi R \Delta R \Sigma) = 2\pi R \Sigma(R) v_R(R) - 2\pi (R + \Delta R)\Sigma(R + \Delta R) v_R(R + \Delta R), \tag{1.6}$$

where Σ is the surface density and v_R is the radial velocity of the gas in the disc. Taking the limit for small ΔR and rearranging gives

$$R\frac{\partial \Sigma}{\partial t} + \frac{\partial}{\partial R}(R\Sigma v_R) = 0. \tag{1.7}$$

Conservation of angular momentum, again in the small ΔR limit, gives

$$R\frac{\partial}{\partial t}(R^2 \Omega \Sigma) + \frac{\partial}{\partial R}(R^2 \Omega \cdot R\Sigma v_R) = \frac{1}{2\pi}\frac{\partial G}{\partial R}, \tag{1.8}$$

where Ω is the angular velocity of the gas and G is the torque acted on the annulus by neighbouring annuli. For a viscous fluid this torque is

$$G = 2\pi R \cdot \nu \Sigma R \frac{d\Omega}{dR} \cdot R, \tag{1.9}$$

where ν is the kinematic viscosity. Combining Eq 1.6 and Eq 1.8, and assuming a Keplerian potential ($\Omega \propto R^{-3/2}$), gives the evolution of the surface density of a geometrically thin disc as

$$\frac{\partial \Sigma}{\partial t} = \frac{3}{R}\frac{\partial}{\partial R}\left(R^{1/2}\frac{\partial}{\partial R}(\nu \Sigma R^{1/2})\right). \tag{1.10}$$

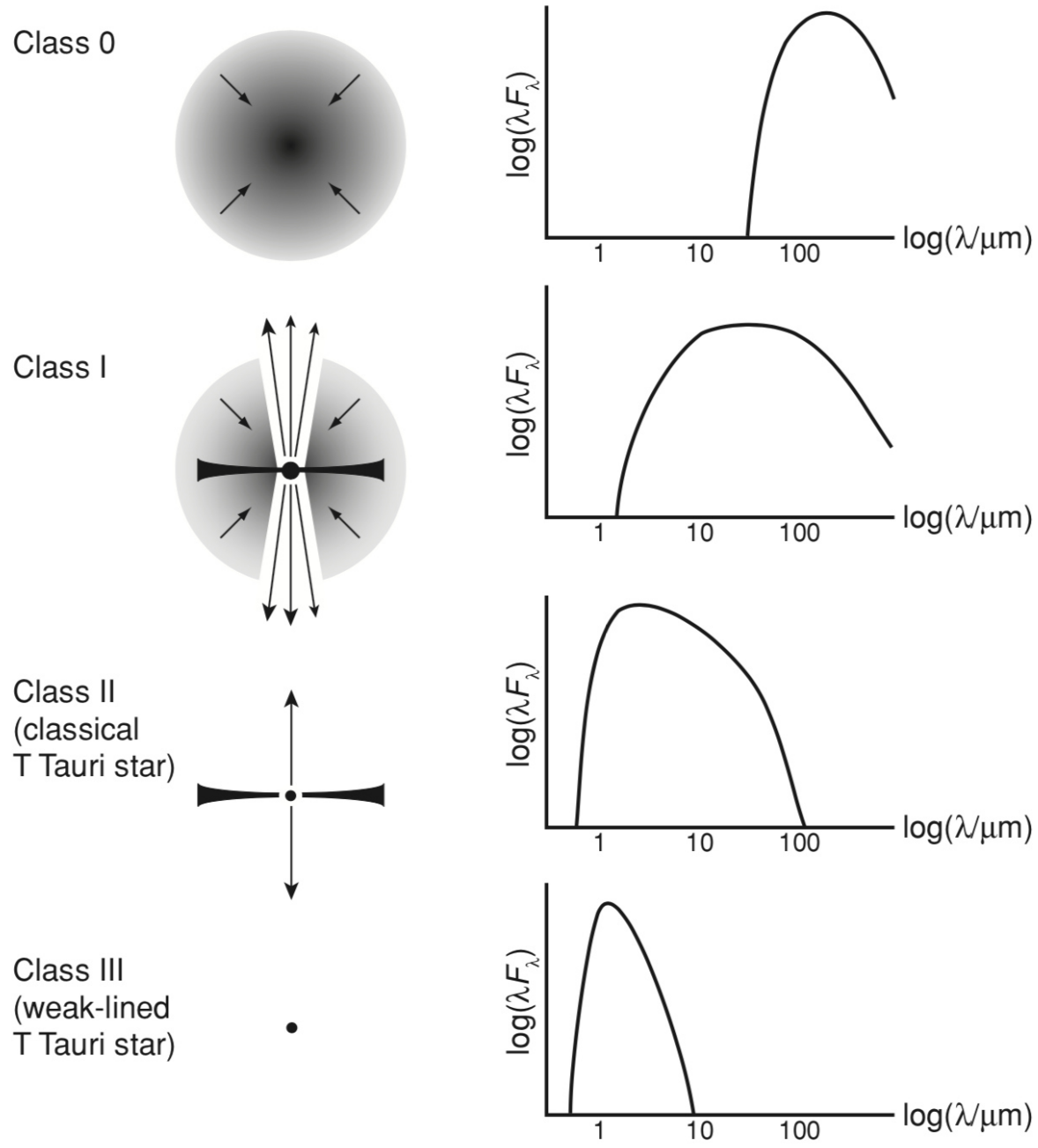

Figure 1.1: Classification of young stellar objects from their spectral energy distributions. (source: Armitage, 2010)

One solution to Equation 1.10 is the Green's function solution (Lynden-Bell and Pringle, 1974; Pringle, 1981). We start by considering a ring of mass m, initially at R_0, with an initial surface density profile

$$\Sigma(R, t = 0) = \frac{m}{2\pi R_0}\delta(R - R_0), \tag{1.11}$$

where $\delta(R - R_0)$ is the Dirac delta function. If we take ν = constant this leads to a

solution in the form

$$\Sigma(x,\tau) = \frac{m}{\pi R_0^2}\frac{1}{x^{1/4}\tau} exp\left(-\frac{1+x^2}{\tau}\right) I_{1/4}\left(\frac{2x}{\tau}\right), \tag{1.12}$$

given in terms of the dimensionless radius $x \equiv R/R_0$ and dimensionless time $\tau \equiv 12\nu t R_0^{-2}$, where $I_{1/4}$ is the modified Bessel function. This solution is plotted in Figure 1.2 and describes the spreading effect of viscosity on the ring over time. Most of the material falls inwards and since the specific angular momentum, h, for a circular object is given by $h = R^2\Omega \propto R^{1/2}$ the material loses angular momentum as it falls inwards. To conserve angular momentum a small tail of material must move outwards. Eventually the majority of the material collapses to the origin while all the angular momentum is carried to infinite radius by a vanishingly small mass.

The Green's function solution allows us to see the general behaviour of the material in the disc under the effects of viscosity, though it is of limited use since discs do not initially contain all their mass in a single ring. More illuminating is the self-similar solution, also developed by Lynden-Bell and Pringle (1974). This time we take $\nu = r^\gamma$ and consider a disc with an initial surface density profile

$$\Sigma(t=0) = \frac{C}{3\pi\nu_1\tilde{x}^\gamma}\exp\left(-\tilde{x}^{(2-\gamma)}\right). \tag{1.13}$$

corresponding to a steady-state solution for this viscosity law out to some radius, R_1, with an exponential cut-off at larger radii, where C is a normalisation constant, $\tilde{x} \equiv R/R_1$ and $\nu_1 \equiv \nu(R_1)$. The self-similar solution is then given by:

$$\Sigma(\tilde{x},\tilde{\tau}) = \frac{C}{3\pi\nu_1\tilde{x}^\gamma}\tilde{\tau}^{(\gamma-5/2)/(2-\gamma)}\exp\left(-\frac{\tilde{x}^{(2-\gamma)}}{\tilde{\tau}}\right), \tag{1.14}$$

where

$$\tilde{\tau} \equiv \frac{t}{t_s} + 1 \tag{1.15}$$

and

$$t_s \equiv \frac{1}{3(2-\gamma)^2}\frac{R_1^2}{\nu_1}. \tag{1.16}$$

This solution is plotted for the case where $\gamma = 1$ in Figure 1.3 and shows the disc losing mass over time as material is accreted due to viscosity. The outer edge of the disc also expands outwards to compensate for the loss of angular momentum from the in-falling material. This is reminiscent of the Green's function solution, with the majority of the material falling inwards while a small tail travels outwards.

1.3.2 Scale Height

The height H of the disc is set by the balance of gravitational forces and the pressure gradient in the vertical direction. If we assume that the disc mass is negligible compared

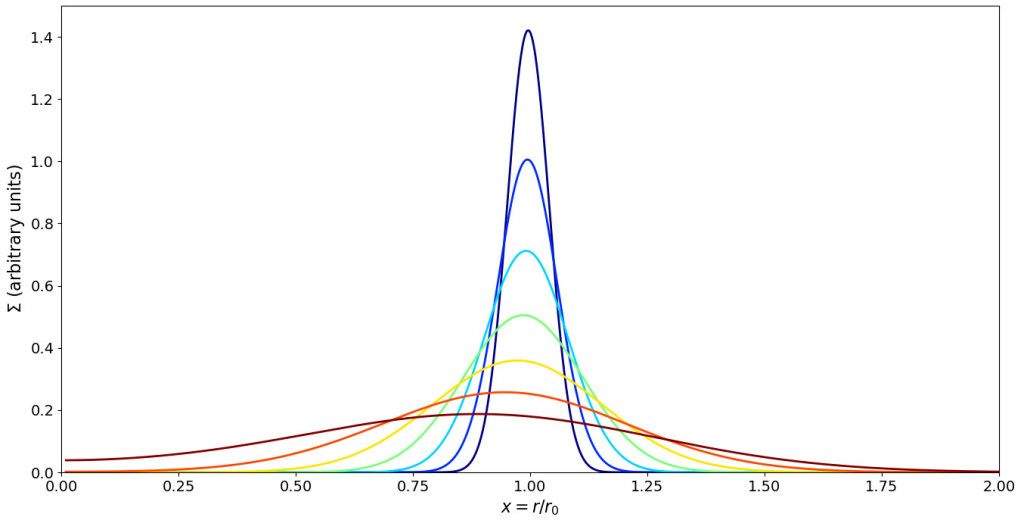

Figure 1.2: Green's function solution showing the evolution of a ring of mass m initially at $r = r_0$ under the effects of viscosity. From top to bottom the curves show the ring at different dimensionless time $\tau = 12\nu t/r_0^2$ for $\tau = 0.004$, 0.008, 0.016, 0.032, 0.064, 0.128 and 0.256.

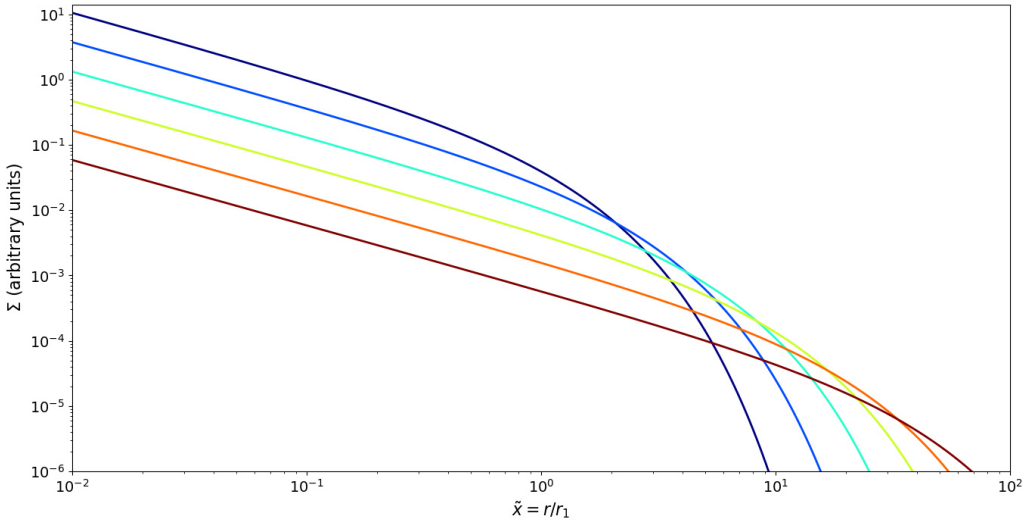

Figure 1.3: Self-similar solution showing the evolution of a disc with viscosity $\nu \propto r$ and a surface density profile corresponding to that of a steady-state disc at small radii with an exponential cut-off at large radii. From top to bottom the curves show the disc dimensionless times $\tilde{\tau} = 1$, 2, 4, 8, 16 and 32.

to the stellar mass, $M_{\rm disc} \ll M_*$, then the vertical acceleration due to gravity in the

vertical direction becomes

$$g_z = \frac{\mathrm{G}M_*}{R^2+z^2}\frac{z}{\sqrt{R^2+z^2}}. \tag{1.17}$$

For a vertically isothermal disc, $P = \rho c_\mathrm{s}^2$, where P is the pressure, the balance between the vertical pressure gradient $(1/\rho)(\mathrm{dP/dz})$ and the vertical acceleration due to gravity gives

$$c_\mathrm{s}^2\frac{\mathrm{d}\rho}{\mathrm{d}z} = -\frac{\mathrm{G}M_* z}{(R^2+z^2)^{3/2}}\rho. \tag{1.18}$$

This leads to a vertical density structure of the form

$$\rho = C\exp\left(\frac{\mathrm{G}M_*}{c_\mathrm{s}(R^2+z^2)^{1/2}}\right), \tag{1.19}$$

where C is a constant set by the density in the mid-plane. If we assume the disc thickness is a small fraction of the orbital radius we can write $g_z \simeq \Omega^2 z$, where $\Omega = \sqrt{\mathrm{G}M_*/R^3}$ is the Keplerian frequency. This assumption holds since the disc has a high surface area, allowing for efficient cooling which leads to low temperature which implies a thermal pressure low enough to only be able to support a thin disc. In this limit we obtain a vertical structure of the form

$$\rho = \rho_0\exp\left(-\frac{z^2}{2H}\right), \tag{1.20}$$

where ρ_0 is the mid plane density and H is the disc scale height, defined as

$$H \equiv \frac{c_\mathrm{s}}{\Omega}. \tag{1.21}$$

1.3.3 Viscous Evolution

Estimates of the accretion rates in protoplanetary discs give a lifetime of 10^7 yrs for all the material to be accreted onto the central star. Indeed, this estimate matches observational surveys suggesting that almost all stars have lost their discs by this age (see Figure 1.4). There must therefore be some efficient viscosity driving this momentum transport, the most common form of this is molecular viscosity which comes from collisions on a microscopic scale. Armitage (2007) found, however, that in the medium of protoplanetary discs this viscosity is on the order of $\sim 10^5$ cm^2 s^{-1}, giving a disc lifetime of 10^{13} yrs, 6 orders of magnitude longer than the lifetime of a disc and indeed longer than the age of the universe itself, thus the viscosity must come from another physical source.

One commonly suggested source is the magneto-rotational instability (MRI) (Balbus and Hawley, 1998), which occurs in ionised discs. A weakly magnetised flow is unstable whenever the angular velocity decreases with radius, that is instability occurs when $\mathrm{d}\Omega^2/\mathrm{dr} < 0$ (Balbus and Hawley, 1991). This condition is always met for Keplerian discs, making the MRI an easy instabiliy to invoke. The coupling of the gas and the magnetic

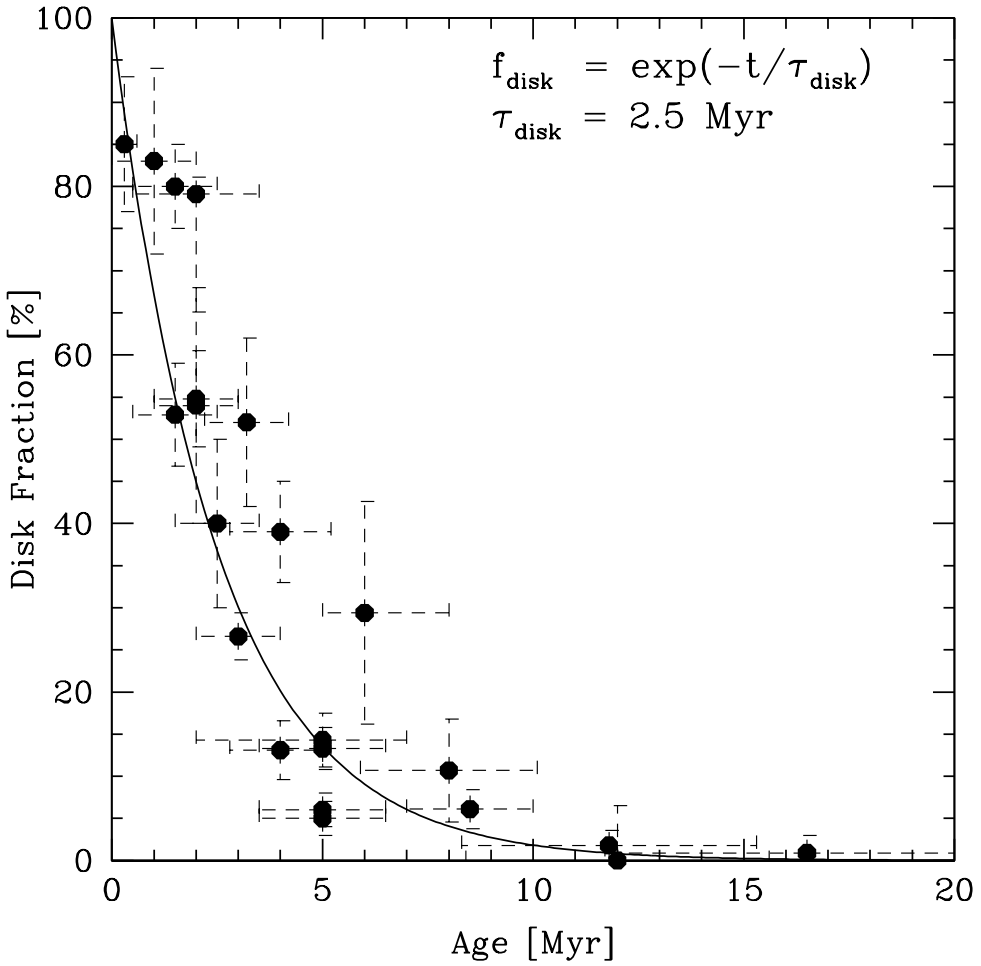

Figure 1.4: Disc fraction as a function of stellar age. After 10 Myr less that 2% of stars still have discs. (source: Mamajek, 2009)

field, however, requires a relatively high ionisation fraction and an optically thick disc can block stellar radiation, creating "dead zones" of unionised gas in the midplane, reducing the efficiency the MRI in these regions (Gammie, 1996).

A competing instability which requires no ionised material is the gravitational instability (GI) (Toomre, 1964). As the name suggest this occurs when a disc becomes unstable to its own self-gravity, inducing a disc-scale turbulence. The stability criterion is given by

$$Q \equiv \frac{c_{\rm s}\Omega}{\pi {\rm G}\Sigma} < 1. \tag{1.22}$$

If we take the disc mass as $M_{\rm disc} \simeq \pi R^2 \Sigma$ then we can rewrite this as

$$\begin{aligned} Q &\equiv \frac{M_*}{M_{\rm disc}} \frac{H}{R} < 1. \\ \frac{H}{R} &< \frac{M_{\rm disc}}{M_*}. \end{aligned} \tag{1.23}$$

This tells us that the GI is active when the ratio of the disc mass to the stellar mass is greater than the aspect ratio of the disc, typically on the order of 10^{-2}. However, a survey of the Taurus star forming region performed by Andrews et al. (2013) found that only about 20% of discs meet this criterion (see Figure 1.5), suggesting that the GI is not the source of momentum transport in the majority of discs.

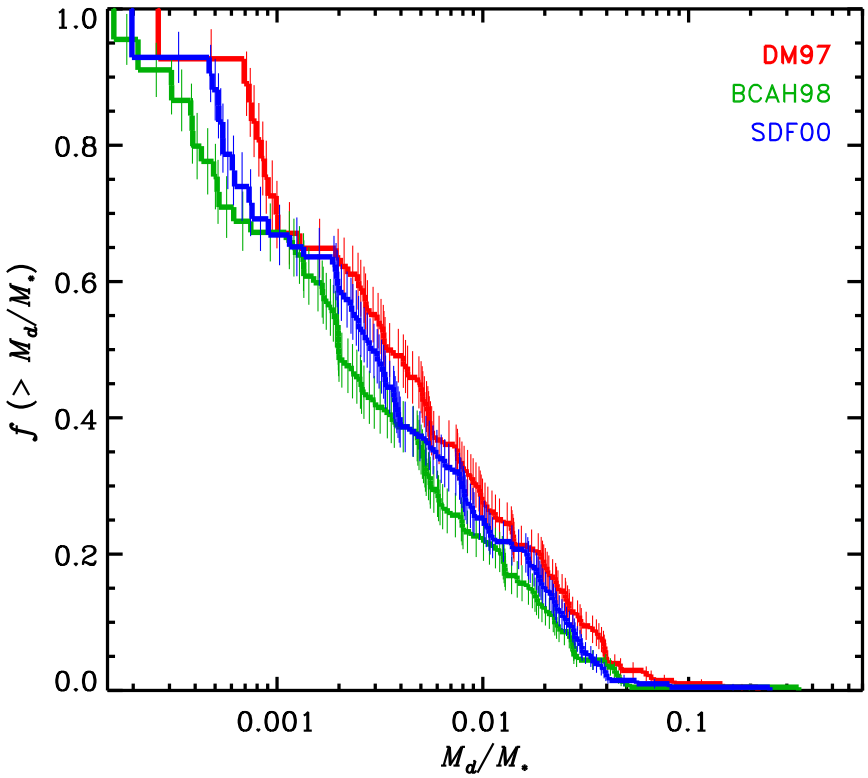

Figure 1.5: Cumulative distribution of disc-to-star mass ratios of discs in the Taurus star forming region. Only about 20% of T Tauri stars have a disc-to-star mass ratio greater than 10^{-2}. The red, green, and blue lines use data from D'Antona and Mazzitelli (1997), Baraffe et al. (1998), and Siess et al. (2000), respectively. (source: Andrews et al., 2013)

Since the physical source of the viscosity is an open question the common approach when modelling discs is to assume a turbulent viscosity while remaining agnostic to the source and approximating the effects on the fluid. This approximation was performed by Shakura and Sunyaev (1973) who considered the maximum scales on which this turbulent viscosity could act. The length scale of the turbulent motions can be no larger than the smallest scale in the disc, which is the disc scale height H. The velocities of these motions are limited to less than the sound speed c_s, since supersonic motions cause shocks which quickly dissipate velocities. Therefore the turbulent viscosity has the form

$$\nu = \alpha_{\rm SS} c_{\rm s} H, \tag{1.24}$$

and is characterised by only one dimensionless parameter, $\alpha_{\rm SS}$, known as the Shakura-Sunyaez α parameter, which must be smaller than unity. The timescale on which viscosity acts is given by

$$\begin{aligned} t_\nu &\simeq \frac{R^2}{\nu} \\ &= \frac{R^2}{\alpha_{\rm SS} c_{\rm s} H} \\ &= \frac{1}{\Omega}\frac{1}{\alpha_{\rm SS}}\left(\frac{R}{H}\right)^2. \end{aligned} \tag{1.25}$$

1.3.4 Transitional Discs

One subset of accretion discs is the transitional disc. These are a late stage class II YSO that represent, as the name suggests, a disc transitioning from class II to class III as it loses its material. Transitional discs are classified by their SED, showing a near-IR deficit and a far-IR excess when compared to a classical T Tauri star, as shown in Figure 1.6. Since near-IR emission originates from hot material close to the star and far-IR orginates from cold material in the outer disc this near-IR deficit is interpreted as a large cavity in the inner region of the disc.

One theory for the formation of the cavities in transitional discs is the photoevaporation model, first described by Begelman et al. (1983) in the context of black hole discs and adapted to protoplanetary discs by Hollenbach et al. (1994). In this scenario the surface layers of a disc are heated to temperatures high enough to drive a pressure supported wind which overcomes gravity. Considering the photoevaporative wind acting alone to clear the disc gives a timescale far longer than the lifetime of a disc, however combined with viscous evolution (described in Section 1.3.3) it acts on a far shorter timescale and can visibly affect the disc (Clarke et al., 2001).

In the early disc life the accretion rate due to viscous evolution is much larger than the mass loss due to the photoevaporative wind. Over time, however, the accretion rate drops and eventually a time is reached when the accretion rate is overtaken by the photoevaporation rate at the "gravitational radius" (Hollenbach et al., 1994):

$$R_{\rm g} = \frac{{\rm G}M_*}{c_{\rm s}^2}, \tag{1.26}$$

where M_* is the mass of the star. Once this occurs any fluid parcel in the outer disc will be removed by the photoevaporative wind when it viscously drifts to this radius, thus opening a gap and cutting off the resupply of material to the inner disc. The inner disc is then quickly accreted from the inside-out on a viscous timescale of order $R_{\rm g}^2/\nu \ll R_{\rm out}^2/\nu$,

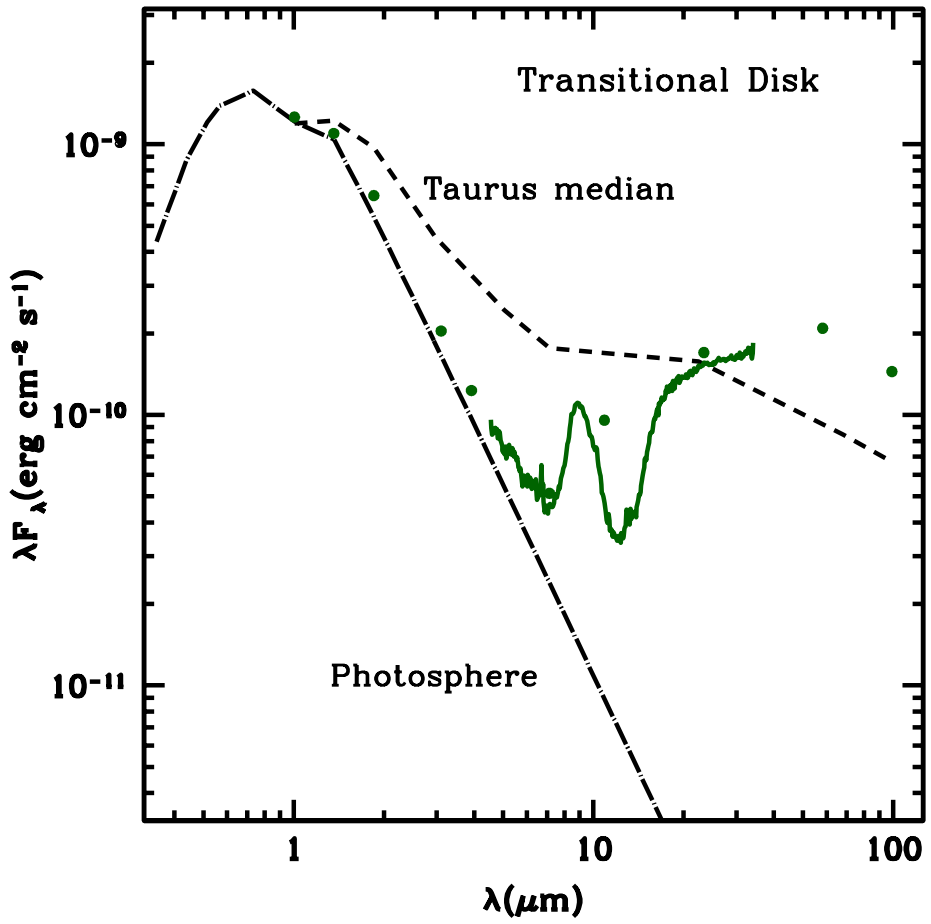

Figure 1.6: SED of the transitional disc GM Aur (Calvet et al., 2005). Fluxes have been corrected for redenning and scaled to the stellar photosphere (dot-dashed line). Typically for a transitional disc the SED shows a deficit in the near-IR and an excess in the far-IR when compared to a classical T Tauri star (dashed line). (source: Espaillat et al., 2014)

where $R_{\rm out}$ is the outer radius of the disc, leaving a large cavity out to $R_{\rm g}$ that resembles a transitional disc. The cavity wall is now directly heated by the central star, increasing the photoevaporative rate while the accretion rate continues to decrease, leading to a cavity that grows larger with time. A schematic of this process is given in Figure 1.7.

Work by Andrews et al. (2011) and Owen and Clarke (2012) found two classes of transitional discs, mm-faint and mm-bright, based on the emission strength at 1.3 mm compared to the median of $\sim$ 30 mJy. The photoevaporative model predicts that a decreasing transitional disc fraction with increasing mm-flux. This is because mm-flux is used as a good proxy for disc mass, which decreases over time due to accretion, and transitional discs are assumed to be at a late evolutionary stage by the photoevaporative model. While Andrews et al. (2011) and Owen and Clarke (2012) did find this to be the

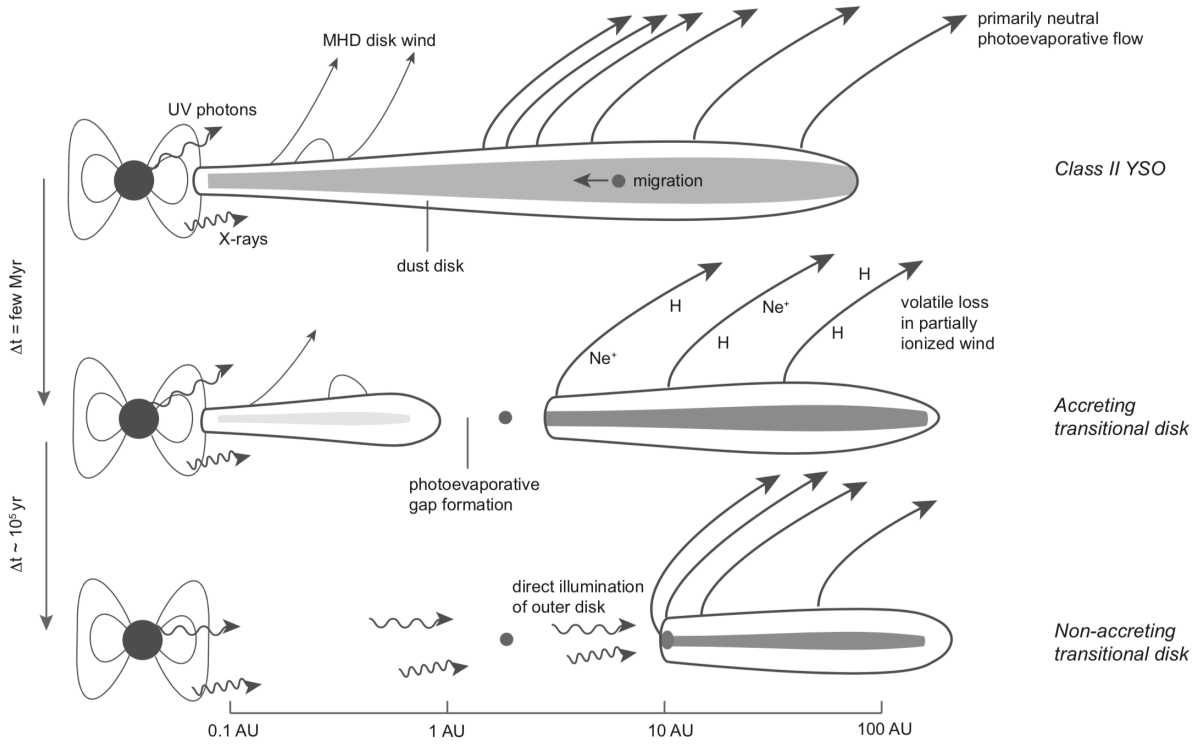

Figure 1.7: Schematic diagram of the photoevaporation process. At early stages the accretion dominates and the disc resembles a class II YSO. Eventually the accretion rate drops and photoevaporation dominates, opening a gap in the disc, allowing for material to quickly be cleared from the inside-out, leaving behind a transitional disc. (source: Alexander et al., 2014)

case for mm-faint discs, they also found that the transitional disc fraction increased for mm-bright discs (see Figure 1.8). Furthermore, in a transitional disc survey performed by Manara et al. (2014) the mass accretion rate was not found to be a decreasing function of cavity size (see Figure 1.9). These results imply that mm-bright transitional discs are much younger than predicted by the photoevaporation model and a model for cavity opening that works on a shorter timescale is needed to accurately describe them. One such model, which is the focus of this thesis, is to open a cavity via binary star interactions.

1.4 Circumbinary Discs

A circumbinary disc is simply any accretion disc that surrounds a binary star. The presence of a second star act to open a large cavity in the inner region of the disc. The process by which a cavity is opened in an accretion disc is a competition between the Lindblad resonances from a stellar companion, which act to open a cavity, and the disc viscosity, which acts to close it. Investigations into this process were originally performed

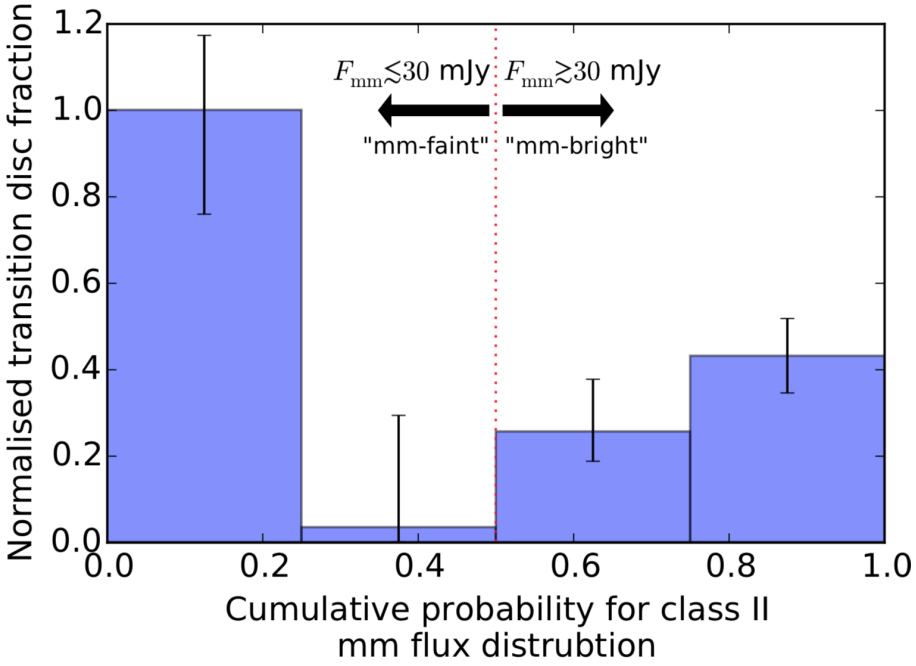

Figure 1.8: Normalised transitional disc fraction in each quartile of the primordial discs' mm-flux distribution. The median 1.3mm flux for primordial discs is $\sim$ 30 mJy. Discs brighter than this are classified as mm-bright, while discs that are fainter are classified as mm-faint. (source: Owen, 2016)

by Goldreich and Tremaine (1979) and Lin and Papaloizou (1986). They didn't consider binary companions, however, instead focusing on planets orbiting within the disc, which act to open a gap at their orbital radius. As we are not considering planets we will instead detail the works done by Artymowicz and Lubow (1994), hereafter AL94, and Miranda and Lai (2015), hereafter ML15, who applied the works of Goldreich and Tremaine (1979) and Lin and Papaloizou (1986) to stellar companions opening a cavity. They did this by working in a reference frame centred on the centre of mass of the binary, rather than on a single star, and carefully rearranged the disturbing potential due to the presence of the companion, expressing it as a sum of Fourier components

$$\Phi = \sum_{m,l} \Phi_{m,l}(R)\cos(m\phi - l\Omega_{\rm B}t), \tag{1.27}$$

where (R, ϕ) specifies the position within the disc in polar co-ordinates, m is the azimuthal number in the disc plane (formally, $m > 0$), l is a time harmonic number, $\Omega_{\rm B} = ({\rm G}M_{\rm tot}/a^3)^{1/2}$ is the binary orbital frequency, $M_{\rm tot} = M_1 + M_2$ is the total mass of the binary, and a is the binary semi-major axis. Here Φ is given per unit mass. Each potential harmonic $\Phi_{m,l}$ rotates with pattern frequency

$$\omega_{\rm P} = \frac{l}{m}\Omega_{\rm B} \tag{1.28}$$

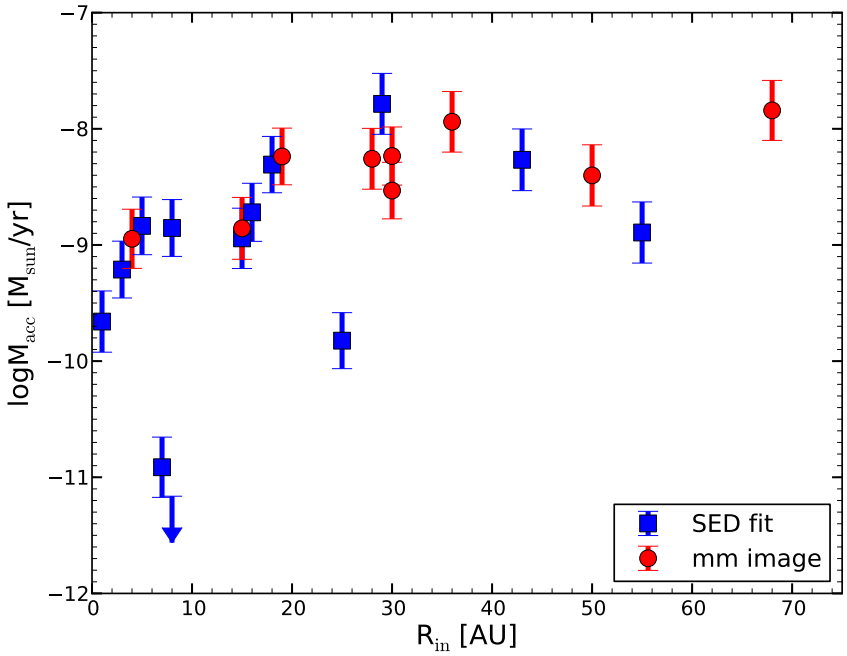

Figure 1.9: Logarithm of mass accretion rate plotted against cavity size for a sample of transitional discs. (source: Manara et al., 2014)

and excites density waves at three resonances (AL94): a corotational resonance (CR) at the radius where the disc rotation rate is equal to the potential harmonics pattern frequency, $\Omega(R) = \omega_{\rm P}$, and two (one outer and one inner) Lindblad resonances (LRs) where the forcing of a particle orbiting within the disc occurs at the epicyclic frequency, $m(\omega_{\rm P} - \Omega(R)) = \pm\kappa R$, where κ is the epicyclic frequency, the frequency of radial motions of fluid parcels due to a small perturbation in their orbit. For a circumbinary disc which is exactly Keplerian, $\kappa(R) = \Omega(R)$, the LRs are located at

$$\frac{R_{\rm LR}}{a} = \left(\frac{m \pm 1}{l}\right)^{2/3}, \tag{1.29}$$

where the upper sign corresponds to the outer Lindblad resonances (OLRs) and the lower sign corresponds to the inner Lindblad resonances (ILRs). Torques are also applied at the corotational resonances

$$\frac{R_{\rm CR}}{a} = \left(\frac{m}{l}\right)^{2/3}, \tag{1.30}$$

but these do not act to open a gap in an accretion disc (AL94), so we only need to consider the LRs. The torque acted on the disc at a LR is given by (Goldreich and Tremaine, 1978, 1979)

$$T_{m,l} = -m\pi^2 \left(\Sigma \left(\frac{\rm dD}{\rm dlnR}\right)^{-1} |\psi_{m,l}|^2\right), \tag{1.31}$$

where Σ is the surface density of the disc, $D = \kappa^2 - m^2(\Omega - \omega_{\rm P})^2$ and

$$\psi_{m,l} = \frac{{\rm d}\phi_{\rm m,l}}{{\rm dlnR}} + \frac{2\Omega}{\Omega - \omega_{\rm P}}\Phi_{m,l}. \tag{1.32}$$

The torque at ILRs is negative, so fluid elements lose angular momentum and drift inwards, while the torque at OLRs is positive, so fluid elements gain angular momentum and are forced to larger radii. Since $R_{\rm OLR} > R_{\rm ILR}$ these fluid motions act to open a cavity.

Counteracting the clearing effects of Lindblad torques is the viscous torque, which acts to close the gap. The strength of the viscous torque is given by (Pringle, 1981)

$$T_\nu = 3\pi\alpha_\nu \left(\frac{H}{R}\right)^2 \Sigma\Omega^2 R^4. \tag{1.33}$$

A gap can be opened at the (m, l) LR if $|T_{m,l}| \geq |T_\nu|$. Comparing (1.31) and (1.33) gives a gap opening criterion (Lin and Papaloizou, 1986)

$$\alpha_\nu \left(\frac{H}{R}\right)^2 \leq \frac{T_{m,l}}{3\pi\Sigma\Omega^2 R^4}. \tag{1.34}$$

A gap will not be successfully opened, however, if the opening timescale is long compared to the other timescales in the disc. This leads to a second criterion for gap opening based a comparison of the opening time to the viscous closing time (AL94)

$$\frac{t_{\rm open}}{P} \simeq \frac{1}{2\pi\alpha_\nu \left(H/R\right)^2}\left(\frac{\Delta r}{R}\right), \tag{1.35}$$

where P is the orbital period. This allowed AL94 to find the inner radius of a cavity by finding the largest LR at which a gap can be cleared. They predicted a cavity size between 2–4 times the binary semi-major axis, becoming larger both with increasing binary eccentricity and decreasing disc viscosity.

Numerous computational studies have confirmed this basic picture (AL94; Günther and Kley, 2002; Thun et al., 2017), with some discrepancies over the exact cavity size. Artymowicz and Lubow (1994) checked their own theoretical predictions of the dependence of cavity size on mass ratio and eccentricity against Smoothed Particle Hydrodynamics (SPH) simulations (see Sec 2.2). All of these simulations were performed in 2 dimensions and simulated circumbinary discs coplanar with the binary orbit and with an initial inner cavity radius of twice the semi-major axis. The results of the simulations are given in Table 1.1 and snapshots of the simulation with mass fraction $q = 0.3$, where $q = M_1/(M_1 + M_2)$ and eccentricity $e = 0.1$ are given in Fig 1.10. They confirmed that the cavity radius increases with both mass fraction and eccentricity. Fig 1.10 shows the timescale with which a cavity is opened. In the first (top left) panel (0.5 binary orbits) we

Mass fraction, q	Eccentricity e	Cavity radius R/a
0.3	0.00	1.80 ± 0.10
0.3	0.02	1.92 ± 0.10
0.3	0.05	2.15 ± 0.10
0.3	0.10	2.40 ± 0.10
0.3	0.30	2.72 ± 0.10
0.3	0.50	2.88 ± 0.10
0.3	0.70	3.10 ± 0.10
0.1	0.00	1.80 ± 0.10
0.1	0.10	2.10 ± 0.10
0.1	0.50	2.73 ± 0.10

Table 1.1: Model setup and disc inner edge location for SPH simulations run by Artymowicz and Lubow (1994)

see a rapid excavation of gas near the L4 and L5 Lagrange points. The cavity is almost fully opened after only 3 binary orbits (top right), and after 10 binary orbits (bottom left) the disc in in quasi-equilibrium.

Thun et al. (2017) performed two-dimensional hydrodynamical simulations of circumbinary discs using the codes PLUTO and RH2D, running simulations for 16,000 binary orbits, nearly 3 orders of magnitude longer than the original SPH simulation performed by AL94. As shown in Fig 1.11, they found that after tens of thousands of orbits the cavity size can be as large as 7 times the semi-major axis, nearly twice what was found by both Artymowicz and Lubow (1994) & Miranda and Lai (2015). Also contrary to earlier findings, Thun et al. (2017) saw that at low eccentricity the cavity size decreases with eccentricity, with a minimum at $e \simeq 0.2$.

Miranda and Lai (2015) generalised the study by AL94 to discs inclined with respect to the binary orbital plane. Their findings are displayed in Fig 1.12, which shows the dependence of cavity inner radius on eccentricity e, mass ratio q, and disc inclination i. In agreement with AL94, they find that cavity size increases with eccentricity for a coplanar disc, and this behavior holds for $i \leq 45^\circ$ at any mass ratio. At high inclination $i \gtrsim 90^\circ$ the behavior changes and the disc inner radius can have many local maxima as a function of eccentricity. For retrograde discs at low mas ratio the cavity size is independent of eccentricity. This is because $|T_\nu| > |T_{m,l}|$ for all $(m, n) \neq (1, 1)$, regardless of eccentricity, so the cavity will always be truncated at the $(1, 1)$ resonances.

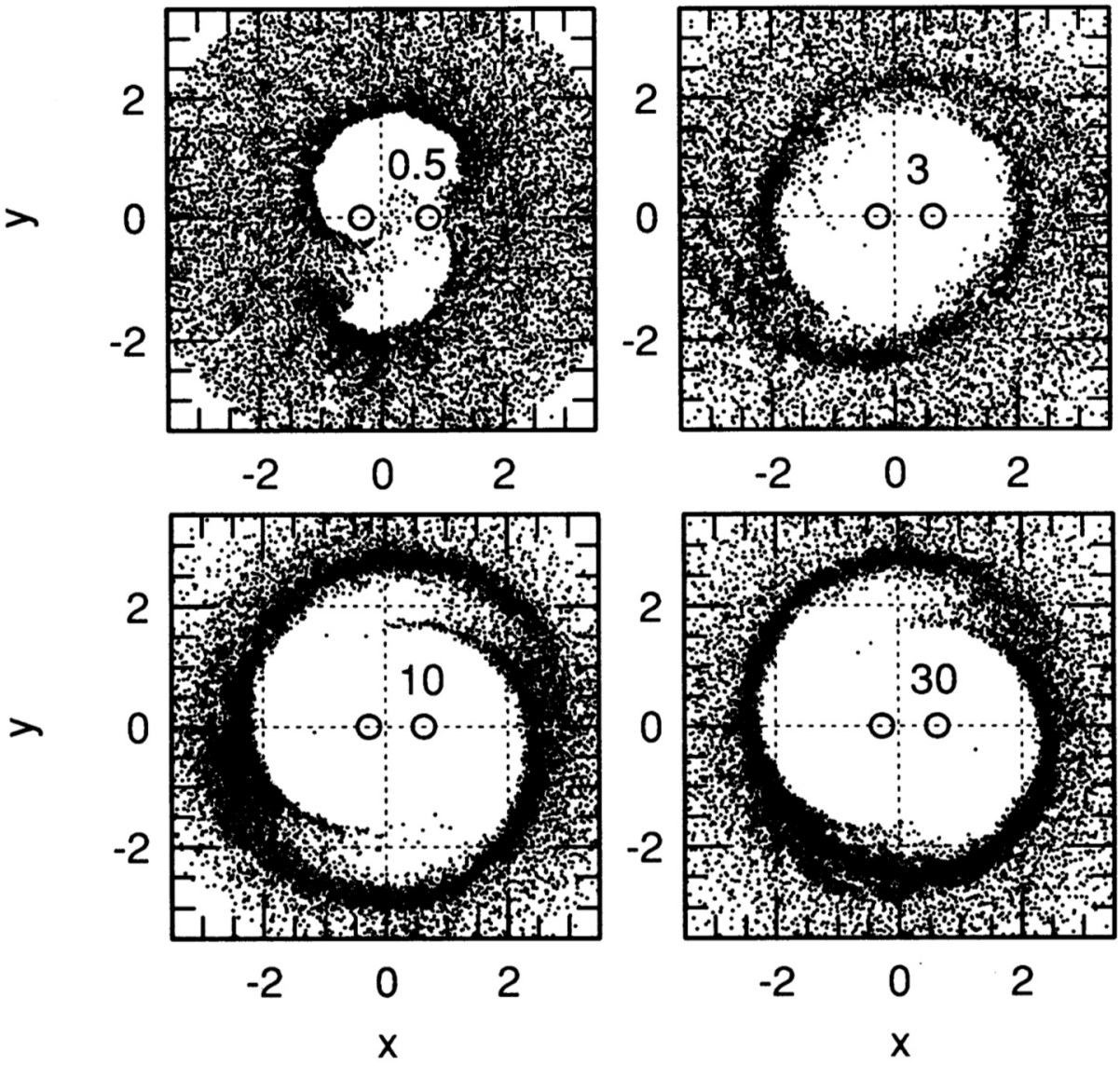

Figure 1.10: Circumbinary disc evolution for a binary with mass ratio $q = 0.3$ and eccentricity $e = 0.1$. Initially the disc had a surface density profile $\Sigma \propto R^{-1}$ extending between $2a$ and $4.5a$ where a is the semi-major axis. Axis are given in units of a and the numbers in each panel correspond to the number of binary orbits completed. (source: Artymowicz and Lubow, 1994)

Using 3-dimensional SPH simulations Aly et al. (2015) showed that any circumbinary disc on an initially inclined orbit will tend towards either a coplanar or a polar configuration. The critical angle above which a disc will tend towards a polar orbit is (Aly et al., 2018)

$$i_{\rm crit} = \tan^{-1}\sqrt{\frac{1-e^2}{5e^2}}. \tag{1.36}$$

That is to say that polar configurations are more likely for discs around highly eccentric binaries, or those that start with a large initial inclination. The analysis from ML15

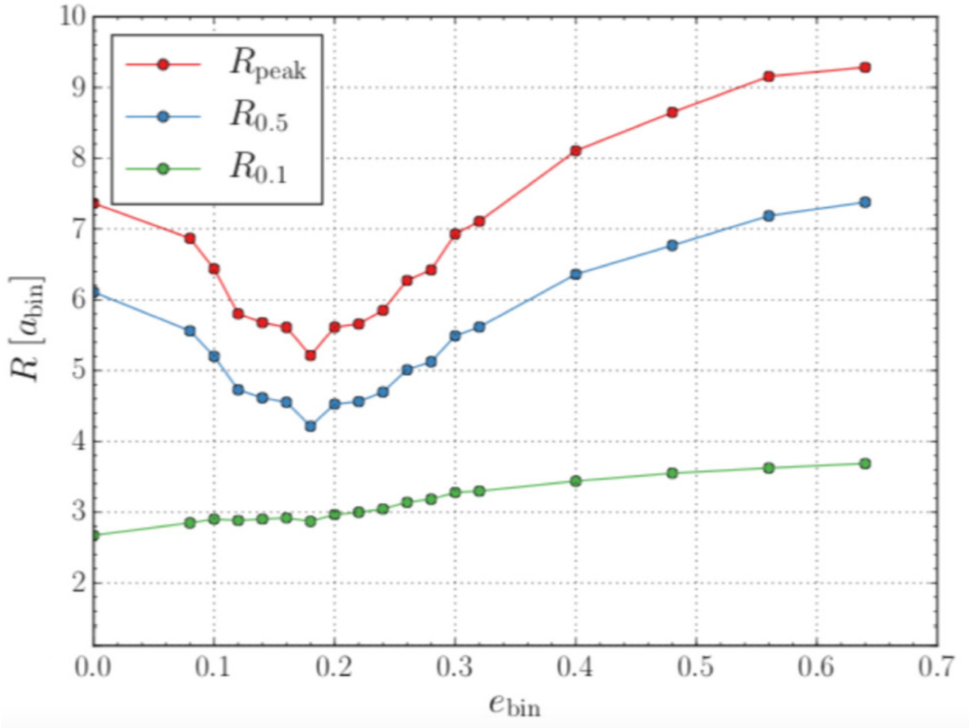

Figure 1.11: Cavity inner edge radius plotted against eccentricity from simulations runs by Thun et al. (2017). Each line corresponds to a different metric for calculating the cavity size. The red line corresponds to using the radius of the maximum surface density, the blue line 50% of the maximum surface density, and the green line 10% of the maximum. The blue line is the closest analogy to the definition from Artymowicz and Lubow (1994) (source: Thun et al., 2017)

implicitly assumes the disc stays at a fixed inclination, and so does not capture the long-term behaviour of a disc that realigns. Thus the behaviour of such discs is an open question, one that lends itself well to 3-dimensional numerical simulations as a means of answering it.

1.5 Observations of Disc Cavities

Perhaps the most well studied circumbinary disc is HD 142527. Located at a distance of 156^{+7}_{-6} pc (Gaia Collaboration et al., 2016) in the Sco-Cen association this disc contains many observational features commonly associated with circumbinary discs. A gas cavity is found out to a radius of 90 ± 5 AU (Perez et al., 2015) and a gas cavity out to ~ 140 AU is visible in IR imaging (Fukagawa et al., 2006), sub-millimeter continuum (Ohashi, 2008), and CO line emission (Casassus et al., 2013). Spiral structure originating from the cavity edge is seen in the IR (Fukagawa et al., 2006; Casassus et al., 2012). Cycle 0 ALMA observations reveal a horseshoe shaped structure at the inner edge in the dust continuum

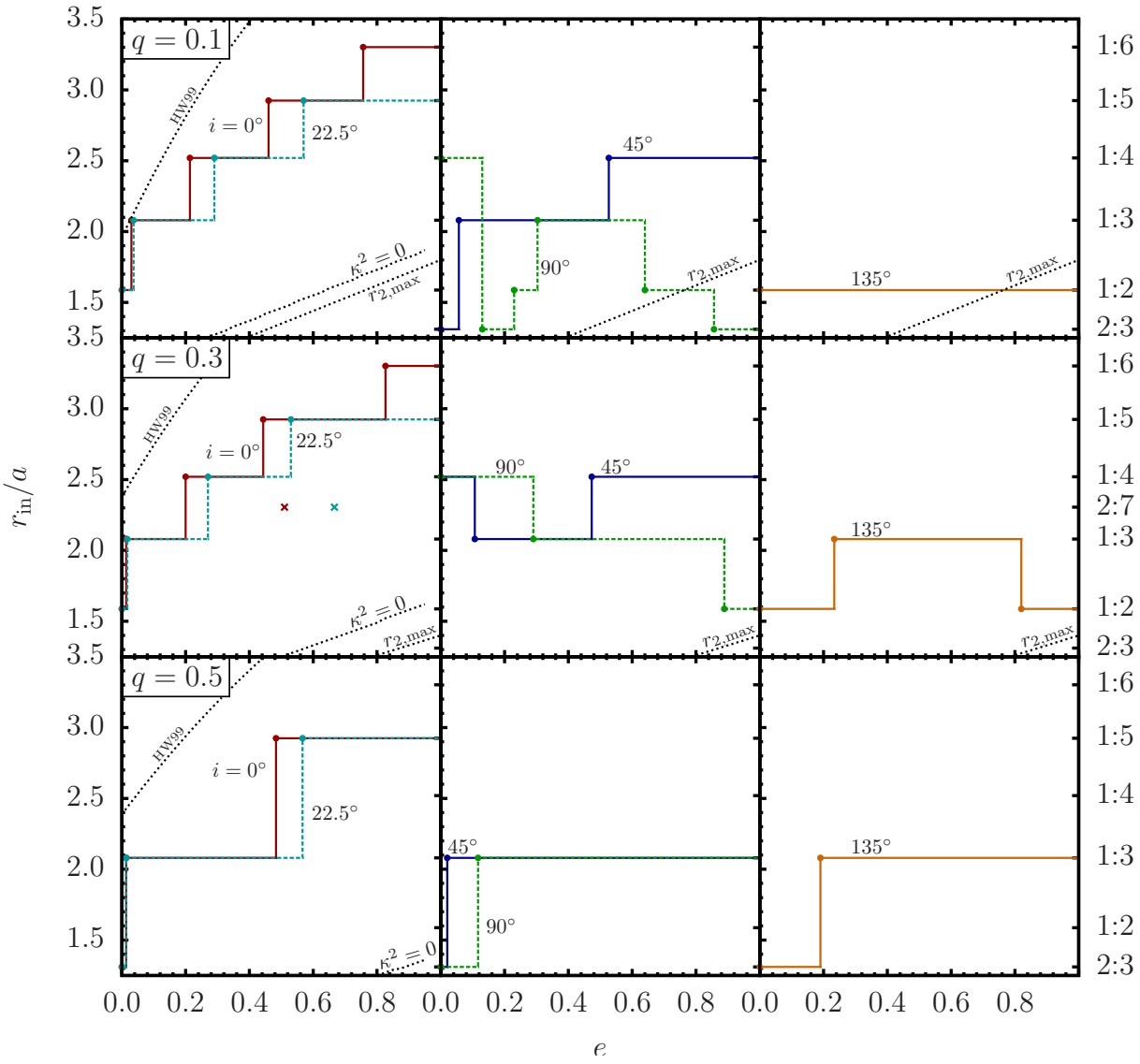

Figure 1.12: Cavity inner edge radius plotted against eccentricity as predicted analytically by Miranda and Lai (2015). Mass ratios of each row are given in the top left corner of the left panels, disc inclination is given by different colours and location of commensurabilities are labeled on the right. (source: Miranda and Lai, 2015)

emission (Casassus et al., 2013). Multiple scattered light observations recover shadows on the cavity wall (Fukagawa et al., 2006; Avenhaus et al., 2014, 2017), likely cast by some inclined inner disc (Marino et al., 2015). The high accretion rate of $\simeq 2 \times 10^{-7}$ $M_\odot$/yr onto the central stars (Garcia Lopez et al., 2006) implies the inner disc must be getting refilled by material from the outer disc, likely via the filaments of CO gas seen crossing the cavity in HCO+ emission (Casassus et al., 2013). These features are shown in Figure 1.13.

Price et al. (2018a) modelled HD 142527 using the 3-dimensional SPH code `PHANTOM` (see Section 2.2) of a circumbinary disc, taking the estimates of the binary orbit from

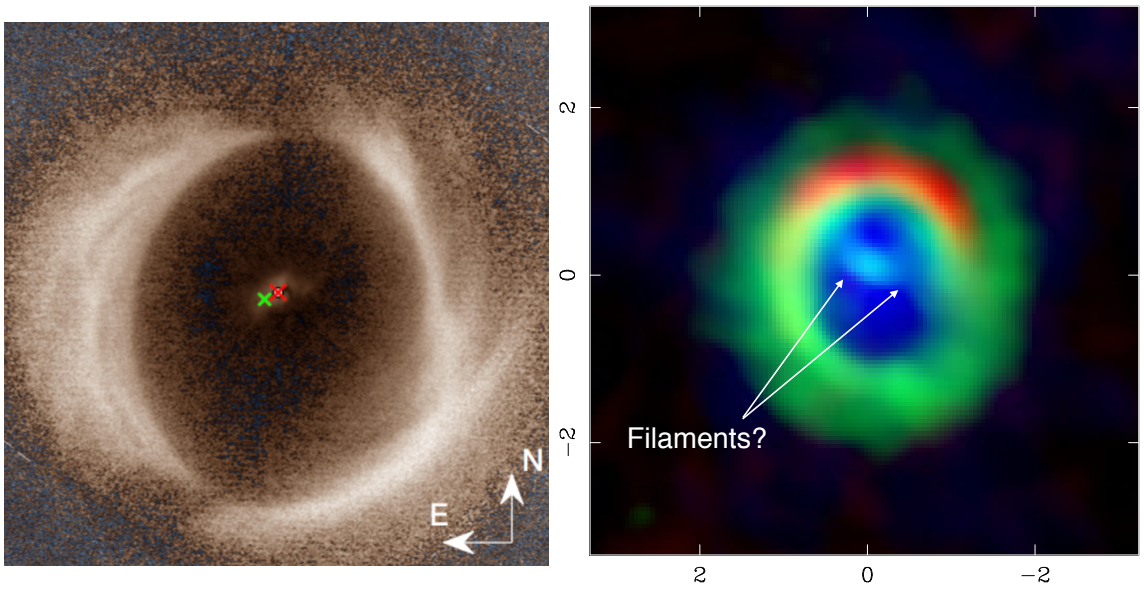

Figure 1.13: Observations of HD 142527. Left: Scattered light image from Avenhaus et al. (2017). Two stars are observed inside a large cavity, with shadows being cast on the cavity wall and a faint spiral structure originating at the cavity edge. Right: ALMA Cycle 0 image from Casassus et al. (2015a). A large cavity is once again visible, with filaments of material falling onto the central stars and a horseshoe overdensity near the cavity edge.

Lacour et al. (2016). Using radiative transfer, they then created synthetic observations to compare with the above works. They were able to recover the correct cavity size, as well as the spiral structure in the IR, the horseshoes structure presented by Casassus et al. (2013), and an inner disc that casts shadows on the cavity wall, all while maintaining a high accretion rate from filaments connecting the inner and outer discs. The ability to recover all of these features from simulations of a circumbinary disc suggests that the presence of a binary companion is indeed their source.

Once thought to be a circumbinary disc, GG Tau has been the subject of many works. Early mm-observations from Guilloteau et al. (1999) dubbed it "the ring world" due to large cavity and subsequent ring shaped disc. Further observations, however, confirmed that GG Tau A and GG Tau B are they themselves binaries with their own circumbinary discs (White et al., 1999; Andrews et al., 2014). Observations from Di Folco et al. (2014) suggest that GG Tau A may be even more complex again, potentially being a hierarchical triple. Due to the complex nature of the GG Tau system we caution that the results presented in this work are not appropriate for a comparison with observations of the GG

Tau circumbinary discs without careful consideration of the effects from all other bodies within the system.

A number of transitional discs exhibit large cavities and some of the features described above, but as yet no detected binary companion. Spirals are visible in the disc of DZ Cha in both J-band polarimetry (Canovas et al., 2018) (see Figure 1.14) and NIR scattered light observations (Yu et al., 2019). SR 21 also shows spiral structure in H-band scattered light images from SPHERE (Muro-Arena et al., 2020). DoAr 44 shows asymmetric dust regions at the cavity edge, reminiscent of the horseshoe in HD 142527, in band 7 ALMA cycle 1 observations (van der Marel et al., 2016a) and H-band SPHERE observatinos (Casassus et al., 2018). Similar structure can be seen in Band 6 ALMA observations of CQ Tau (Ubeira Gabellini et al., 2019), as shown in Figure 1.15. Muro-Arena et al. (2019) presented J- and H-band observations in polarized scattered light with SPHERE of HD 139614 showing shadows on the outer disc, as shown in Figure 1.16. The cavities in these transitional discs have also been found to not be completely devoid of gas, but rather depleted in surface density by up to 5 orders of magnitude compared to the outer disc (van der Marel et al., 2015, 2016b, 2018).

These features have been shown to be the consequence of a disc-binary interactions. Spiral arms occur in any disc with a companion, be it stellar or planetary (Ogilvie and Lubow, 2002; Dong et al., 2015; Benisty et al., 2017). Shadows on the cavity edge or on the disc itself require some misalignment in the inner disc which can be caused by a companion on an inclined orbit (Marino et al., 2015; Min et al., 2017). Recently Ragusa et al. (2017) suggested that horseshoes, and other asymmetries at the cavity edge, can be caused by binary companions on eccentric orbits, an idea first put forward by Ataiee et al. (2013). This suggests that the transitional discs mentioned above potentially host unseen stellar companions, we need only the methods to detect them.

Similar to the work by Price et al. (2018a), Calcino et al. (2019) modelled IRS 48, a transitional disc with no known stellar binary, using PHANTOM and compared observations with synthetic images from radiative transfer calculations. They recovered spiral structures, a dusty horseshoe overdensity, and their velocity map showed a twisted feature similar to that of van der Marel et al. (2016a). They suggest that these features, and the close match to observational data, indicate that IRS 48 is host to a stellar companion. While this is not a detection of a companion, it does lend weight to the idea that many transitional discs may as yet be hiding unresolved binaries.

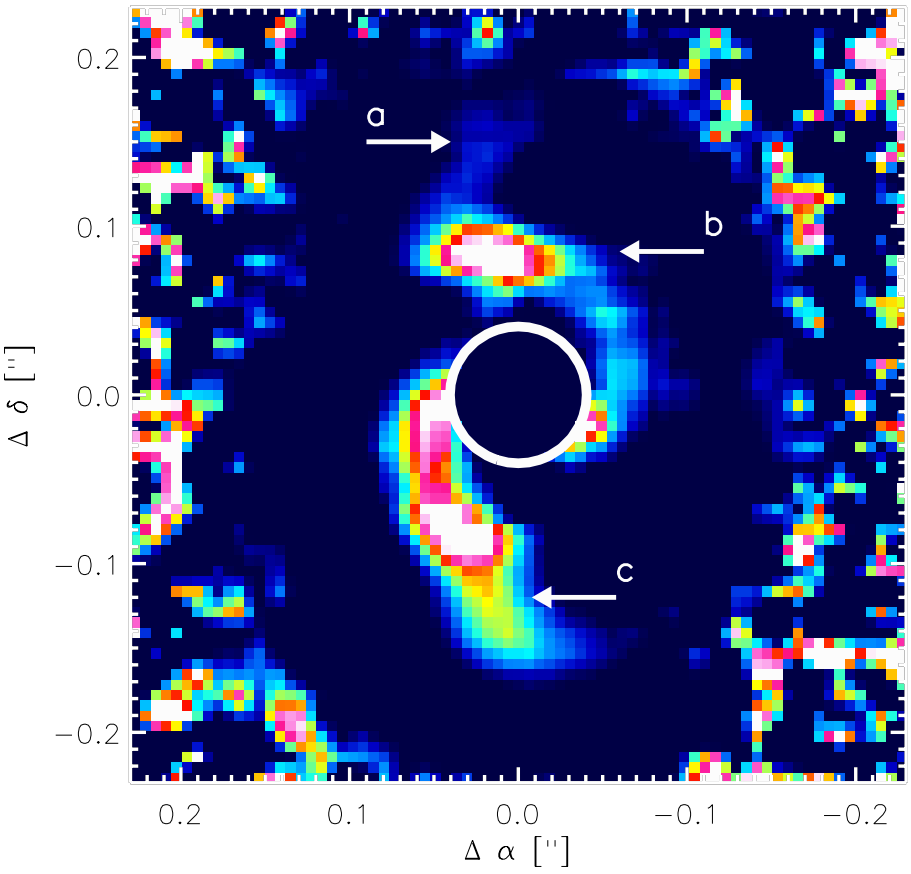

Figure 1.14: Unsharped Q_Φ image of DZ Cha from Canovas et al. (2018). A strong spiral is seen originating from the cavity edge.

1.6 Goals of this Thesis

As seen in this introduction, the cavity opening process in inclined circumbinary discs is an unsolved problem. Furthermore, the direct detection of a binary companion remains a difficult problem, so we must turn to indirect methods to infer the presence the companion in most binary systems. As such the main questions this thesis seeks to answer are:

- What is the final cavity size of a circumbinary disc with arbitrary inclination?
- What can the observed cavity tell us about the binary companion and disc properties?
- What are the detectable signatures of an unseen binary companion on the circumbinary disc?

In order to answer these questions we perform 3-dimensional simulations of circumbinary discs to investigate their dynamical behavior. Then we create synthetic observations

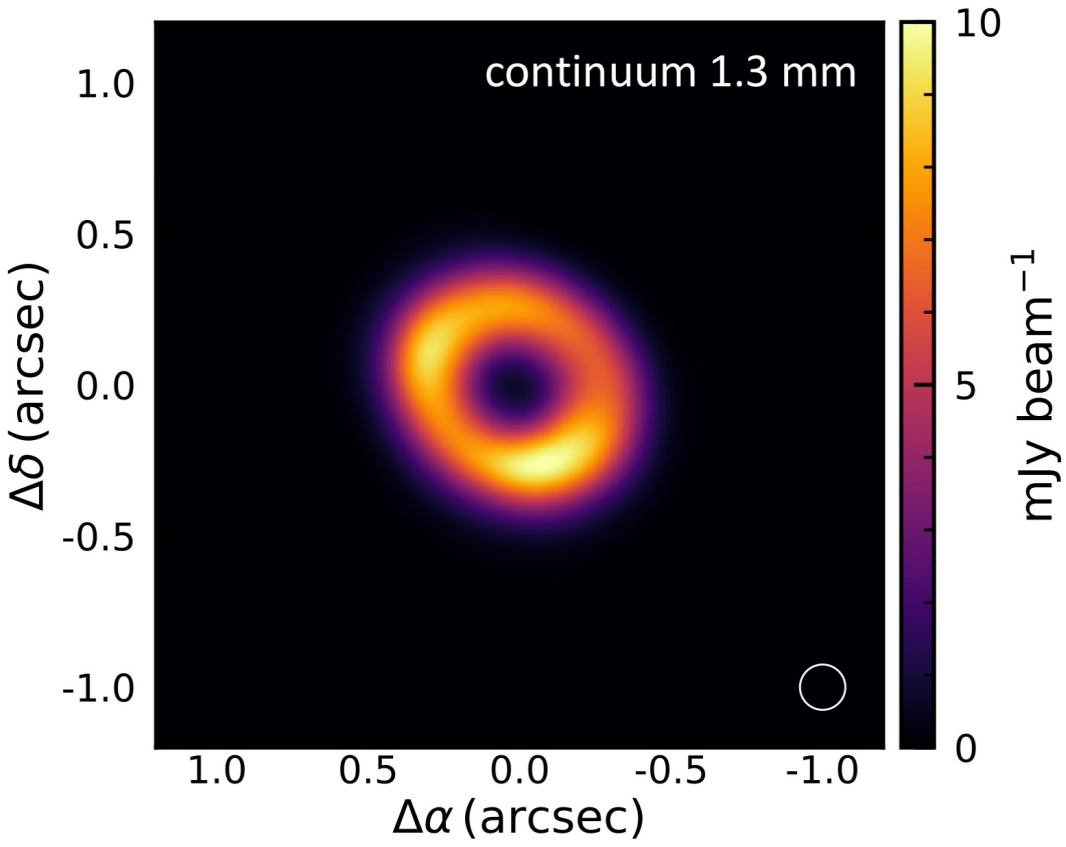

Figure 1.15: ALMA continuum observations at 1.3 mm of CQ Tau from Ubeira Gabellini et al. (2019). Two overdensities, reminiscent of the horseshoe-shaped features in HD 142527, ar visible at the inner edge of the disc.

of these discs in order to determine the detectable signatures of the binary. Finally, we develop a metric to quantify the effect of the binary on the disc.

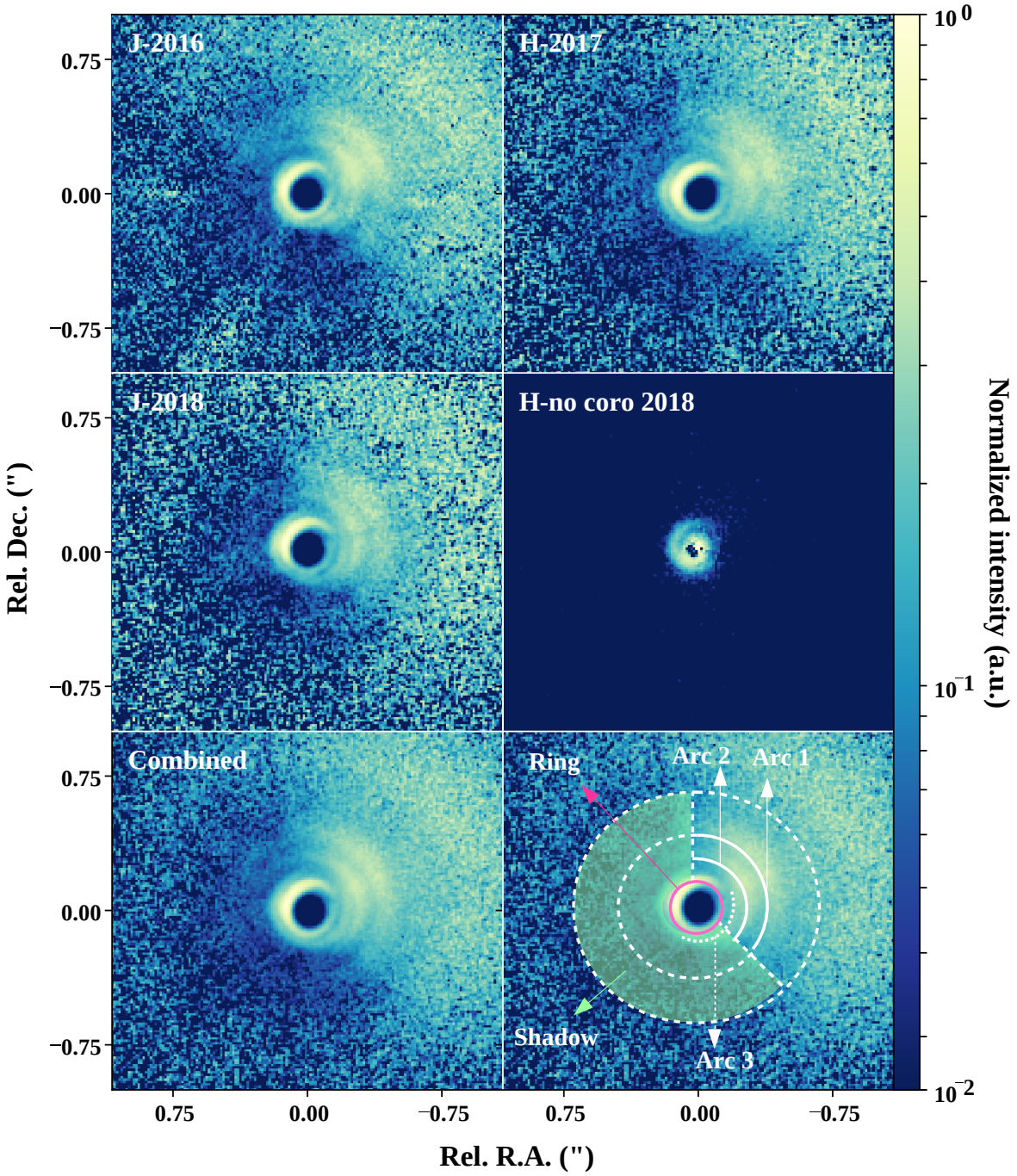

Figure 1.16: SPHERE scattered light observations of HD 139614 from Muro-Arena et al. (2019). Heavy shadowing is seen in the outer disc, implying some misalignment in the inner disc.

Chapter 2

Methods

2.1 Disc Model

In this work we model the discs as a single fluid using the Euler equations in 3 dimensions, assuming no self gravity in the disc,

$$\frac{\mathrm{d}\rho}{\mathrm{d}t} = -\rho\nabla\cdot\mathbf{v}, \tag{2.1}$$

$$\frac{\mathrm{d}\mathbf{v}}{\mathrm{d}t} = \frac{-\nabla P}{\rho} - \nabla\Phi, \tag{2.2}$$

$$\Phi = \frac{-GM_1}{|\mathbf{r}-\mathbf{r}_1|} - \frac{GM_2}{|\mathbf{r}-\mathbf{r}_2|}, \tag{2.3}$$

$$P = c_\mathrm{s}^2(R)\rho, \tag{2.4}$$

where ρ, $\mathbf{v}$, P and c_s are the density, velocity, pressure and sound speed of fluid elements in the disc, M_1 and M_2 are the masses of the primary and secondary stars, and $\mathbf{r}_1$ and $\mathbf{r}_2$ are the positions of the primary and secondary stars. Equation (2.4) approximates the temperature within the disc as being a specified function of cylindrical radius, i.e. $T \equiv T(R)$.

Evolving these discs requires choosing a numerical method to use. Due to the complex geometry of the discs, as well as the high density contrast and the presence of free boundaries we simulate the discs using the Smoothed Particle Hydrodynamics (SPH) method, specifically the code `PHANTOM` (Price et al., 2018a), described in Section 2.2. Then, we create synthetic observations of these discs using the radiative transfer code `MCFOST` (Pinte et al., 2006, 2009), described in Section 2.3

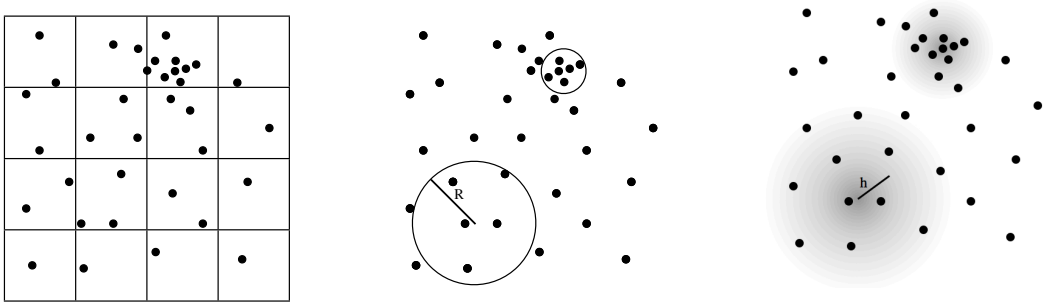

(a) Grid (b) Local sample (c) Weighted local sample

Figure 2.1: Three different approaches to computing a continuous density field from an arbitrary distriution of point masses. a) Constructing a mesh on top of the point masses, as adopted in particle-mesh methods. b) Sampling the local volume based on number of neighbours. c) Weighted local sampling, as adopted in SPH. (Source: Price, 2012)

2.2 Smoothed Particle Hydrodynamics (SPH)

The SPH formalism was first developed by Lucy (1977) and Gingold and Monaghan (1977) in an attempt to model the highly asymmetric phenomena commonly found in astrophysics. It is a Lagrangian particle method for solving the equations of hydrodynamics on a set of discrete particles, each representing a fluid element. A `PHANTOM` output consists of a dump file containing the relevant properties of these particles (e.g. position, density, temperature, etc.) so that the properties of the entire domain can be found by interpolating between these particles. While we describe the SPH method in this section; many reviews exist which provide further detail (see: Benz, 1990; Monaghan, 1992, 2005; Rosswog, 2009; Price, 2012).

2.2.1 Density Estimates, Smoothing Kernels & Smoothing Lengths

The basis of SPH is the answer to a simple question: how does one compute a density field from a set of discrete particles?

There are three main methods to solving this problem, shown in Fig. 2.1. Perhaps the most intuitive method is to construct a grid and calculate the density in each cell as the mass divided by the volume (Fig. 2.1a). This method suffers from being unable to resolve regions of high or low density when the density distribution is highly non-uniform and spans many orders of magnitude. Furthermore, it is slow due to the need to interpolate to and from each particle (e.g. when calculating forces). One solution to these issues is to instead sample the local volume around each particle using, for example, a fixed number

of neighbours (Fig. 2.1b). This method, however, is noisy to whether a particle at the edge of the sample volume is in or out, with fluctuations on the order of the inverse of the number of neighbours. Smoothing the boundary of the sample volume leads to the SPH formalism (Fig. 2.1c), where density is calculated as a weighted sum of neighbouring particles, given by

$$\rho(\mathbf{r}) = \sum_{b=1}^{N_{neigh}} m_b W(\mathbf{r} - \mathbf{r}_b, h), \tag{2.5}$$

where m_b and $\mathbf{r}_b$ are the mass and position, respectively, of particle b, N_{neigh} is the number of neighbours, W is the weighting function, known as the smoothing kernel, and h, the smoothing length, defines the drop-off rate of W. Conservation of mass, $\int \rho \mathrm{dV} = \sum_{\mathrm{b=1}}^{\mathrm{N_{neigh}}} \mathrm{m_b}$, gives us the normalisation condition for W:

$$\int_V W(\mathbf{r}' - \mathbf{r}_b, h)\mathrm{dV}' = 1. \tag{2.6}$$

The accuracy of the SPH density estimate is strongly influenced by the choice of W, so care must be taken when constructing a smoothing kernel. A well constructed W will have positive weighting, smooth derivatives and is monotonically decreasing. Furthermore, to ensure that the density estimate is independent of orientation the kernel must be symmetrical in $(\mathbf{r} - \mathbf{r}_b)$. Lastly, having a flat central portion ensures that the density estimate is not noisy to a small change in location of nearby neighbours.

A natural function that satisfies all these criteria is the Gaussian, however since it requires interactions between every pair of particles it has a computational cost of $\mathcal{O}(N^2)$. Since distant particles only have a minor contribution on the density estimate it is possible to ignore these without introducing significant inaccuracies. Thus, by choosing a kernel with compact support, that is a kernel that reaches zero at some finite radius, it is possible to reduce the computational cost to $\mathcal{O}(N_{neigh}N)$ while maintaining a high accuracy.

The most commonly used kernels are derived from the Schoenberg (1946) B-spline functions (Monaghan and Lattanzio, 1985). The simplest of these functions is the M_4 cubic spline truncated at $2h$, plotted in Figure 2.2:

$$w(q) = \sigma \begin{cases} \frac{1}{4}(2-q)^3 - (1-q)^3, & 0 \le q < 1; \\ \frac{1}{4}(2-q)^3, & 1 \le q < 2; \\ 0, & q \ge 2. \end{cases} \tag{2.7}$$

Smoothing kernels are constructed from splines by defining $W(\mathbf{r} - \mathbf{r}_b, h) \equiv \frac{1}{h^d} w(q)$, where $q = |\mathbf{r}' - \mathbf{r}|/h$, d is the number of dimensions, and σ is a normalisation constant. For the cubic spline kernel $\sigma = [2/3, 10/(7\pi), 1/\pi]$ in $[1, 2, 3]$ dimensions. Higher order spline

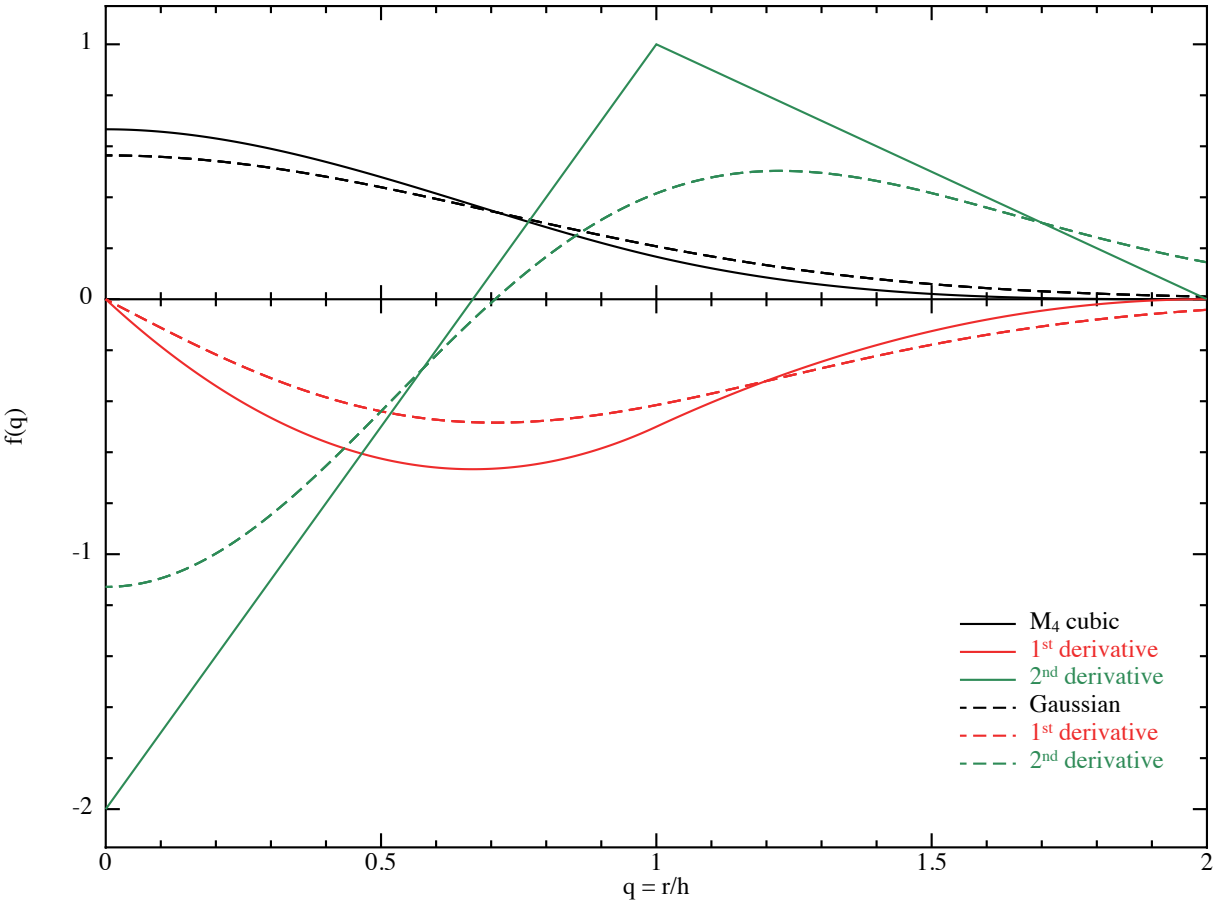

Figure 2.2: M_4 cubic spline and Gaussian kernels, and their first two derivatives.

functions exist, giving higher accuracy at the expense of computational cost.

There exist other families of kernels, such as those based on the Wendland (1995) functions (Dehnen and Aly, 2012), and the 'double-hump' shaped kernel functions (Fulk and Quinn, 1996; Laibe and Price, 2012). Each of these kernels come with their own sets of strengths and weaknesses, and their applicability is context dependant. Which kernel to use in which context is still an open question and we refer the reader to Section 2.1.6 of Price et al. (2018b) for a small discussion on the issue. In this work we exclusively use the B-spline kernels.

One advantage of SPH is that the resolution naturally increases with density, but in order to accurately model both the dense and sparse regions requires a variable smoothing length that is a function of density. Since density itself is a function of the smoothing length, this leads to a pair of simultaneous equations (Monaghan, 2002):

$$h(\mathbf{r}_a) = h_{\rm fac}\left(\frac{m_a}{\rho_a}\right)^{1/d}; \qquad \rho(\mathbf{r}_a) = \sum_b m_b W(\mathbf{r}_a - \mathbf{r}_b, h_a), \tag{2.8}$$

where $h_{\rm fac}$ relates the smoothing length to the mean particle spacing and is of order unity. In practice this means that the density and smoothing length must be found using an iterative root-finding method, the choice of which is free but `PHANTOM` uses Newton-Raphson.

2.2.2 Equations of Motion in SPH

The discretisation of Equation 2.2 can be achieved by considering the Euler-Lagrange equations (e.g. Gingold and Monaghan, 1982; Price, 2012)

$$\frac{\mathrm{d}}{\mathrm{d}t}\left(\frac{\partial L}{\partial \mathbf{v}}\right) - \frac{\partial L}{\partial \mathbf{r}} = 0, \tag{2.9}$$

where $L = T - V$ is the Lagrangian, the difference between kinetic energy, T and potential energy, V. The discrete Lagrangian, for a system of point masses, is given by

$$L = \sum_b m_b \left[\frac{1}{2}v_b^2 - u_b(\rho_b, s_b)\right], \tag{2.10}$$

with derivatives

$$\frac{\partial L}{\partial \mathbf{v}_a} = m_a \mathbf{v}_a; \qquad \frac{\partial L}{\partial \mathbf{r}_a} = \sum_b m_b \left.\frac{\partial u_b}{\partial \rho_b}\right|_s \frac{\partial \rho_b}{\partial \mathbf{r}_a}, \tag{2.11}$$

where the thermal energy, u, is a function of both density, ρ, and entropy, s, and we assume that the entropy is constant when taking the spatial derivative of the Lagrangian.

At constant entropy, the change in internal energy is given by

$$\left.\frac{\partial u_b}{\partial \rho_b}\right|_s = \frac{P}{\rho^2}. \tag{2.12}$$

The density gradient is given by

$$\frac{\partial \rho_b}{\partial \mathbf{r}_a} = \frac{1}{\Omega_a}\sum_c m_c \frac{\partial W_{bc}(h_b)}{\partial \mathbf{r}_a}(\delta_{ab} - \delta_{ac}), \tag{2.13}$$

where

$$\Omega_a \equiv \left[1 - \frac{\partial h_a}{\partial \rho_a}\sum_b m_b \frac{W_{ab}(h_a)}{\partial h_a}\right], \tag{2.14}$$

is a term that takes into account the variable smoothing length and $W_{ab}(h_a) \equiv W(\mathbf{r}_a - \mathbf{r}_b, h_a)$.

Substituting Equations 2.12 and 2.13 back in to Equation 2.11 allows us to solve Equation 2.9, giving the standard form of the equation of motion:

$$\frac{\mathrm{d}\mathbf{v}_a}{\mathrm{d}t} = -\sum_b m_b \left[\frac{P_a}{\Omega_a \rho_a^2}\frac{\partial W_{ab}(h_a)}{\partial \mathbf{r}_a} + \frac{P_b}{\Omega_b \rho_b^2}\frac{\partial W_{ab}(h_b)}{\partial \mathbf{r}_b}\right]. \tag{2.15}$$

Conservation of momentum in this formalisation can be shown by considering the time derivatives of linear (Equation 2.16) and angular (Equation 2.17) momentum:

$$\frac{\mathrm{d}}{\mathrm{d}t}\sum_a m_a\mathbf{v}_a = \sum_a m_a\frac{\mathrm{d}\mathbf{v}_a}{\mathrm{d}t} = -\sum_a\sum_b m_a m_b\left(\frac{P_a}{\Omega_a\rho_a^2}+\frac{P_b}{\Omega_b\rho_b^2}\right)\nabla_a W_{ab}, \tag{2.16}$$

$$\frac{\mathrm{d}}{\mathrm{d}t}\sum_a \mathbf{r}_a\times m_a\mathbf{v}_a = \sum_a m_a\left(\mathbf{r}_a\times\frac{\mathrm{d}\mathbf{v}_a}{\mathrm{d}t}\right) = -\sum_a\sum_b m_a m_b\left(\frac{P_a}{\Omega_a\rho_a^2}+\frac{P_b}{\Omega_b\rho_b^2}\right)\mathbf{r}_a\times\nabla_a W_{ab}. \tag{2.17}$$

Both these quantities can be shown to be equal to zero by swapping the indices a and b in the double sum, adding half the original term to half the new term, and noting that $\nabla_a W_{ab}$ is antisymmetric. Thus, SPH exactly conserves momentum, up to the accuracy of the timestepping algorithm.

2.2.3 Timestepping

A popular integration scheme for SPH applications is the leapfrog method. A major strength of this scheme is its symplectic nature and time-reversibility, which means that it exactly conserves energy (Monaghan, 2005).

`PHANTOM` uses the leapfrog method in 'velocity Verlet' form (Verlet, 1967) with an extra predictor step in the velocity. The position, velocity and acceleration of the particles are updated as follows:

$$\mathbf{v}^{n+\frac{1}{2}} = \mathbf{v}^n + \frac{1}{2}\Delta t\mathbf{a}^n, \tag{2.18}$$

$$\mathbf{r}^{n+1} = \mathbf{r}^n + \Delta t\mathbf{v}^{n+\frac{1}{2}}, \tag{2.19}$$

$$\mathbf{v}^{*} = \mathbf{v}^{n+\frac{1}{2}} + \frac{1}{2}\Delta t\mathbf{a}^n, \tag{2.20}$$

$$\mathbf{a}^{n+1} = \mathbf{a}(\mathbf{r}^{n+1}, \mathbf{v}^{*}), \tag{2.21}$$

$$\mathbf{v}^{n+1} = \mathbf{v}^{*} + \frac{1}{2}\Delta t[\mathbf{a}^{n+1} - \mathbf{a}^n], \tag{2.22}$$

where $\mathbf{r}$, $\mathbf{v}$ and $\mathbf{a}$ are the particle's position, velocity and acceleration, respectively, and n is the timestep number. The error in the predictor step is then checked to be below a tolerance, ϵ, typically set to 10^{-2}

$$\frac{|v^{n+1} - v^{*}|}{|v^{\mathrm{mag}}|} < \epsilon, \tag{2.23}$$

where v^{mag} is the mean velocity of all particles. If the error is too large Equations 2.21 and 2.22 are recalculated and the error re-checked.

The maximum timestep for stability is given by the Courant condition (Courant et al., 1928):

$$\Delta t^a < C\frac{h}{v_{max}}, \tag{2.24}$$

where v_{max} is the maximum velocity over the particle's neighbours and C is the Courant number, a dimensionless constant less than unity which ensures stability. This condition implies that in one timestep a particle can't move more than a fraction of its smoothing length as set by the Courant number, and $C = 0.3$ by default (Lattanzio et al., 1986). For computational efficiency `PHANTOM` allows for particles to have individual timesteps, which breaks the time-reversibility of the leapfrog scheme, meaning that energy is no longer exactly conserved.

2.2.4 Viscosity

In Section 2.2.2 the derivation of Equation 2.15 has built into it the assumption that the Lagrangian is differentiable, that is to say we do not allow discontinuous solutions and our equations of motion break down at shocks. This can be solved with the introduction of an artificial viscosity (Von Neumann and Richtmyer, 1950). This artificial viscosity acts to spread the shock over smallest resolution scale, in this case the smoothing length, removing the discontinuity. In practise this is done using an artificial viscosity term, $q_{\rm AV}$, as in Monaghan (1997), giving a modified equation of motion:

$$\frac{\mathrm{d}\mathbf{v}_a}{\mathrm{d}t} = -\sum_b m_b \left[\frac{P_a + q^a_{\rm AV}}{\Omega_a \rho_a^2}\frac{\partial W_{ab}(h_a)}{\partial \mathbf{r}_a} + \frac{P_b + q^b_{\rm AV}}{\Omega_b \rho_b^2}\frac{\partial W_{ab}(h_b)}{\partial \mathbf{r}_b}\right], \tag{2.25}$$

with the artificial viscosity term

$$q^a_{\rm AV} = \begin{cases} -\frac{1}{2}\rho_a v_{{\rm sig},a}\mathbf{v}_{ab}\cdot\hat{\mathbf{r}}_a, & \mathbf{v}_{ab}\cdot\hat{\mathbf{r}}_a < 0; \\ 0, & \text{otherwise}, \end{cases} \tag{2.26}$$

where $\mathbf{v}_{ab} \equiv \mathbf{v}_a - \mathbf{v}_b$, $\mathbf{r}_{ab} \equiv (\mathbf{r}_a - \mathbf{r}_b)/|\mathbf{r}_a - \mathbf{r}_b|$, a $v_{\rm sig}$ is the maximum signal speed, given by

$$v_{{\rm sig},a} = \alpha^{\rm AV}_a c_{s,a} + \beta^{\rm AV}|\mathbf{v}_{ab}\cdot\hat{\mathbf{r}}_a|. \tag{2.27}$$

$\beta_{\rm AV}$ mimics a Von Neumann and Richtmyer (1950) term and is set to 2 by default to prevent particle penetration (Lattanzio et al., 1986) and $\alpha^{\rm AV}_a \in [0, 1]$ is controlled by the Morris and Monaghan (1997) switch to reduce dissipation away from shocks.

In our application we wish to have an artificial viscosity that represents Equation 1.24, the Shakura and Sunyaev (1973) α-disc viscosity, requiring a few changes to be made. The viscosity term must be applied for both approaching and receding pairs of particles; $\beta^{\rm AV}$ is set to zero for receding particles, though is still used for approaching particles to prevent

particle penetration; $\alpha^{\rm AV}$ is set to be constant, removing the shock detection switch; and the artificial viscosity term is multiplied by a factor of $h/|\mathbf{r}_{ab}|$. This leads to an artificial viscosity term in the form

$$q^a_{\rm AV} = -\frac{\rho_a h_a}{2|\mathbf{r}_{ab}|} \begin{cases} (\alpha^{\rm AV}_a c_{s,a} + \beta^{\rm AV}|\mathbf{v}_{ab}\cdot\hat{\mathbf{r}}_a|)\mathbf{v}_{ab}\cdot\hat{\mathbf{r}}_a, & \mathbf{v}_{ab}\cdot\hat{\mathbf{r}}_a < 0; \\ \alpha^{\rm AV}_a c_{s,a}\mathbf{v}_{ab}\cdot\hat{\mathbf{r}}_a, & \text{otherwise}, \end{cases} \tag{2.28}$$

This new formalisation gives shear and bulk coefficients as (e.g. Monaghan, 2005; Lodato and Price, 2010)

$$\nu \approx \frac{1}{10}\alpha^{\rm AV} c_s h, \tag{2.29}$$

$$\zeta = \frac{5}{3}\nu \approx \frac{1}{6}\alpha^{\rm AV} c_s h. \tag{2.30}$$

Combining Equations 1.24 and 2.29 allows $\alpha_{\rm SS}$ to be determined from $\alpha^{\rm AV}$ via

$$\alpha_{\rm SS} = \frac{\alpha^{\rm AV}}{10}\frac{\langle h\rangle}{H}, \tag{2.31}$$

where $\langle h\rangle$ is the azimuthally averaged smoothing length.

2.2.5 Sink Particles

To model the central binary, we use a pair of sink particles (Bate et al., 1995). The only interactions sinks experience is via gravity, both from the other sink and from the SPH particles in the disc. This leads to an equation of motion for sink i:

$$\frac{{\rm d}v_i}{{\rm d}t} = -\sum_{j=1}^{N_{sink}} \frac{GM_j}{|r_i - r_j|^2}\hat{r}_{ij} - \sum_{a=1}^{N_{gas}} \frac{Gm_a}{|r_a - r_i|^2}\hat{r}_{ia}. \tag{2.32}$$

Consequently, an interaction term needs to be added to the acceleration of the SPH particles, given by:

$$a^a_{\text{sink-gas}} = -\sum_{j=1}^{N_{sink}} \frac{GM_j}{|r_a - r_j|^2}\hat{r}_{aj}. \tag{2.33}$$

SPH particles are accreted onto the sinks if they pass within $0.5r_{acc}$ of the sink, where r_{acc} is the effective size of the sink. If a particle passes between $0.5r_{acc}$ and r_{acc} it will only be accreted if it is both bound to that sink (and no other) and its specific angular momentum is less than that of a Keplerian orbit at r_{acc}. When particle a is accreted onto sink i the mass, position, velocity, acceleration and spin angular momentum of the sink are updated in the following way that conserves mass, linear momentum and angular

momentum, but not energy:

$$M_i = M_i + m_a, \tag{2.34}$$

$$r_i = \frac{r_i M_i + r_a m_a}{M_i + m_a}, \tag{2.35}$$

$$v_i = \frac{v_i M_i + v_a m_a}{M_i + m_a}, \tag{2.36}$$

$$a_i = \frac{a_i M_i + a_a m_a}{M_i + m_a}, \tag{2.37}$$

$$S_i = S_i + \frac{M_i m_a}{M_i + m_a}[(r_a - r_i) \times (v_a - v_i)]. \tag{2.38}$$

2.2.6 Kernel Interpolation

Converting data from a set of discrete SPH particles to a continuous field requires interpolating between the particles. To do this we must first start with the identity

$$A(\mathbf{r}) = \int A(\mathbf{r}')\delta(\mathbf{r}')\mathrm{d}\mathbf{r}', \tag{2.39}$$

where A is any scalar field and δ is the Dirac-delta function. This can be approximated by replacing δ with the smoothing function, giving:

$$A(\mathbf{r}) = \int A(\mathbf{r}')W(\mathbf{r} - \mathbf{r}', h)\mathrm{d}\mathbf{r}' + \mathcal{O}(\mathrm{h}^2). \tag{2.40}$$

We can discretise this by replacing the integral with a summation, replacing the density element with the particle mass, and ignoring second order terms as follows:

$$\begin{aligned} \langle A(\mathbf{r})\rangle &= \int \frac{A(\mathbf{r}')}{\rho(\mathbf{r}')}W(\mathbf{r} - \mathbf{r}', h)\rho(\mathbf{r}')\mathrm{d}\mathbf{r}' \\ &\simeq \sum_{b=0}^{N_{neigh}} m_b \frac{A_b}{\rho_b} W(\mathbf{r} - \mathbf{r}', h), \end{aligned} \tag{2.41}$$

giving us a way to interpolate any scalar property $A(\mathbf{r})$ at any point in space using only the mass, density, and A of the neighbouring particles. Note that if we chose A to be the density here we recover Equation 2.5, the SPH density estimate.

The gradient of any scalar quantity can be found by taking the derivative of Equation 2.41 as follows:

$$\begin{aligned} \langle \nabla A(\mathbf{r})\rangle &= \frac{\partial}{\partial \mathbf{r}} \int \frac{A(\mathbf{r}')}{\rho(\mathbf{r}')}W(\mathbf{r} - \mathbf{r}', h)\rho(\mathbf{r}')\mathrm{d}\mathbf{r}' \\ &\simeq \sum_{b=0}^{N_{neigh}} m_b \frac{A_b}{\rho_b} \nabla W(\mathbf{r} - \mathbf{r}', h). \end{aligned} \tag{2.42}$$

Vector quantities can be interpolated in the same way simply by replacing A with $\mathbf{A}$ in Equation 2.41, giving:

$$\langle \mathbf{A}(\mathbf{r}) \rangle \simeq \sum_{\mathrm{b}=0}^{\mathrm{N_{neigh}}} \mathrm{m_b} \frac{\mathbf{A_b}}{\rho_\mathrm{b}} \mathrm{W}(\mathbf{r} - \mathbf{r}', \mathrm{h}). \tag{2.43}$$

Similarly, the divergence and curl can be found using the same method as in Equation 2.42, giving:

$$\langle \nabla \cdot \mathbf{A}(\mathbf{r}) \rangle \simeq \sum_{b=0}^{N_{neigh}} m_b \frac{\mathbf{A_b}}{\rho_b} \nabla \cdot W(\mathbf{r} - \mathbf{r}', h), \tag{2.44}$$

$$\langle \nabla \times \mathbf{A}(\mathbf{r}) \rangle \simeq \sum_{b=0}^{N_{neigh}} m_b \frac{\mathbf{A_b}}{\rho_b} \nabla \times W(\mathbf{r} - \mathbf{r}', h). \tag{2.45}$$

2.3 Radiative Transfer

2.3.1 The Radiative Transfer Equation

Radiative transfer describes the transfer of energy by means of electromagnetic radiation travelling through a medium. As such, understanding of radiative transfer is crucial in order to calculate synthetic observations of circumbinary discs.

We start by defining a radiation field with specific intensity $I(\mathbf{x}, \mathbf{n}, \lambda)$, where $\mathbf{x}$ is position, $\mathbf{n}$ is a unit vector in the direction of the radiation, and λ is the wavelength. The specific intensity represents the amount of energy carried by the radiation per unit wavelength interval across a unit area perpendicular to $\mathbf{n}$ per unit solid angle per unit time. The general form of the radiative transfer equation (RTE) is given by (see: Chandrasekhar, 1960; Rybicki and Lightman, 1979):

$$\mathbf{n} \cdot \nabla I(\mathbf{x}, \mathbf{n}, \lambda) = -\kappa(\mathbf{x}, \lambda)\rho(\mathbf{x})I(\mathbf{x}, \mathbf{n}, \lambda) + j(\mathbf{x}, \mathbf{n}, \lambda). \tag{2.46}$$

The term on the left hand side represents the spatial change in intensity. The first term on the right hand side represents extinction, that is the loss of energy as radiation is absorbed when it passes through matter, where $\kappa(\mathbf{x}, \lambda)$ is the extinction coefficient, also known as opacity, and $\rho(\mathbf{x})$ is the mass density. This is a sink term, that is it removes energy from the system. The final term is a source term that represents, as the name suggests, new sources that inject photons into the system.

If we introduce a distance s defined along the path $\mathbf{x}$ in propagation direction $\mathbf{n}$ Equation 2.46 can be rewritten as:

$$\frac{\mathrm{d}I(s, \lambda)}{\mathrm{d}s} = -\kappa(s, \lambda)\rho(s)I(s, \lambda) + j(s, \lambda), \tag{2.47}$$

which has the solution

$$I(s,\lambda) = \int_{-\infty}^{\infty} j(s',\lambda) \exp\left(-\tau(s',s,\lambda)\right) \mathrm{d}s', \tag{2.48}$$

where the optical thickness between two points is defined as

$$\tau(s_1,s_2,\lambda) = \int_{s_1}^{s_2} \kappa(s,\lambda)\rho(s)\mathrm{d}s. \tag{2.49}$$

This solution shows that the intensity at any point along the path s is simply the emission from all previous points s' reduced by a factor of $\exp\left(-\tau(s',s,\lambda)\right)$ due to extinction. This solution, however, relies on the assumption that j does not depend on I, an assumption that does not hold in general. Furthermore, Equation 2.46 is the simplest form of the RTE, and can be made more rigorous by considering the physical processes that go into it.

The simplest processes to consider are primary emission and absorption. Primary emission for our sake is stellar emission and emission line radiation from ionised gas. It is captured in the source term in Equation 2.46, and is written as j_* when considering stellar emission. Absorption is the process by which gas molecules and dust grains convert incident radiation into internal energy and is included in the extinction term as κ_{abs}, the absorption coefficient. κ_{abs} depends on the size, shape, and composition of the dust grains and in principle can be found at any wavelength. In practise, however, modelling absorption from dust grains is an ongoing area of research (e.g. Purcell and Pennypacker, 1973; Draine, 1988; Min et al., 2005). Adding these terms to Equation 2.46 does not increase its mathematical complexity and it still has a solution of the form given in Equation 2.48.

One possible outcome of an interaction between a gas or dust particle is scattering. Rather than removing or adding radiation, scattering is the process by which a photon changes direction. This adds both an additional sink and source term to the RTE; a sink term for a photon travelling in direction $\mathbf{n}'$ and a source term for the photon now traveling in the new direction $\mathbf{n}$. The efficiency of scattering is quantified by the scattering coefficient κ_{sca}. The scattering phase function $\Phi(\mathbf{n},\mathbf{n}',\mathbf{x},\lambda)$ describes the probability that a photon travelling in direction $\mathbf{n}'$ will be travelling in direction $\mathbf{n}$ after scattering at position $\mathbf{x}$ and has the normalisation condition

$$\int_{4\pi} \Phi(\mathbf{n},\mathbf{n}',\mathbf{x},\lambda)\mathrm{d}\Omega' = \int_{4\pi} \Phi(\mathbf{n},\mathbf{n}',\mathbf{x},\lambda)\mathrm{d}\Omega = 1, \tag{2.50}$$

that is, the probability over all solid angles is 1. Adding scattering to the RTE gives:

$$\begin{aligned}\mathbf{n}\cdot\nabla I(\mathbf{x},\mathbf{n},\lambda) = &-\kappa_{\mathrm{ext}}(\mathbf{x},\lambda)\rho(\mathbf{x})I(\mathbf{x},\mathbf{n},\lambda) + j_*(\mathbf{x},\mathbf{n},\lambda) \\ &+ \kappa_{\mathrm{sca}}(\mathbf{x},\lambda)\rho(\mathbf{x}) \int_{4\pi} \Phi(\mathbf{n},\mathbf{n}',\mathbf{x},\lambda) I(\mathbf{x},\mathbf{n}',\lambda)\mathrm{d}\Omega',\end{aligned} \tag{2.51}$$

where $\kappa_{\rm ext} = \kappa_{\rm abs} + \kappa_{\rm sca}$. Dust scattering is a highly anisotropic process, so correct modelling of this anisotropy via the scattering phase function is important in order to produce accurate calculations. Perhaps the most popular parameterisation is the Henyey and Greenstein (1941) phase function, which introduces anisotropy factor g to give a phase function in 2-dimensions of:

$$\Phi(\theta) = \frac{1}{4\pi} \frac{1 - g^2}{(1 + g^2 - 2G\cos\theta)^{3/2}}. \tag{2.52}$$

More complex phase functions exist, giving higher accuracy at the cost of computational efficiency (e.g: Kattawar, 1975; Hong, 1985; Draine, 2003).

Since dust is also able to emit radiation we must add another source term to the RTE. Large dust grains are assumed to be in local thermal equilibrium with the radiation field and emit as a blackbody, giving rise to a source term:

$$j_{\rm d}(\mathbf{x}, \mathbf{n}, \lambda) = \kappa_{\rm abs}(\lambda)\rho(\mathbf{x})B(T, \lambda), \tag{2.53}$$

where $B(T, \lambda)$ is the Planck function and T is the local equilibrium temperature. The assumption that the dust is in thermal equilibrium doesn't hold for small grains due to their low heat capacities which lead to large temperature fluctuations. For small grains the source term becomes

$$j_{\rm d}(\mathbf{x}, \mathbf{n}, \lambda) = \kappa_{\rm abs}(\lambda)\rho(\mathbf{x}) \int_0^\infty P(T, \mathbf{x})B(T, \lambda), \tag{2.54}$$

where $P(T, \mathbf{x})$ is the temperature distribution of the small grains.

$\kappa_{\rm abs}(\lambda)$, as well as $\kappa_{\rm sca}(\lambda)$, can be computed for dust grains with the Mie theory if one assumes they are spherical and homogenous. For a given size and composition distribution $f(\mathbf{x}, a)$ the local opacities are given by;

$$\kappa_{\rm abs/sca}(\mathbf{x}, \lambda) = \int_{a_{\rm min}}^{a_{\rm max}} \pi a^2 Q_{\rm abs/sca}(\lambda, a) f(\mathbf{x}, a) {\rm d}a, \tag{2.55}$$

where $Q_{\rm abs}(\lambda, a)$ and $Q_{\rm sca}(\lambda, a)$ are the absorption and scattering cross-sections of a grain with size a at wavelength λ, respectively.

Thus far we have only considered the specific intensity $I(\mathbf{x}, \mathbf{n}, \lambda)$ of the radiation field, however this is an incomplete picture since it does not take into account polarised light. Even for unpolarised light, scattering events can lead to polarisation, especially when scattered off aligned dust grains (e.g. Schmidt, 1973; Fischer et al., 1994, 1996). Polarisation is described using the Stokes vector $\mathbf{S} = (I, Q, U, V)$, where I still represents the specific intensity, Q and U represent linearly polarised intensity in axes rotated 45°

from each other, and V represents circularly polarised intensity. The introduction of the Stokes vector turns the RTE from a single equation to a set of four coupled equations given by:

$$\begin{aligned}\mathbf{n}\cdot\nabla\mathbf{S}(\mathbf{x},\mathbf{n},\lambda) = &-\kappa_{\rm ext}(\mathbf{x},\lambda)\rho(\mathbf{x})\mathbf{S}(\mathbf{x},\mathbf{n},\lambda) + j_*(\mathbf{x},\mathbf{n},\lambda) + j_{\rm d}(\mathbf{x},\mathbf{n},\lambda)\\ &+\kappa_{\rm sca}(\mathbf{x},\lambda)\rho(\mathbf{x})\int_{4\pi}\mathcal{M}(\mathbf{n},\mathbf{n}',\mathbf{x},\lambda)\mathbf{S}(\mathbf{x},\mathbf{n}',\lambda){\rm d}\Omega', \end{aligned} \tag{2.56}$$

where $\mathcal{M}(\mathbf{n},\mathbf{n}',\mathbf{x},\lambda)$, known as the Mueller matrix or scattering matrix, is the coupling term that describes the changes to the Stokes vector due to scattering.

2.3.2 Monte Carlo Method

The anisotropic scattering from dust grains makes finding an analytical solution to the RTE impossible, thus numerical methods must be employed. The most popular method is the Monte Carlo (MC) method. This is the method we will focus on in this section, focusing specifically on the implementation in `MCFOST`. Other methods exist, such as ray tracing and finite difference, which will not be covered here (see Pinte et al., 2009; Steinacker et al., 2013, for an overview).

MC works by modelling the radiation flow as photon packets which propagate through the disc. Their propagation is governed by appropriately chosen probability density functions (PDFs) that describe the material in the disc. Upon leaving the boundary of the computational domain these photon packets are then used to create intensity and channel maps or SEDs.

Before considering the propagation of the photon packets, however, the computational domain must first be specified. When using `MCFOST` to create an image from a `PHANTOM` output, the computational domain is constructed from the Vorenoi tessellation (Voronoï, 1908) of the distribution of SPH particles, i.e. each cell corresponds to the position of an SPH particle and the grid boundaries are the planes that are equidistant to the two closest SPH particles. This allows particle properties to be mapped onto the grid without interpolation. Once this grid is constructed we can now consider the behaviour of the photon packets.

A photon packet's journey begins when it is injected into the computational domain. In this work this physically represents emission from the central stars. The initial position and propagation direction are sampled from the PDF given by:

$$p(\mathbf{x},\mathbf{n}) = \frac{j_*(\mathbf{x},\mathbf{n},\lambda)}{L_{\rm tot}}, \tag{2.57}$$

where $p(\mathbf{x}, \mathbf{n})$ is the PDF and $L_{\rm tot}$ is the total luminosity of the source.

Once the photon packet has been launched the next step is to determine the distance it will travel before an interaction, or indeed whether it will escape the computational domain, given a large enough propagation distance. The optical depth is sampled from the PDF given by $p(\tau) = \exp(-\tau)$. This is then converted to a physical distance, l, by integrating Equation 2.49 until the following equality is satisfied:

$$\tau(\lambda) = \int_0^l \kappa_{\rm ext}(\mathbf{x}, \lambda)\rho(\mathbf{x})\mathrm{d}s. \tag{2.58}$$

Once the position, $\mathbf{x}$, of interaction is found the probability of a scattering is found via the local albedo:

$$p_{\rm sca} = \mathcal{A}(\mathbf{x}, \lambda) = \frac{\int_{a_{\rm min}}^{a_{\rm max}} \pi a^2 Q_{\rm sca}(\lambda, a) f(\mathbf{x}, a)\mathrm{d}a}{\int_{a_{\rm min}}^{a_{\rm max}} \pi a^2 Q_{\rm ext}(\lambda, a) f(\mathbf{x}, a)\mathrm{d}a}, \tag{2.59}$$

where $\mathcal{A}(\mathbf{x}, \lambda)$ is the local albedo, $p_{\rm sca}$ is the probability of scattering, and it follows that the probability of absorption is $p_{\rm abs} = 1 - p_{\rm sca}$.

Once a scattering interaction has occurred the photon packet's new propagation direction must be found. The scattering direction is defined by two angles, the scattering angle θ and the azimuth angle ϕ. Rewriting the elements of the scattering matrix as a function of scattering angle, position, and wavelength allows the scattering angle to be sourced from the cumulative distribution function:

$$F(\theta) = \frac{\int_0^\theta \mathcal{M}_{11}(\theta', \mathbf{x}, \lambda)\sin(\theta')\mathrm{d}\theta'}{\int_0^\pi \mathcal{M}_{11}(\theta', \mathbf{x}, \lambda)\sin(\theta')\mathrm{d}\theta'}. \tag{2.60}$$

If the incoming photon packet is linearly unpolarised the azimuth distribution is isotropic. For a photon packet with non-zero linear polarisation, $\mathbf{S} = \sqrt{Q^2 + U^2}/I$, the azimuth is defined relative to the direction of polarisation and sourced from the cumulative distribution function:

$$F_\theta(\phi) = \frac{1}{2_\pi}\left(\phi - \frac{\mathcal{M}_{11}(\theta, \mathbf{x}, \lambda) - \mathcal{M}_{12}(\theta, \mathbf{x}, \lambda)}{\mathcal{M}_{11}(\theta, \mathbf{x}, \lambda) + \mathcal{M}_{12}(\theta, \mathbf{x}, \lambda)} P \frac{\sin(\phi)}{2}\right), \tag{2.61}$$

where θ is taken from Equation 2.60 (Solc, 1989).

Naturally, if an interaction is not a scattering event it must be an absorption event, which acts to heat the material in the disc. `MCFOST` works on two extreme assumptions; either the gas-dust mixture is perfectly coupled and in local thermal equilibrium, or there is no thermal coupling at all. In the case of perfect coupling the temperature of each cell is given by the radiative equilibrium equation:

$$4\pi \int_0^\infty \kappa_{{\rm abs},i}(\lambda) B(T_i, \lambda)\mathrm{d}\lambda = \Gamma_{{\rm abs},i}, \tag{2.62}$$

where i refers to the cell index and $\Gamma_{\mathrm{abs},i}$ is the energy absorption rate. By considering only passive heating we can rewrite the energy absorption rate in terms of the mean intensity, $J(\lambda)$:

$$4\pi \int_0^\infty \kappa_{\mathrm{abs},i}(\lambda) B(T_i, \lambda) \mathrm{d}\lambda = 4\pi \int_0^\infty \kappa_{\mathrm{abs},i}(\lambda) J(\lambda) \mathrm{d}\lambda, \tag{2.63}$$

and any extra sources of heating can be taken into account by adding the corresponding term to the right hand side of this equation. Each time a photon packet γ of wavelength λ passes through a cell the distance Δl_γ that packet travels within the cell is computed. The mean intensity can then be derived following Lucy (1999), replacing the right hand side of Equation 2.63:

$$4\pi \int_0^\infty \kappa_{\mathrm{abs},i}(\lambda) B(T_i, \lambda) \mathrm{d}\lambda = \frac{L_*}{V_i} \sum_{\lambda,\gamma} \frac{\kappa_{\mathrm{abs},i}(\lambda) \Delta l_\gamma}{N_\gamma}, \tag{2.64}$$

where $L*$ is the stellar luminosity, V_i is the volume of cell i, and N_γ is the number of photon packets with wavelength γ. This gives rise to a source term in the form of Equation 2.53.

In the case where the gas and dust, or dust grains of different sizes, are not thermally coupled the radiative equilibrium equation must be rewritten for each different species. As this is computationally expensive Bjorkman and Wood (2001) came up with the concepts of immediate re-emission and temperature correction to greatly speed up calculations. In effect this means that any photon packet that gets absorbed is immediately re-emitted with a wavelength chosen by taking into account a corrected temperature given by the PDF:

$$\rho(\gamma) \propto \kappa_{\mathrm{abs},i}(\lambda) \frac{\mathrm{d}B(T_i, \lambda)}{\mathrm{d}T}. \tag{2.65}$$

2.3.3 Intensity and Channel Maps

When computing synthetic maps there are two main methods for sampling the radiation field; photon packets with the same energy, regardless of wavelength, or photon packets with the same number of photons, and thus different energy at each wavelength. The former leads to a better convergence of the temperature distribution while the latter allows for more efficient computation of the maps. `MCFOST` strikes a balance between the two by using a two step process.

In the first step the temperature distribution is calculated. Here photon packets are generated at the stellar surface and propagated until they exit the computational domain and each photon packet has the same energy $\epsilon = L_* N_{\gamma,\mathrm{step1}}$. This reduces the noise in the temperature distribution, especially at low optical depth, but is inefficient for calculating

synthetic maps.

In the second step the map is calculated from the temperature distribution found in step 1. Here the number of photon packets, $N_{\gamma,\text{step2}}$, is held constant at all wavelengths, leading to a comparable noise level in all wavelength bins. In this step photon packets are always scattered and never absorbed but at each interaction the Stokes vector is weighted by the probability of scattering, p_{sca}, to take into account the energy loss from absorption. This allows all photons to exit the disc and contribute to the map with a reduced weight. Unlike in step 1, packets are now emitted from the disc as well as the stellar surface. These packets are generated with a luminosity that is determined by the total energy emitting by the star and disc at their given wavelength:

$$\epsilon = \frac{L_*(\lambda) + \sum_i w_i(\lambda) L_i(\lambda)}{N_{\gamma,\text{step2}}}. \tag{2.66}$$

These packets are randomly emitted from the stellar surface with probability:

$$p_* = \frac{L_*(\lambda)}{L_*(\lambda) + \sum_i w_i(\lambda) L_i(\lambda)}, \tag{2.67}$$

and from the disc, in cell i, with probability:

$$p_i = \frac{w_i(\lambda) L_i(\lambda)}{L_*(\lambda) + \sum_i w_i(\lambda) L_i(\lambda)}, \tag{2.68}$$

where the luminosities are given by:

$$L_*(\lambda) = 4\pi R_*^2 B(T_*, \lambda), \tag{2.69}$$

for the star and:

$$L_i(\lambda) = 4\pi m_i \kappa_{\text{abs},i}(\lambda) B(T_i, \lambda), \tag{2.70}$$

for the disc, m_i is the mass of cell i and $w_i(\lambda)$ is its weighting. To prevent any photon packets being generated so deep in an optically thick region of the disc that they wouldn't reach the surface with an appreciable energy a "dark zone" is defined for each wavelength. This dark zone is the region where the optical depth $\tau(\lambda) \geq 30$ to get out of the computational domain in any direction. $w_i(\lambda) = 0$ inside this zone, ensuring no photon packets are generated there, and $w_i(\lambda) = 1$ outside it. Furthermore, any photon generated outside the dark zone that enter it during their random walk are killed.

Intensity maps are calculated from the continuum at a given wavelength. Channel maps, on the other hand, consider only a single spectral line. Spectral lines are subject to a number of broadening effects resulting in a profile of finite thickness in wavelength space. The Doppler effect shifts the wavelength due to the line of sight velocity of the emitting material. Each wavelength contributing to the spectral profile can be converted to a velocity, giving rise to channel maps which image the disc in slices of line of sight velocity.

2.3.4 Moment Maps

From the channel maps it is possible to calculate moment maps, each of which gives different imformation about the material in the disc. The moment 0 map is calculated as $\int I(\mathbf{x}, \mathbf{n}, v)\mathrm{d}v$ for each pixel, the sum of intensity of all channels, and traces the flux density. While dense regions tend to be more luminous, luminosity doesn't only depend on density. Of particular importance is the dependence of luminosity on temperature, which means that a less dense but hotter material closer to the binary can in theory be more luminous than a more dense but colder region further out. In practise, however, the densest regions of the disc are those closest to the binary, so the moment 0 map roughly traces column density. It is also important to note that for optically thick material this probes the surface layers of the disc, while for optically thin material this probes the disc midplane.

The moment 1 map is calculated as $\int I(\mathbf{x}, \mathbf{n}, v)v\mathrm{d}v / \int I(\mathbf{x}, \mathbf{n}, v)\mathrm{d}v$. This is a map of the average velocity along the observer's line of sight weighted by intensity, thus the signal is strongest for discs which are edge-on to the observer. Finally, the moment 2 map is calculated as $\int I(\mathbf{x}, \mathbf{n}, v)v^2\mathrm{d}v / \int I(\mathbf{x}, \mathbf{n}, v)\mathrm{d}v$. This is a measure of the velocity dispersion.

Chapter 3

On the Cavity Size in Circumbinary Discs

3.1 Introduction

As discussed in Section 1.4 the long-term evolution of an inclined circumbinary disc is not well understood. To investigate this we perform a series of 3-dimensional SPH simulations of inclined circumbinary discs. Before considering inclined discs, however, we first model coplanar discs, varying the disc viscosity, as well as the binary eccentricity and mass ratio to investigate what the final cavity size can tell us about unseen binary companions and about the disc properties. The work in this chapter has been published in Hirsh et al. (2020).

3.2 Methods

3.2.1 Initial Conditions

Using the SPH code `PHANTOM` (Price et al., 2018b) we model a gas disc consisting of one million particles initially placed in a circumbinary disc extending from 1.4 to 14.5 times the binary semi-major axis, with the binary modelled as a pair of sink particles as described in Section 2.2.5. We simulate binaries with mass ratios of $q = 0.01, 0.1, 0.3$ and 0.5 with $q = M_2/(M_1 + M_2)$, where M_1 and M_2 are the mass of the primary and secondary, respectively. We use a disc mass of $M_{\rm disc} = 0.0001M_1$, in order to reduce the effects of the disc gravity on the binary orbit. This low mass leads to a negligible disc self-gravity, so we do not include it in our simulations. We assume a surface density profile $\Sigma \propto R^{-p}$, with $p = 1.0$. We prescribe a locally isothermal equation of state, that is $P = c_s^2(R)\rho$, with sound speed varying as $c_s \propto R^{-w}$, with $w = 0.25$. This leads to a temperature profile $T \propto R^{-2w}$ and a disc aspect ratio varying as $H/R \propto R^{1/2-w}$. This allows us to set the

Table 3.1: Simulation parameters. We vary the binary mass ratio, disc inclination, and disc scale height. Varying the scale height corresponds to the value of artificial viscosity given beneath it.

Parameter	Fiducial value	Other explored values
q	0.1	0.01, 0.3, 0.5
$M_{\rm disc}/M_1$	0.0001	
$R_{\rm in}/a$	1.4	
$R_{\rm out}/a$	14.5	
p	1.0	
w	0.25	
α	0.005	
inclination	0°	22.5°, 45°, 90°
Viscosity-dependent parameters		
$(H/R)_{\rm in}$	0.05	0.01, 0.02, 0.04, 0.06, 0.08, 0.10, 0.12
$\alpha_{\rm AV}$	0.20	0.07, 0.11, 0.17, 0.22, 0.27, 0.31, 0.35

sound speed, temperature and aspect ratio by specifying the aspect ratio at the disc inner edge. We simulate discs with $(H/R)_{\rm in} = 0.01, 0.02, 0.04, 0.05, 0.06, 0.08, 0.10$ and 0.12. The setup for our fiducial simulation, as well as the full parameter space investigated, is outlined in Table 3.1.

3.2.2 Disc Viscosity

We prescribe an α disc (see Sections 1.3.3 and 2.2.4), setting $\alpha_{\rm AV}$ such that the average $\alpha = 0.005$. This allows us to vary the viscosity by varying the scale height of the disc. The corresponding viscous time $t_{\rm visc} = R^2/\nu$, at $R = R_{\rm in}$, is given in terms of the orbital time $(2\pi/\Omega)$ according to

$$t_{\rm visc} \approx 12,800 \text{ orbits} \left(\frac{\alpha}{0.005}\right)^{-1} \left(\frac{H/R}{0.05}\right)^{-2}. \tag{3.1}$$

For the discs we investigate this gives a $t_{\rm visc}$ that varies from roughly 2,200 orbits for $(H/R)_{\rm in} = 0.12$, to roughly 320,000 orbits for $(H/R)_{\rm in} = 0.01$. Physically it is more sensible to consider $t_{\rm visc}$ at the cavity edge ($R_{\rm cav}$), but since this varies throughout and between simulations we consider $t_{\rm visc}$ at $R_{\rm in}$ and note a discrepancy of a factor of $R_{\rm cav}/R_{\rm in}$.

3.2.3 Cavity Size

We azimuthally average the surface density and define the half-maximum radius to be the radius at which the surface density first reaches half its maximum, with a similar

definition for the quarter-maximum density. Following the prescription in AL94, we then take the cavity size to be the radius at half-maximum, with a symmetric error taken as the difference between the radii at half-maximum and quarter-maximum.

3.3 Results

3.3.1 Time Evolution

Figure 3.1 shows surface density rendered face-on views of the cavity opening process for a coplanar disc with $(H/R)_{\rm in} = 0.05$ and $q = 0.1$ and eccentricities ranging from $e = 0$ to $e = 0.8$. The cavity size increases with time (top to bottom) until reaching an equilibrium after several thousand orbits. After 10,000 binary orbits the background surface density is smaller due to viscous disc spreading.

Figure 3.2 quantifies the cavity size as a function of time and initial binary eccentricity. The top panel shows the evolution on tens of dynamical timescales (a dynamical timescale being $\lesssim 10$ binary orbits at $R_{\rm cav}$). The cavity is opened on this timescale and the size appears to stabilise between $2-3$ times the semi-major axis depending on the eccentricity of the binary. Evolving the system on the viscous timescale ($\sim 10,000$ binary orbits) shows the cavity continue to grow to $2.5-3.5$ times a for eccentric binaries (bottom panel). The circular case is unique in that it reaches a maximum cavity size of the order of hundreds of binary orbits, while eccentric binaries continue to grow their cavities for thousands of binary orbits.

3.3.2 Binary Orbital Eccentricity

Figure 3.1 shows the effect of binary eccentricity on the cavity size. Cavity size increases with increasing eccentricity. This is shown quantitatively in Fig. 3.3. At early (100 binary orbits; green line) and late (10,000 binary orbits; black line) stages the cavity size increases with binary orbital eccentricity, consistent with both AL94 and ML15. After 1000 binary orbits (red line), however, we see a turnover in the cavity size due to the circular binaries reaching a maximum cavity size before eccentric ones. This turnover is only temporary though, and disappears once the eccentric binaries reach a maximum cavity size. Thun et al. (2017) also find a turnover in the cavity size, however theirs persists up to 16,000 binary orbits, and the minimum is seen at $e \approx 0.18$ while ours is at $e \approx 0.1$.

The exact values for the cavity size also show some discrepancies. Thun et al. (2017) found cavity sizes between 4 and 7 times the binary semi-major axis, nearly double the

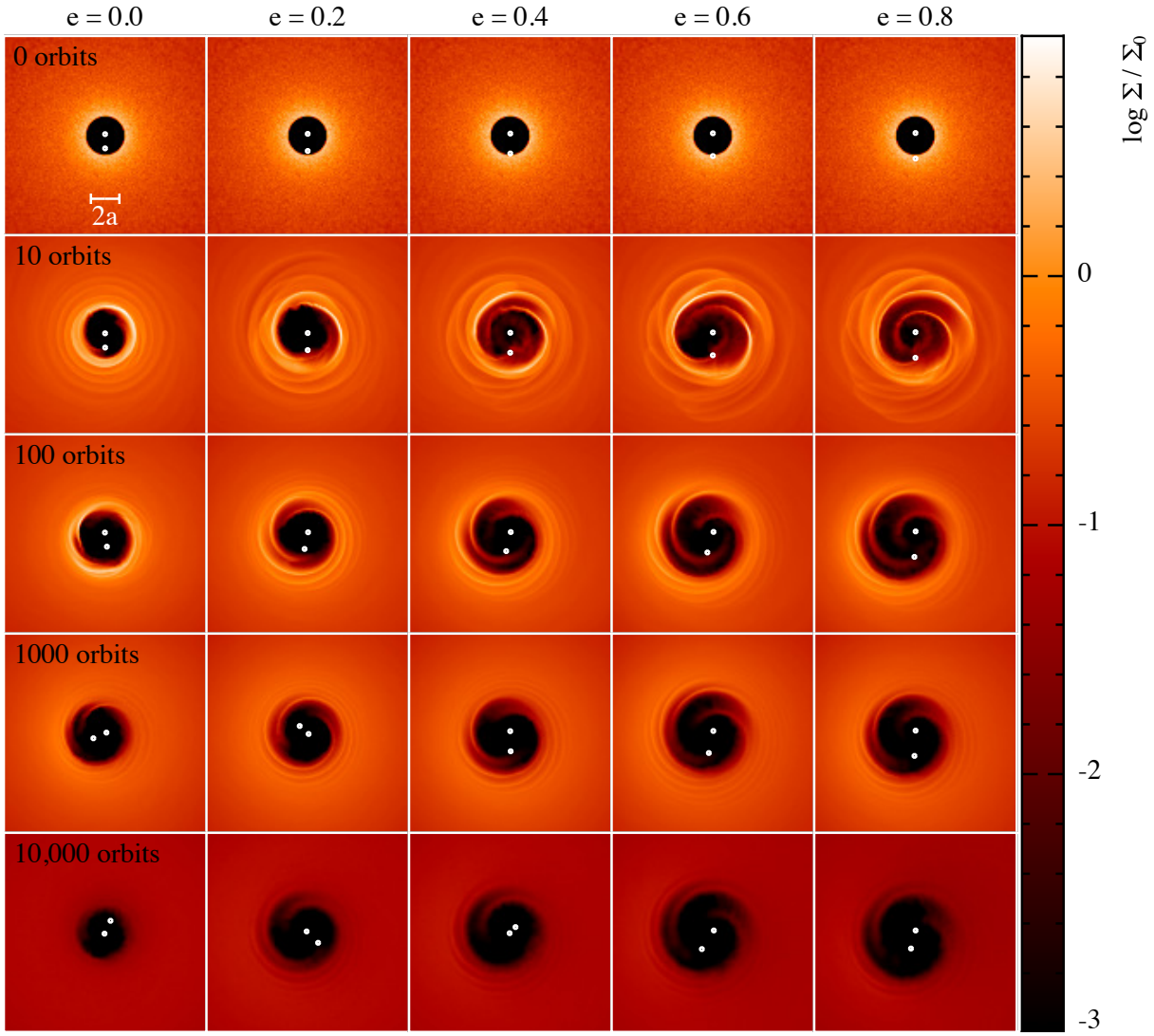

Figure 3.1: Surface density rendered face-on views of the evolution of coplanar discs with $(H/R)_{\rm in} = 0.05$ surrounding a binary with $q = 0.1$. Eccentricity increases from left to right and time increases from top to bottom.

values found by our work, as well as that of AL94 and ML15 (dashed lines in Fig. 3.3). We discuss this difference in Section 3.4.

3.3.3 Disc Scale Height

Figure 3.4 shows the surface density rendered face-on views of discs evolved for 1000 binary orbits with various eccentricities (increasing left to right) and disc scale heights (increasing top to bottom). We see the cavity size increase with binary eccentricity, as described in Section 3.3.2, and decrease with increasing scale height. We also see the most eccentric cavities around the discs with smallest scale height.

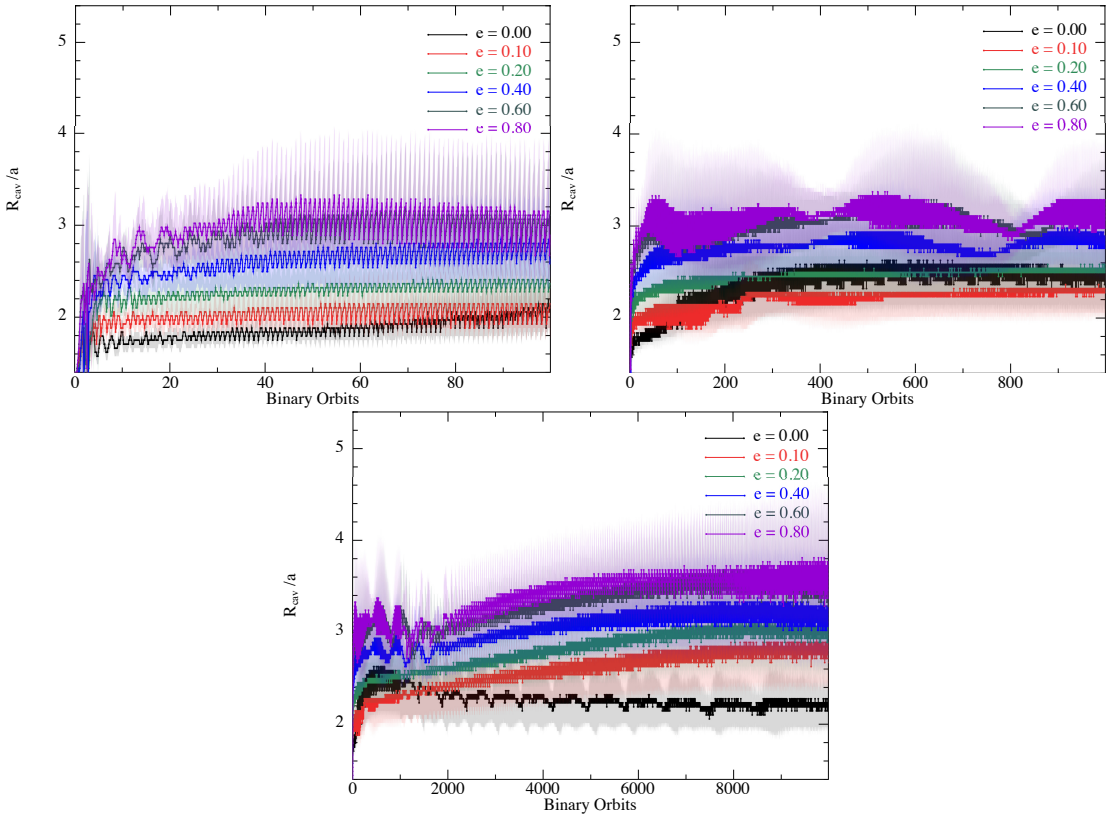

Figure 3.2: Evolution of cavity size over time for a coplanar disc with $(H/R)_{\rm in} = 0.05$ surrounding a binary with $q = 0.1$ over 100 binary orbits (top left panel), 1000 binary orbits (top right panel) and 10,000 binary orbits (bottom panel). The shaded region represents the error bars, as is the case for all subsequent plots in this paper.

Care must be taken, however, to evolve the discs for a significant fraction of the viscous time. The top panel of Fig. 3.5 shows the cavity size as a function of disc aspect ratio after only 100 binary orbits. From Equation 3.1, this corresponds to $\sim 3 \times 10^{-4} t_{\rm visc}$ for $(H/R)_{\rm in} = 0.01$ and $\sim 4.5 \times 10^{-2} t_{\rm visc}$ for $(H/R)_{\rm in} = 0.12$. At this early stage there is no dependence of cavity size on disc aspect ratio. The bottom panel of Fig. 3.5 is the same as the top panel, but after 1000 binary orbits.

Although 1000 binary orbits does not fully resolve the viscous time, it is already possible to see trends appearing. When $(H/R)_{\rm in} \lesssim 0.06$ the cavity size decreases for increasing scale height, then remains largely unchanged above this value. Furthermore, while the most viscous discs with $(H/R)_{\rm in} \gtrsim 0.06$ continue to evolve after 100 orbits the change in cavity size is minor, remaining within error bars. This suggests that taking the cavity size after 1000 orbits ($\gtrsim 0.1 t_{\rm visc}$ for these highly viscous cases) provides a reasonable estimation of the long-term cavity size.

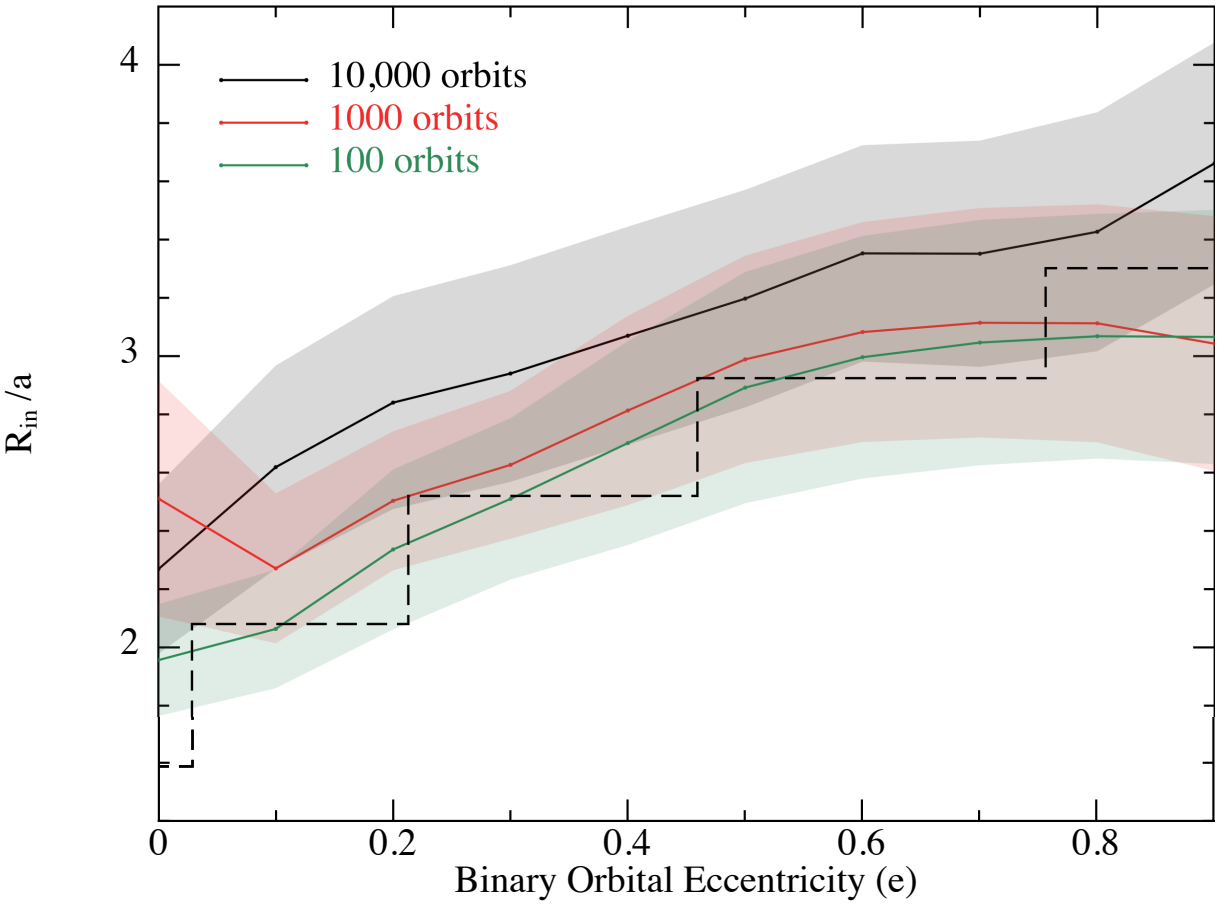

Figure 3.3: Cavity size as a function of binary orbital eccentricity for a coplanar disc with $(H/R)_{\rm in} = 0.05$ surrounding a binary with $q = 0.1$. Snapshots are taken after 100 (green line), 1000 (red line) and 10,000 (black line) binary orbits. Dashed line shows prediction from Miranda and Lai (2015).

While longer simulations would allow us to fully resolve the viscous time, these simulations become prohibitively expensive at low viscosity, requiring more than 10^5 binary orbits for $(H/R)_{\rm in} = 0.01$. It is also important to note that such long simulations would reach, or even exceed, the expected lifetime of protoplanetary discs, reducing their applicability to planet-forming discs at these late times.

3.3.4 Disc Inclination

Figure 3.6 shows circumbinary discs with $q = 0.1$, $(H/R)_{\rm in} = 0.05$ and $e = 0.8$ in both face-on and side-on views, rendered in surface density, with various initial inclinations and at various times. The critical inclination above which a disc of test particles tends towards a polar alignment is given by Equation 1.36. For $e = 0.8$ this corresponds to a critical inclination of 18.5°. Discs with an initial inclination lower than $i_{\rm crit}$ will tend towards a coplanar orbit. If the alignment time is shorter than the lifetime of the disc,

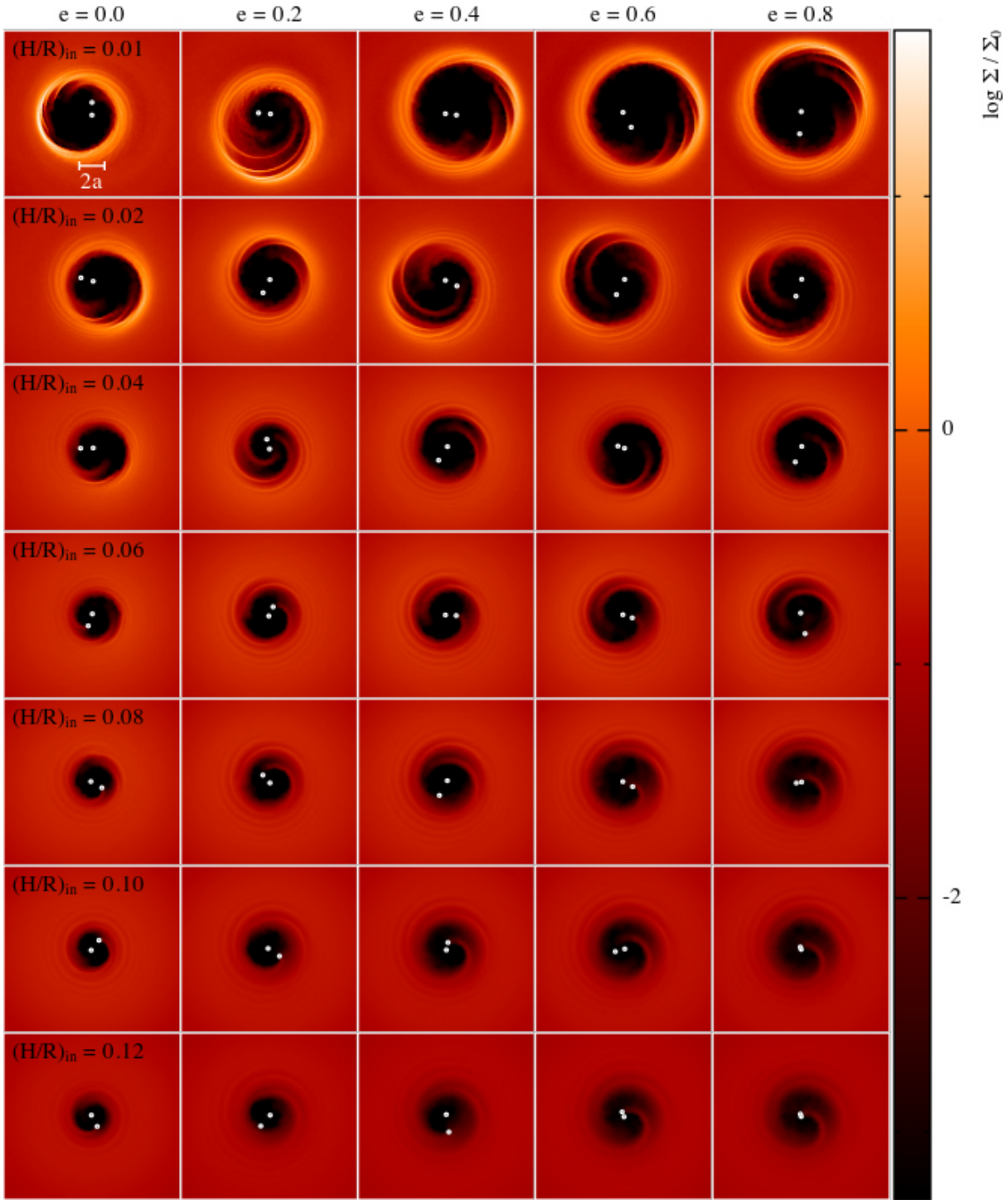

Figure 3.4: Surface density rendered face-on views of coplanar circumbinary discs surrounding a binary with $q = 0.1$ after 1000 binary orbits. Disc aspect ratio increases top to bottom, binary orbital eccentricity increases left to right. As seen in Figs. 3.3 and 3.5 cavity size increases with binary orbital eccentricity and decreases with disc aspect ratio.

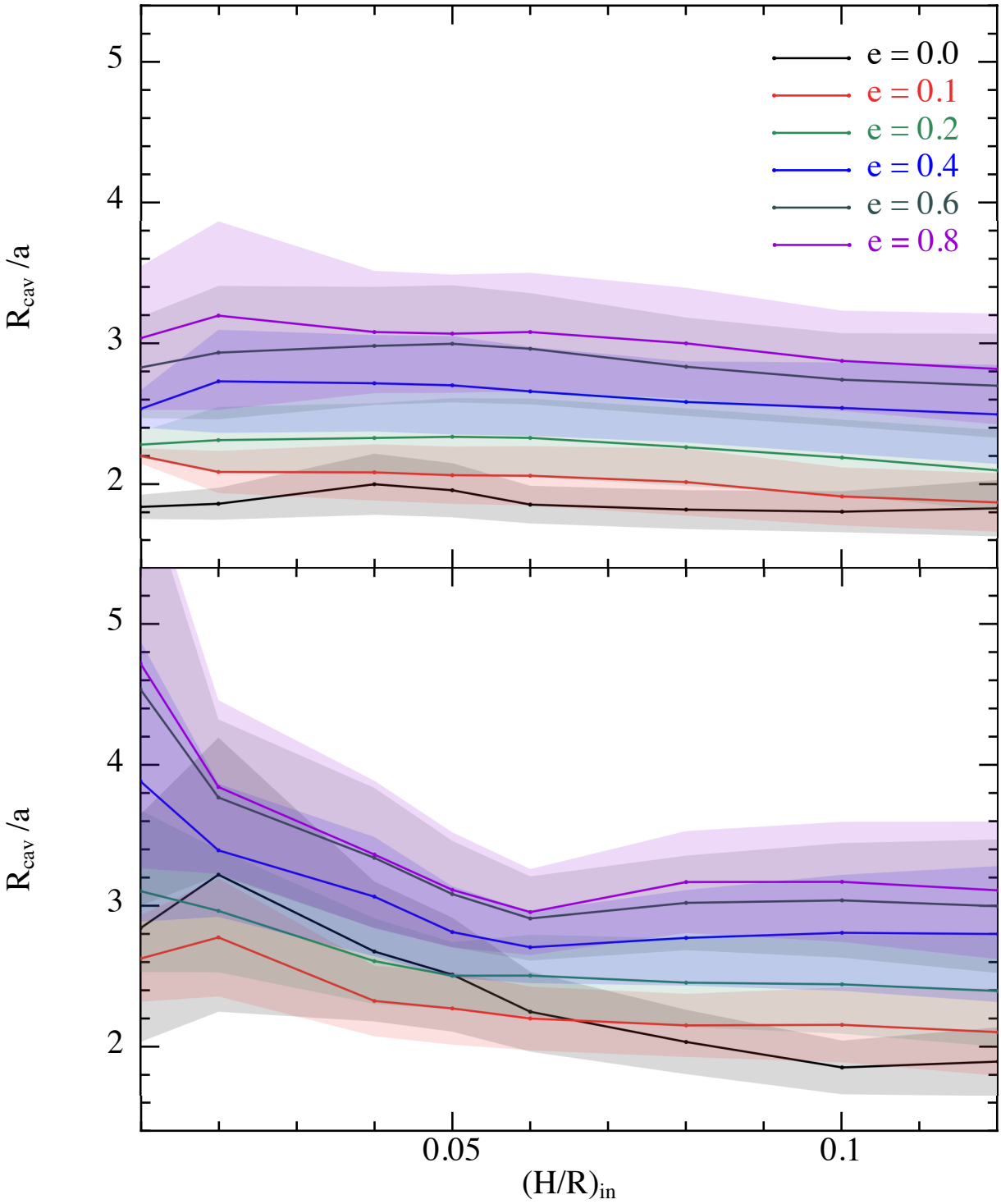

Figure 3.5: Cavity size as a function of disc aspect ratio for a coplanar disc surrounding a binary with mass ratio $q = 0.1$ after 100 binary orbits (top panel) and 1000 binary orbits (bottom panel).

this result implies that the final configurations will always be either polar or coplanar. In the case where the cavity is opened faster than the final alignment is reached, the disc will pass through a sequence of quasi-stationary configurations where the cavity size decreases (increases) as the disc progressively moves towards the polar (coplanar) configuration. In the case where the final alignment is reached before the cavity is opened, the cavity will be the same size as that of a disc initially in the final configuration. In Figure 3.6 we see that, consistent with Equation 1.36, both the $i = 22.5°$ and the $i = 45°$ discs tend towards a polar alignment, but their evolution looks very different due to the different alignment times.

For the $i = 45°$ disc the binary torque is strong enough to break the disc (c.f. Nixon et al., 2013; Facchini et al., 2013) and the inner disc quickly goes polar within hundreds of binary orbits; that is to say that the inner disc reaches a polar configuration on the same timescale as the cavity is opened. The outer disc aligns more slowly due to the weakened interaction with the binary.

For the $i = 22.5°$ disc the binary torque is not strong enough to break the disc and instead a warp forms in the inner regions of the disc which moves outwards over time. In this case the disc tends towards a polar alignment on the order of thousands of binary orbits while rigidly precessing. From the third row of Figure 3.6 we see that after 100 binary orbits the inner disc remains at a low inclination. Comparing the first two rows of Figure 3.6 we see the cavity opening process is similar to an initially coplanar disc due to the low inclination during the opening timescale.

Not shown in Figure 3.6 are discs with an initial inclination less than $i_{\rm crit}$ ($e \leq 0.4$ for $i = 22.5°$ and $e \leq 0.7$ for $i = 45°$). These discs tend towards a coplanar alignment and for $q = 0.1$ do so by warping.

The effect that the differing evolution has on the cavity size can be seen in Figure 3.7, which shows the cavity size of inclined discs after 1000 binary orbits. The two major factors in determining the cavity size at this time are whether the disc tends towards a coplanar or a polar alignment, and how quickly this alignment is reached.

Discs that tend towards a coplanar alignment open a cavity that is slightly smaller than that of an initially coplanar disc, due to the weaker binary torques in an inclined disc (c.f. ML15). The cavity then grows in time as the inclination is damped and the long term cavity size is expected to be that of an initially coplanar disc, though the realignment time is longer than the 1000 binary orbits we simulated.

As discussed earlier, discs that break and go polar reach a polar configuration within 100 binary orbits. This means that the cavity is opened when the disc is already polar, so the cavity size is equal to that of an initially polar disc.

Discs that warp and go polar do so slowly enough to open a cavity at an intermediate inclination before their inclination starts to increase. The binary torques get weaker as the disc gets more inclined, allowing the cavity to shrink as it is filled in due to viscous spreading. This process requires the disc to be evolved for a viscous time at its final polar configuration before the long-term cavity size can be recovered. After 1000 binary orbits, however, we recover an intermediate cavity size as the disc is still in the process of shrinking its cavity.

Simulations with $q = 0.5$ (not shown) produce similar results, with the exception that the binary torques are strong enough to break the disc, regardless of the binary eccentricity and disc inclination, leading to a faster alignment to either a coplanar or polar orbit. This leads to a cavity size that is equal to that of an initially polar disc for any disc that goes polar, while discs that tend towards a coplanar alignment again have a cavity size slightly smaller than that of an initially coplanar disc. For the coplanar discs breaking instead of warping allows for faster realignment for the coplanar discs, especially at low eccentricity. This leads to a cavity size that is closer to that of an initially coplanar disc.

3.3.5 Binary Mass Ratio

Figure 3.8 shows surface density rendered face-on views of circumbinary discs with $(H/R)_{\rm in} = 0.05$ after 1000 binary orbits for various eccentricities and binary mass ratios. Around circular binaries, strong horseshoe shaped over-densities are seen at the cavity edge, becoming weaker as the companion decreases in mass and disappearing at $q = 0.001$. Faint horseshoes can also be seen around highly eccentric binaries, again becoming weaker with smaller companions.

Figure 3.9 shows the cavity size as a function of eccentricity for coplanar discs with $(H/R)_{\rm in} = 0.05$ around binaries with four different mass ratios ($q = 0.01, 0.1, 0.3$ and 0.5) after 1000 binary orbits. When $q \geq 0.1$ we see the turnover discussed in §3.3.2. Consistent with Ragusa et al. (2017), we find that the more massive companions carve the largest cavities. There is an exception to this at low eccentricity ($e \leq 0.2$) where the maximum cavity size is seen around binaries with $q = 0.3$, though we caution here that our resolution in mass ratio is coarse.

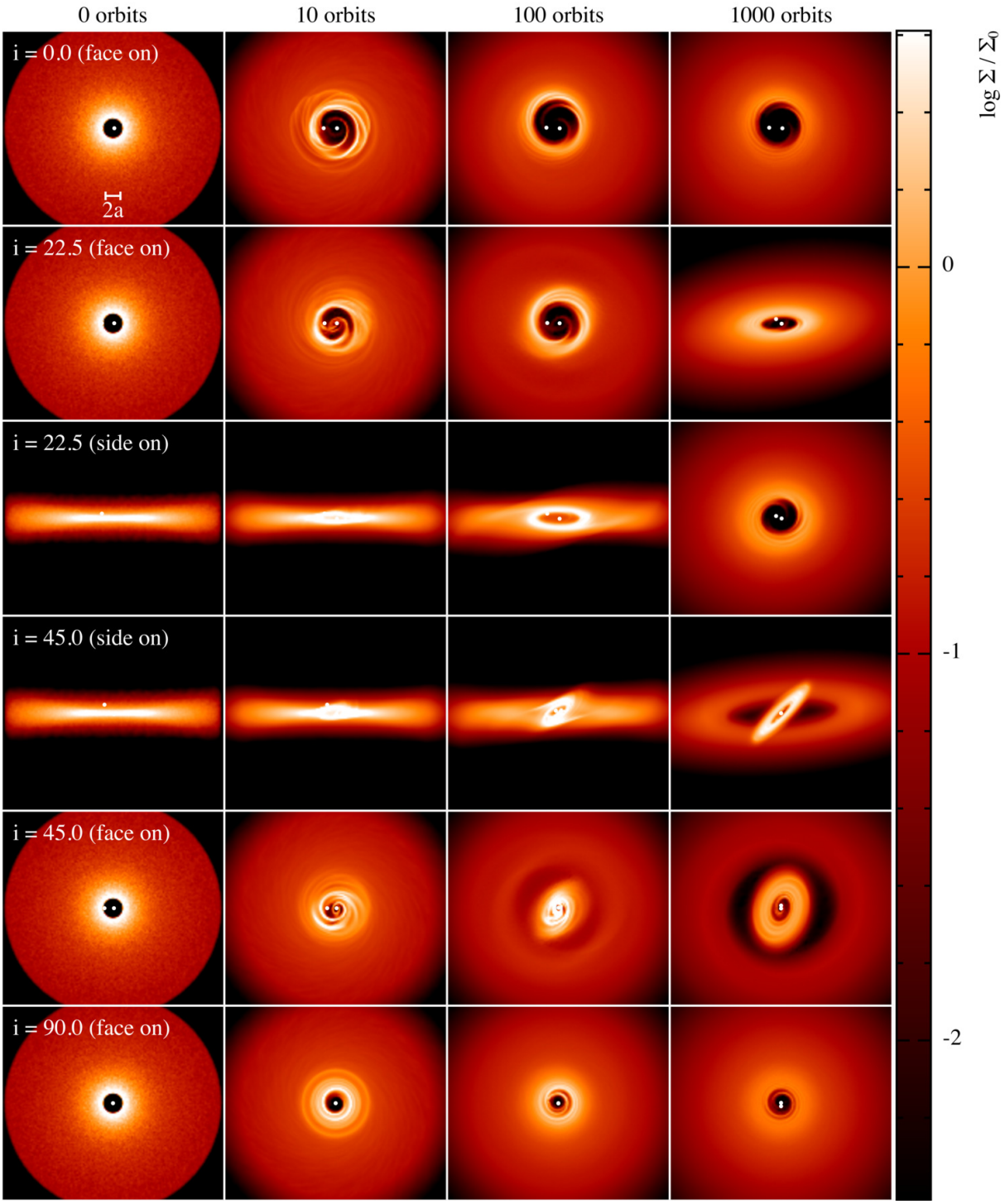

Figure 3.6: Surface density rendered views of the evolution of inclined circumbinary discs with $(H/R)_{\rm in} = 0.05$ surrounding a binary with $q = 0.1$ and $e = 0.8$. Time increases from left to right and inclination increases from top to bottom. Coplanar and polar discs are shown only in face-on views, while $i = 22.5°$ and $i = 45°$ are shown in both face-on and side-on views.

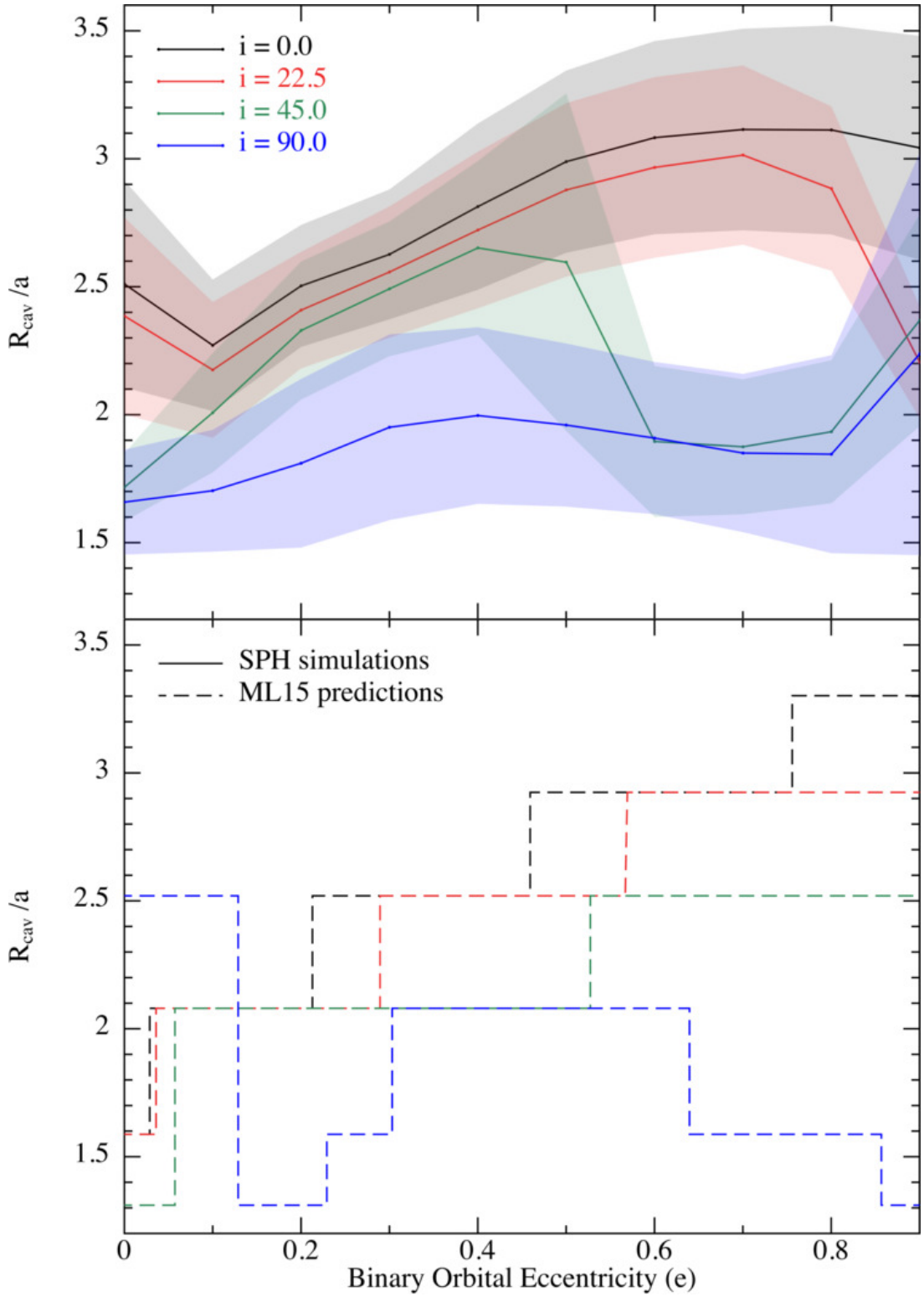

Figure 3.7: Cavity size as a function of binary orbital eccentricity for a disc with $(H/R)_{\rm in} = 0.05$ surrounding a binary with $q = 0.1$ after 1000 binary orbits. Different line colours depict discs with different initial inclinations to the binary orbital plane. The solid lines (top panel) represent the results from our SPH simulations while the dashed lines (bottom panel) represent the analytical estimates from ML15.

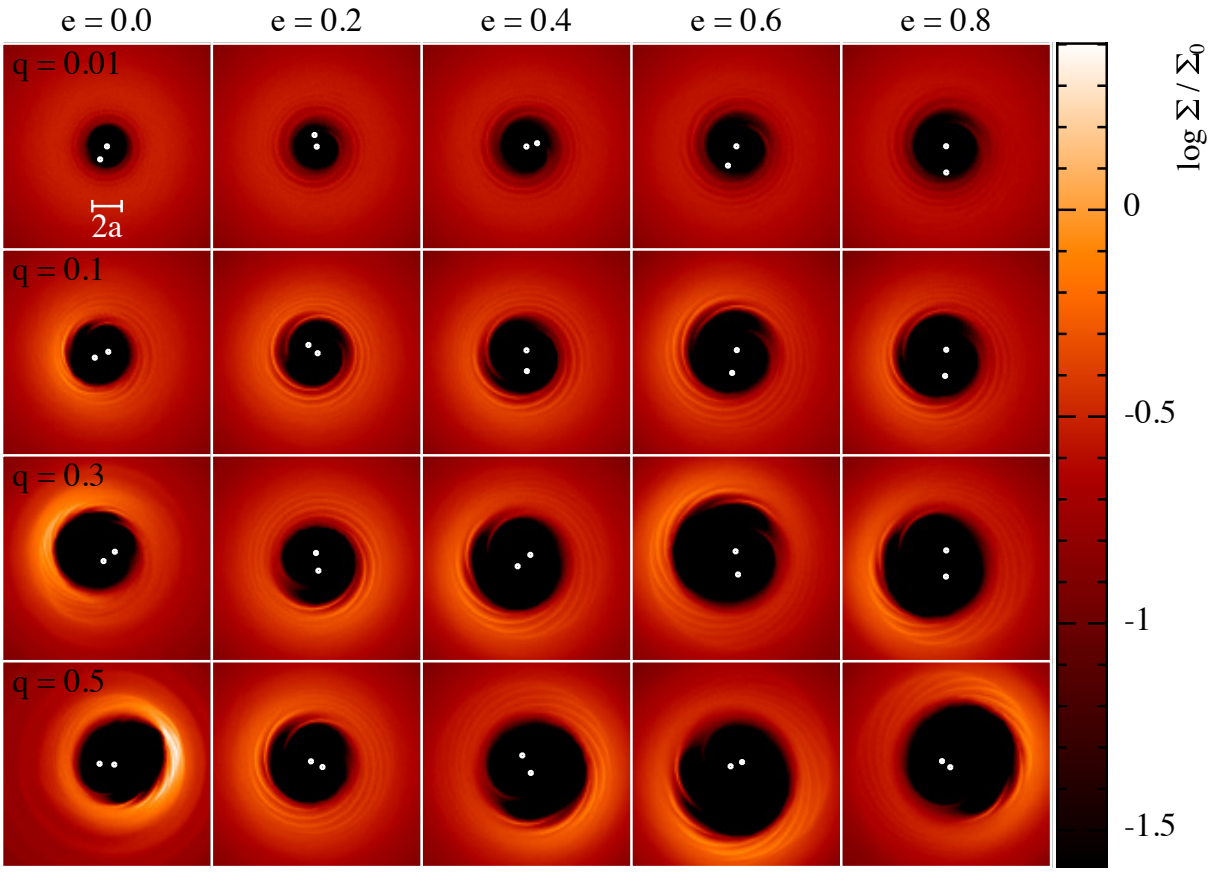

Figure 3.8: Surface density rendered face-on views of coplanar circumbinary discs with $(H/R)_{\rm in} = 0.05$ surrounding a binary with varying mass ratio and eccentricity after 1000 binary orbits. Binary mass ratio increases top to bottom, binary orbital eccentricity increases left to right.

3.3.6 Gas Depletion

Figure 3.10 shows the azimuthally averaged surface density as a function of radius for coplanar discs around circular binaries with $q = 0.1$ and various disc aspect ratios, allowing us to see how depleted the cavity is. One common method to characterise the depletion is to model the surface density of the disc as a power law with an exponential taper (Lynden-Bell and Pringle, 1974) and model the cavity by scaling down the surface density by a constant depletion factor, giving (Andrews et al., 2011; Perez et al., 2015)

$$\Sigma(r) = \delta_{\rm gap}\Sigma_0 \left(\frac{r}{R_0}\right)^{-p} \exp\left[\left(-\frac{r}{R_0}\right)^{2-p}\right], \tag{3.2}$$

where Σ_0 is the surface density at the characteristic radius R_0 and $\delta_{\rm gap}$ is the depletion factor, with $\delta_{\rm gap} = 1$ outside the cavity and $\delta_{\rm gap} < 1$ inside the cavity. This characterisation is impossible for us since the surface density inside the cavity is below what we are able to resolve, so instead we take the depletion as $\delta_{\rm gap} = \Sigma_{\rm max}/\Sigma_{\rm min}$, where $\Sigma_{\rm max}$ and $\Sigma_{\rm min}$

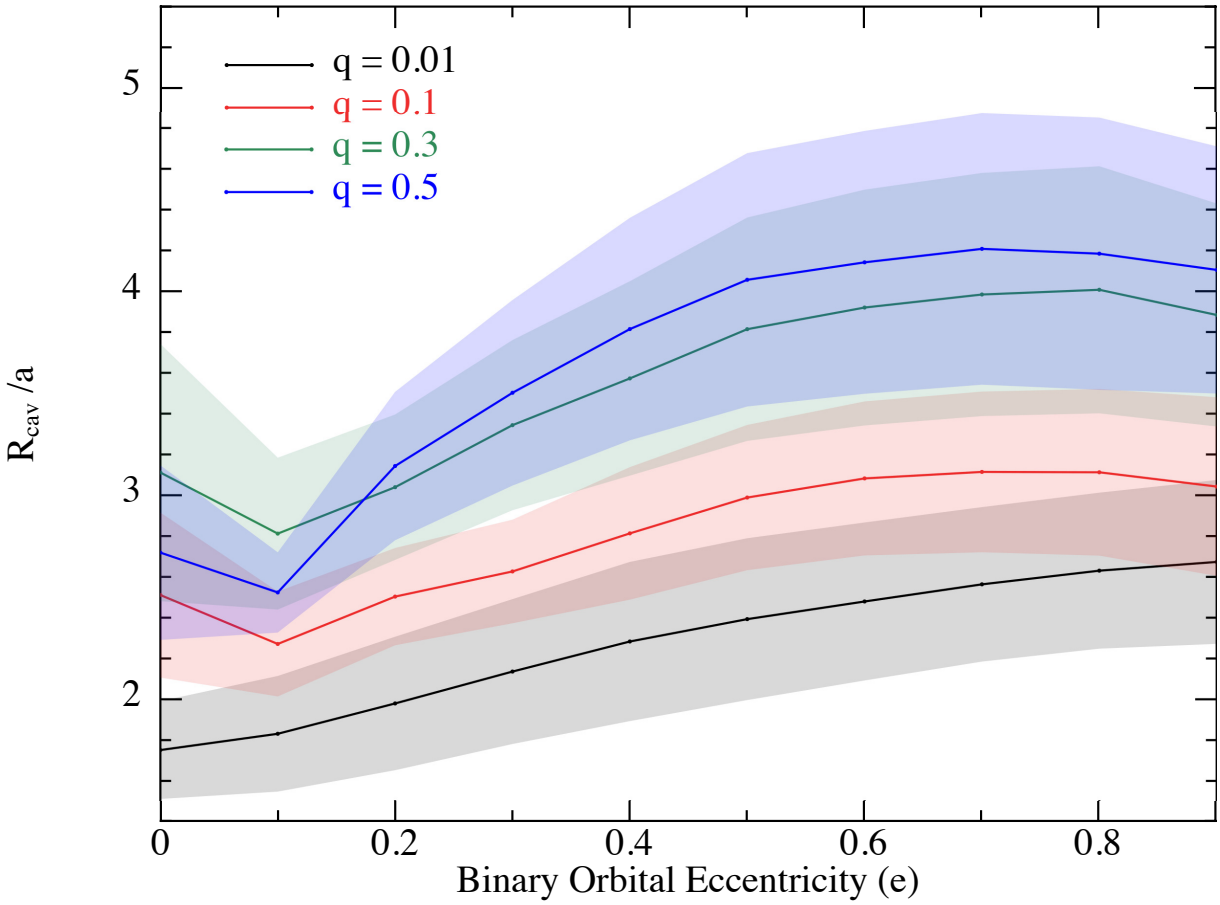

Figure 3.9: Cavity size as a function of binary orbital eccentricity for a coplanar disc with $(H/R)_{\rm in} = 0.05$ after 1000 binary orbits. Different lines depict binaries with different mass ratios.

and the maximum and minimum values of surface density that we recover, respectively.

We find that in all cases the depletion is 2–3 orders of magnitude, decreasing as the disc becomes more viscous. However, in every case our $\Sigma_{\rm min}$ is at our resolution limit, so these values can only be treated as a minimum depletion in the cavity. Furthermore, the more viscous discs have a smaller $\delta_{\rm gap}$ due to a smaller $\Sigma_{\rm max}$, which does not necessarily imply a less depleted cavity.

3.3.7 Resolution Study

We performed a resolution study by comparing the discs in Section 3.3.2 with discs of 300 thousand and 3 million particles, keeping all physical properties the same. For the resolution study we only considered binary eccentricities from $e = 0.1$ to $e = 0.9$ with a step size of 0.2. Figure 3.11 shows the cavity size as a function of binary eccentricity for these simulations. The results only converge for simulations with at least 1 million

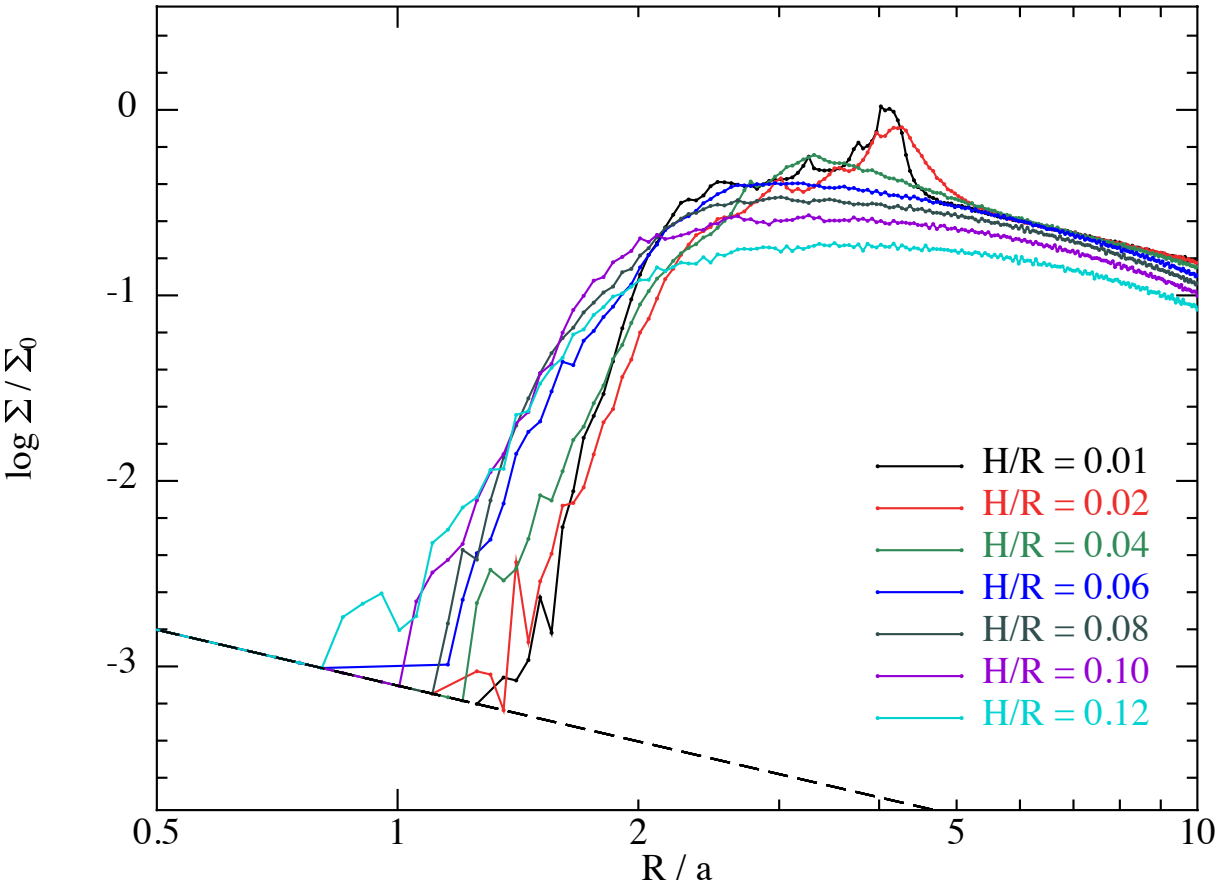

Figure 3.10: Azimuthally averaged surface density as a function of radius in the disc, in units of binary semi-major axis, on a log-log scale. All discs are coplanar with a circular binary of $q = 0.1$, with each line representing a different disc aspect ratio. The dashed line is the lowest possible Σ we can resolve.

particles, while with only 300 thousand particles the cavity size is underestimated. This underestimated cavity size is due to the scale height not being resolved, leading to increased numerical viscosity. At 1 million particles the scale height is resolved, so any further increase in resolution gives no improvement in the cavity size estimate.

3.4 Discussion

When comparing to previous works we found results consistent with the main conclusions from AL94 and ML15, namely that cavity size increases with increasing binary eccentricity and decreasing disc viscosity.

ML15 also found that for discs with $i \leq 45°$ cavity size decreases with disc inclination (bottom panel of Fig. 3.7). However theirs was an analytical study, comparing the strengths of the viscous and binary torques for static discs and not taking into account

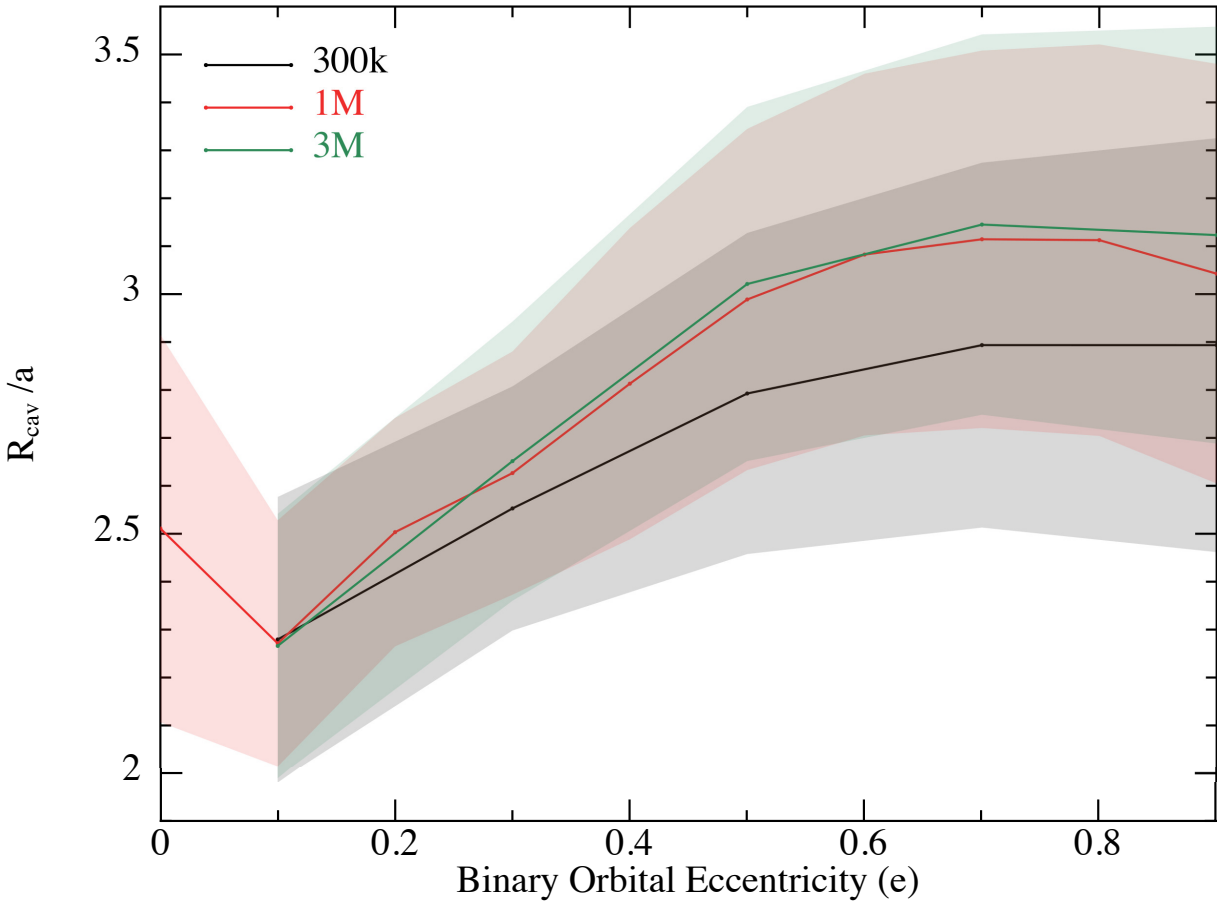

Figure 3.11: Cavity size as a function of binary orbital eccentricity for a coplanar disc with $(H/R)_{\rm in} = 0.05$ and $q = 0.01$. Different lines represent different number of SPH particles.

changes in inclination over time. For discs which tend towards a coplanar orbit we also find that cavity size decreases with initial inclination, however for discs which tend towards a polar orbit this is no longer the case (see Section 3.3.4).

We find that the angle above which a disc will go polar matches previous predictions and simulations (Aly et al., 2015, 2018; Martin and Lubow, 2018; Cuello and Giuppone, 2019). We also see disc breaking at high binary mass ratio and high binary eccentricity. This is consistent with the results from Nixon et al. (2013) and was also recently seen by Facchini et al. (2018).

Thun et al. (2017) found cavities that extend to upwards of seven times the binary semi-major axis for coplanar discs with $(H/R)_{\rm in} = 0.05$ around highly eccentric binaries. They also found a turnover in cavity size as a function of binary eccentricity that persists to 16,000 binary orbits, with the smallest cavities being opened by binaries with $e = 0.18$. We also found a turnover (see Fig. 3.3), however ours was at $e = 0.1$ and only appears at

intermediate stages of the disc evolution, disappearing after several thousands of binary orbits. These differences are likely due to the different codes used in our analyses. The use of 2D grid-based codes requires careful consideration of the inner boundary when working with a polar grid (see Section 4.1 of Thun et al., 2017). Indeed, recent works have found that choosing an open boundary with $R_{\rm in} > a$, as in Thun et al. (2017), can lead to an artificially large cavity (Mutter et al., 2017; Pierens et al., 2020).

Ragusa et al. (2017) find that larger companions carve larger cavities, though they only consider binaries with $q \leq 0.2$. As discussed in Section 3.3.5 we found this to be the case for binaries with $q \leq 0.3$. Equal mass binaries continue this trend when highly eccentric, but when $e \lessapprox 0.2$ equal mass binaries carve smaller cavities than those with $q = 0.3$. The reason for this is unclear.

In Section 3.3.3 we compare discs with different scale heights at the same number of orbits, corresponding to a different fraction of the viscous time for each disc. It is natural to consider whether comparing the discs at the same viscous time shows the same behaviour. To this end Fig. 3.12 shows the evolution of the cavity size as a fraction of the viscous time. After $\sim 10\%$ of a viscous time the cavity size is seen to increase with decreasing viscosity. This is the same behaviour as seen in the bottom panel of Fig. 3.5. That is, our conclusions are independent of whether we use time in orbits or time in viscous times so long as the system has been evolved for a significant fraction of the viscous time. Figure 3.12 suggests that even low eccentricity ($e = 0.1$) binaries in discs with $(H/R)_{\rm in} \lesssim 0.02$ may eventually produce cavities with radii $\gtrsim$ 3–4 times the semi-major axis. However, evolving such low viscosity discs for a significant fraction of the viscous time is prohibitively expensive. The results are also irrelevant for protoplanetary discs, since in these cases the viscous time starts to exceed the disc lifetime.

When comparing this work to observations, one should keep in mind the following:

We only modelled the gas. ALMA continuum observations probe the mm-sized dust in the disc midplane. While comparisons to ALMA observation of gas lines can be made with gas-only simulations, comparisons to the continuum observations would require full gas and dust simulations. We would expect to see a larger cavity in the dust than in the gas (c.f. van der Marel et al., 2018).

We prescribed a fixed temperature profile. Since we did not account for radiation from the central stars we have an axisymmetric temperature profile, rather than one which oscillates during the orbit of the stars (Nagel et al., 2010; Bodman and Quillen, 2015). This

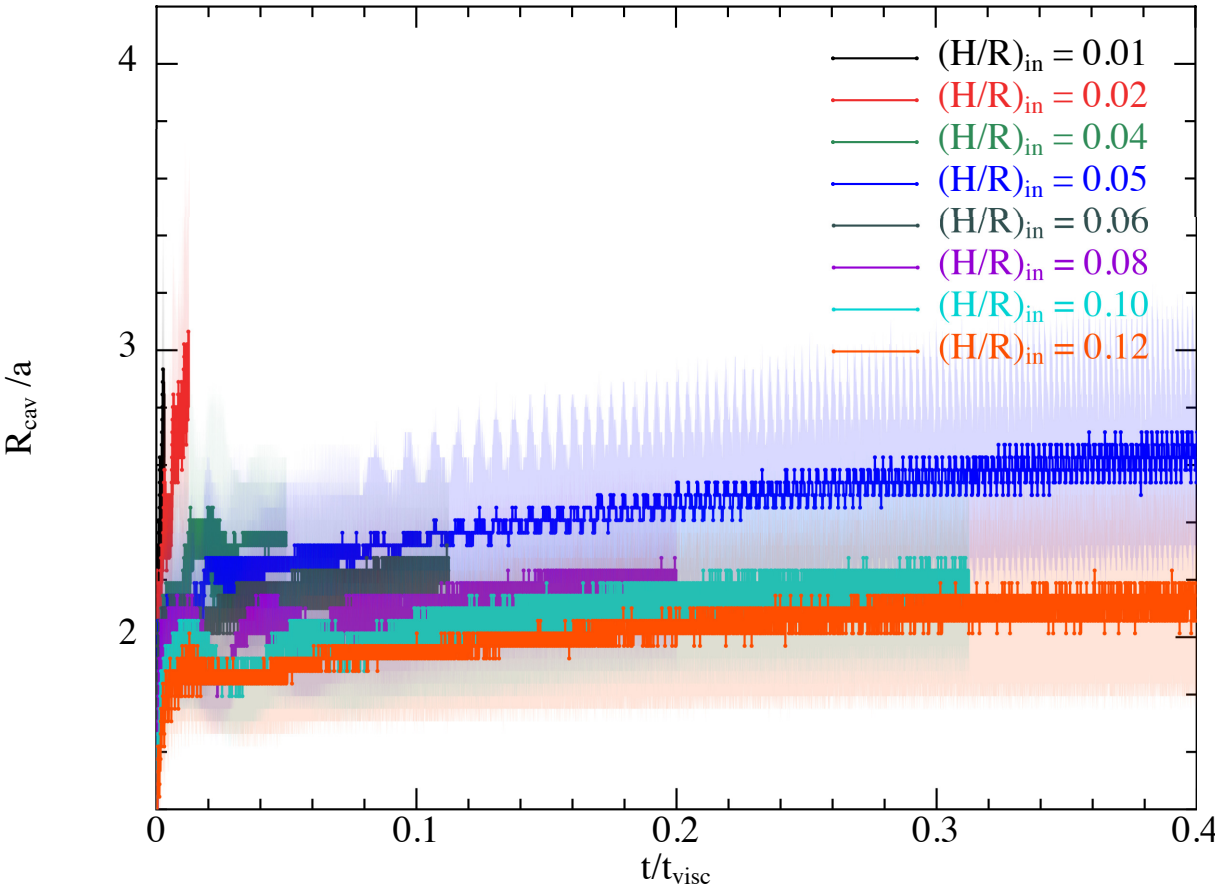

Figure 3.12: Cavity size as a function of fraction of viscous time for coplanar discs surrounding a binary with $e = 0.1$.

azimuthal temperature variation would lead to local fluctuations in viscosity. Any effects from these local fluctuations would be minor, since they oscillate on the orbital time, while the cavity size is set on the viscous time. The temperature difference caused by shadows from a circumstellar disc (e.g. HD 142527, Casassus et al., 2015b; Avenhaus et al., 2017) would be persistent and could drive an eccentric cavity due to local regions of low viscosity. Furthermore, once a cavity becomes eccentric it would have a non-axisymmetric temperature profile, with the material at periastron being warmer than that at apoastron. This could drive larger eccentricity in the cavity, though a simulation that combines dynamics and radiative transfer would be needed to investigate this effect (see Nealon et al., 2020). Recently, Miranda and Rafikov (2019) showed that using a locally isothermal equation of state — instead of solving the energy equation — may overestimate the contrast of gaps in discs. Whether or not this would change our conclusions regarding the cavity size would be worthy of investigation.

We model viscosity using an α-disc with $\alpha = 5 \times 10^{-3}$, though the true value of α in protoplanetary discs remains uncertain. Flaherty et al. (2020) argue that most obser-

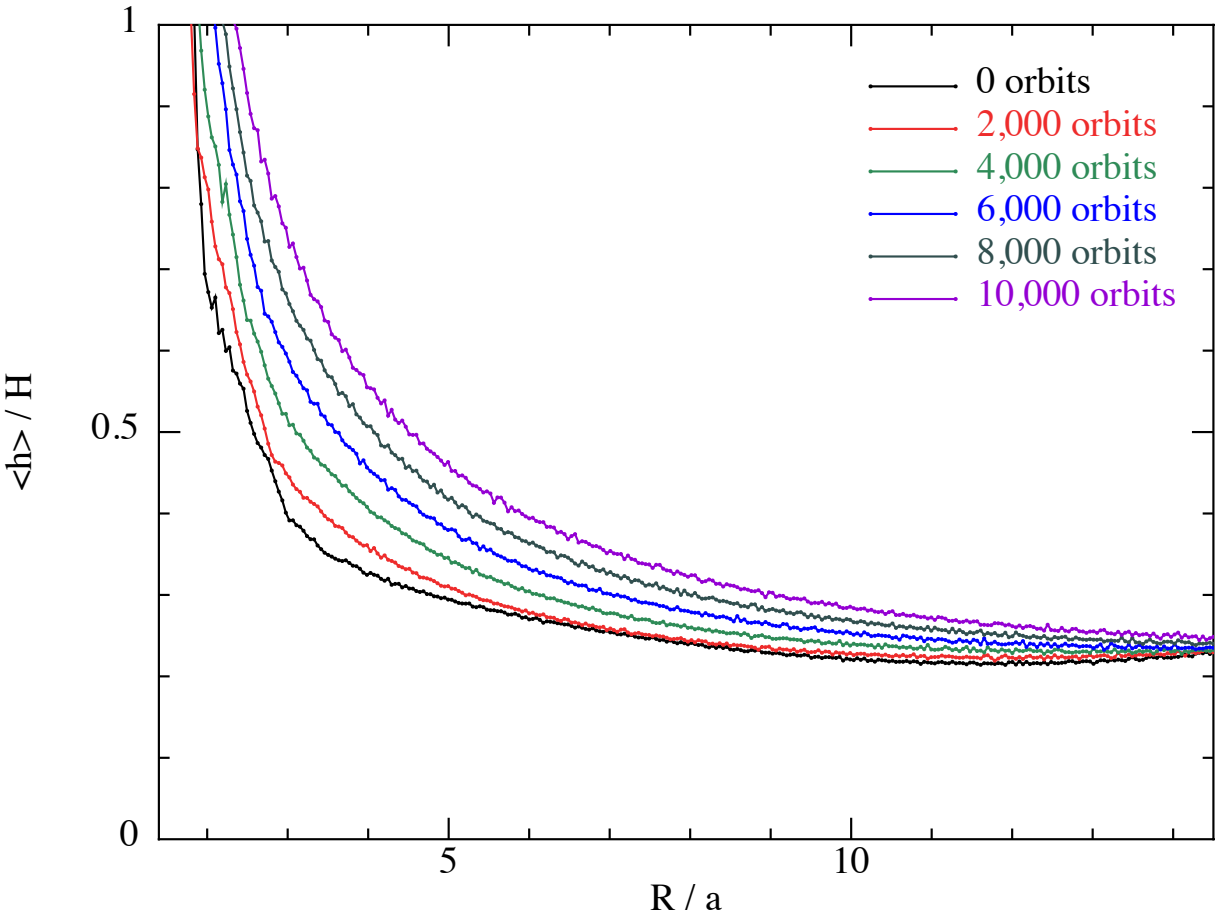

Figure 3.13: Smoothing length, in units of disc scale height, as a function of radius in the disc, in units of binary semi-major axis for a coplanar disc with $(H/R)_{\rm in} = 0.05$ around a circular binary with $q = 0.1$. Lines are shown at 20,000 binary orbit intervals.

vational evidence points towards $\alpha \sim 10^{-4} - 10^{-3}$ (see also Mulders and Dominik, 2012; Boneberg et al., 2016). They do, however, provide examples of a small number of systems with $\alpha \sim 10^{-2}$, suggesting that higher values of α, while uncommon, are possible. Contrasting this, Papaloizou (2005) found that the resonant coupling between inertial-gravity waves and a free $m = 1$ global mode causes an instability which leads to a turbulence with an effective $\alpha \sim 10^{-3}$. Pierens et al. (2020) found that the presence of a binary strengthens this instability, leading to an effective $\alpha \sim 5 \times 10^{-3}$. It is also important to note that setting a low $\alpha_{\rm AV}$ in SPH leads to a higher than expected dissipation (Meru and Bate, 2012). This effect is reduced with higher resolution simulations, however simulating an α of 10^{-4} would require an unfeasibly large number of particles. Since a higher viscosity leads to a smaller cavity, our results would underestimate the cavity size in discs with low α and an investigation into discs with low α would be required for comparisons with observations of discs with such low viscosity.

In section 3.3.4 we claim that all discs will tend towards either a coplanar or a polar orbit in the long term. While this is valid for low mass discs, Martin and Lubow (2019) found that discs with a significantly high mass can reach an equilibrium at an intermediate inclination. As such, a study investigating the effects of disc mass would be required to understand how the cavity evolves in these high mass discs.

Viscous disc spreading reduces the surface density of the disc over time as material is accreted onto the central stars. This also reduces the number density of SPH particles in the disc, lowering the resolution and increasing the smoothing length over time, as shown in Fig. 3.13. Due to our prescription of disc viscosity (Section 3.2.2), this leads to an increase in the viscosity over time. The effect is more pronounced in the inner disc, where the smoothing length increases by up to a factor of 4 after 10,000 binary orbits. An increased viscosity near the cavity edge may lead to an underestimated cavity size in our simulations, though since this effect is present in all discs we expect the trends to remain unaffected.

In our simulations we found that cavities can be up to five times the semi-major axis of the binary orbit, meaning that binary companions can be close to the primary while still carving a large cavity, making the companion difficult to resolve. Indeed, many discs previously classified as transitional, such as CoKu Tau/4 (Ireland and Kraus, 2008) and HD 142527 (Biller et al., 2012), have only been reclassified as circumbinary in the last 15 years, despite hosting stellar or sub-stellar mass companions. This problem is further exacerbated for highly eccentric discs, since they tend towards a polar inclination (Aly et al., 2015, 2018; Martin and Lubow, 2018), Discs on a retrograde orbit are also more likely to become polar (Cuello and Giuppone, 2019) For any polar disc (or indeed, any highly-inclined disc) in a nearly face-on configuration, the small projected separation of the binary would make it extremely difficult to resolve. Since highly-inclined discs are not uncommon for binaries with long periods (Czekala et al., 2019), many discs currently classified as transitional may yet turn out to be hiding binary companions.

3.5 Conclusions

We have performed a numerical examination of cavity opening by a binary embedded in an accretion disc, revisiting and expanding the original numerical and analytic study by AL94 and the recent analytic extension to inclined discs by ML15. We considered the effects of binary eccentricity, inclination, mass ratio, disc vertical scale height and binary mass ratio. Our conclusions are:

1. There exists two timescales for the cavity opening process. The cavity is quickly opened on a dynamical time, within a few tens of orbits, while the long term size of the cavity is set on the viscous time, after tens of thousands of orbits.

2. Binaries carve cavities in circumbinary discs at a radius 2–5 times the semi-major axis, with a cavity size that depends most strongly on binary eccentricity and disc viscosity, as predicted by AL94 and ML15.

3. When considering inclined discs there exists three regimes. Discs which evolve towards a coplanar orbit have a cavity size slightly smaller than an initially coplanar disc, decreasing in size as initial inclination increases. Discs which evolve towards a polar orbit have a cavity size which depends on their evolution, i.e. whether they break or warp. Discs which break have a small cavity equal in size to those of an initially polar disc, while discs that warp quickly open a large cavity which is then filled in on the viscous timescale, resulting in an intermediate sized cavity which shrinks on a viscous timescale to the size of a cavity in an initially polar disc.

4. Cavity size is an increasing function of binary mass ratio for all but the largest companions on low eccentricity orbits.

5. All of our binaries (with $q \geq 0.01$) produced a gas depletion inside the cavity of at least 2 orders of magnitude in surface density.

There are a number of ways this work could be expanded upon. Simulating discs with both gas and dust would allow for an investigation into cavity size of the dust phase of the disc. Simulating discs with a lower α would allow for a deeper understanding of the effects of viscosity on the cavity size and could help to constrain the α in observed discs. Simulating discs with a more complex temperature prescription could allow for investigations into the effects of a non-axisymmetric temperature profile on the cavity size and eccentricity. Creating synthesised images of the discs simulated here would allow for an investigation into the observational signatures of a binary companion. This investigation is presented in Chapter 4.

Chapter 4

Observational Appearance of Circumbinary Discs

4.1 Introduction

As discussed in Section 1.5 there exists many discs showing properties typically associated with that of a circumbinary disc but with no known stellar companion. Thus, if we wish to infer the presence of a second star in these systems it is crucial to understand the observable signatures it imprints on the disc. In this chapter we use the radiative transfer code `MCFOST` (see Section 2.3) to compute synthetic moment 0, 1, and 2 maps, as well as synthetic channel maps, of the simulated discs in Chapter 3. To irradiate the disc we take the central stars as isotropic sources, adopting the 3Myr isochrones from Siess et al. (2000) to determine the stellar parameters. The primary has $T_{\rm eff} = 4250$ K and a luminosity $L = 0.87$ $L_\odot$, with the secondary having the same properties in the $q = 0.5$ simulations. The secondary has $T_{\rm eff} = 3650$ K and $L = 0.25$ $L_\odot$ when $q = 0.3$, $T_{\rm eff} = 2980$ K and $L = 0.07$ $L_\odot$ when $q = 0.1$, and $T_{\rm eff} = 2100$ K and $L = 7.8 \times 10^{-4}$ $L_\odot$ when $q = 0.01$. We then examine synthetic images to better understand how the presence a binary companion can be inferred from observations and we develop a metric to quantify the effect the binary has on the disc. The work presented in this chapter will be published in a paper currently in preparation.

4.2 Definition of Asymmetry Metric

We define two metrics to measure the asymmetry in the disc. The first metric, which for now we will call the double channel metric, measures the asymmetry in two opposite velocity CO channels. The second metric, which for now we will call the single channel metric, measures the asymmetry in a single CO channel. For the double channel metric the

positive branch is flipped across the y-axis and subtracted from the negative branch (note that the choice of which branch to flip is arbitrary) while for the single channel metric a single channel is flipped across the x-axis and subtracted from itself. The resulting images are show in Figure 4.1). We then define the asymmetry in the channel, for both cases, as the L2 norm of the flux in the subtracted image, normalised to the integrated flux in the channel (taking only the positive branch for the double channel metric). This is given by:

$$\aleph_c = \frac{\sqrt{\sum_{i,j} \Delta F_{ij}^2}}{F}, \tag{4.1}$$

where $\aleph_c$ is the asymmetry in channel c, ΔF_{ij} is the flux on pixel (i, j) in the subtracted image and F is the integrated flux. Normalising to the integrated flux gives a non-dimensional $\aleph_c$ that is insensitive to field of view and signal strength.

Figure 4.2 compares the value of $\aleph_c$ for the double channel and single channel metrics. The discs shown are the fiducial set from Chapter 3; that is, binary mass ratio $q = 0.1$, aspect ratio $H/R_{\rm in} = 0.05$, coplanar disc ($i = 0°$), and a number of binary eccentricities are shown. Both metrics appear to have a local maximum $\aleph_c$ near the 0 velocity channel and have an increasing $\aleph_c$ at high velocity channels. While Figure 4.2 only compares discs with differing binary eccentricity this similar behaviour between the two metrics is true in general, implying that we need only consider one metric going forward. In future sections we will consider only the double channel metric due to it being less noisy to channel selection. Since $\aleph_c$ has only small variations in each channel we are free to take the average over all visible channels to get $\aleph$, the total disc asymmetry. This allows us to quantify the disc as a whole and has the advantage of allowing us to compare two discs even if part of one disc is obscured by removing the obscured channels from the average.

In Figure 4.3 we compare $\aleph_c$ at different binary orbital phase for a the fiducial disc from Chapter 3 after 1000 binary orbits. We see that the asymmetry in the disc is independent of the binary orbital phase, thus when comparing discs we are free to consider them at any point during their orbit.

4.3 Moment Maps

Figure 4.4 shows moment 0, moment 1, and moment 2 maps of our fiducial disc at three different angles on the sky. As mentioned in Section 2.3.4 the moment 0 maps largely trace the gas density, with an important caveat. The resolution in the moment 0 map is the beam size, which is much larger than the resolution in the SPH simulations, the

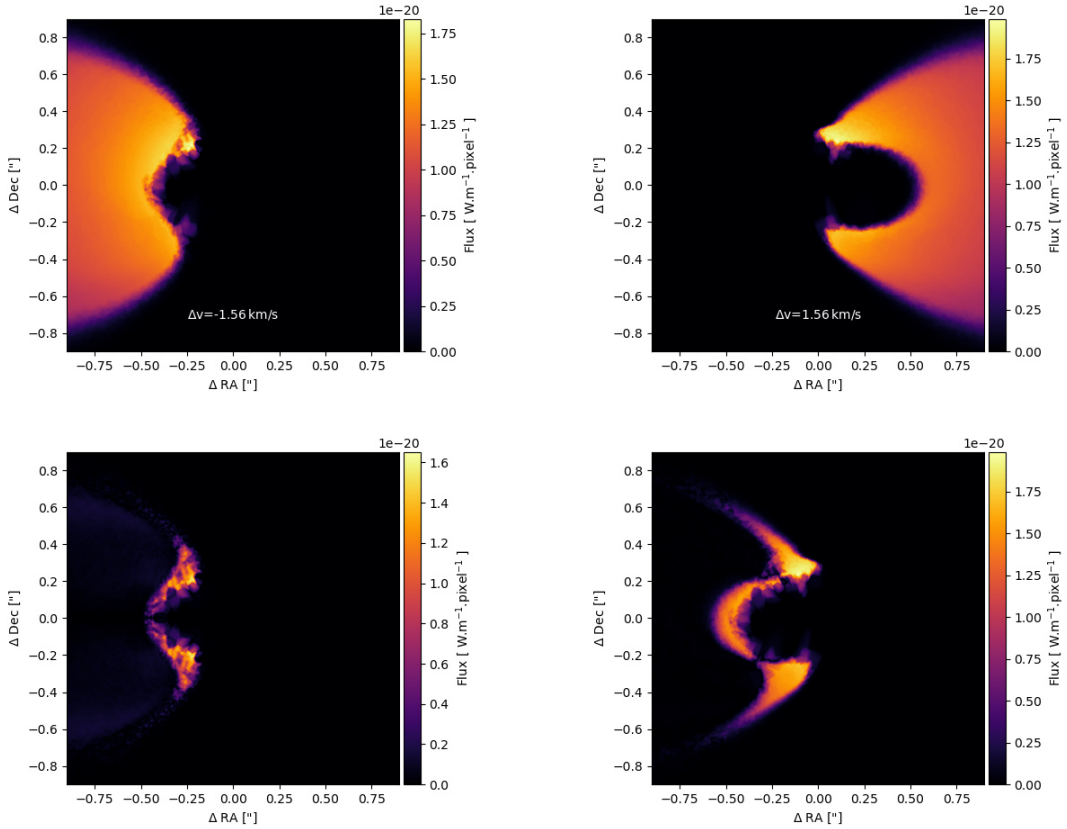

Figure 4.1: Top row: 2 channel maps with opposite velocities. Bottom left: Double channel metric, the positive branch has been flipped horizontally and subtracted from the negative branch. Bottom right: Single channel metric, the negative branch has been flipped vertically and subtracted from itself. Note that in the bottom row the absolute value of the difference has been plotted to give $F_{\rm min} = 0$.

smoothing length. This means that fine details will not be recovered in these synthetic observations. We do not analyse the moment 0 maps in this work, however they are always computed as they are a necessary step in calculating further moment maps.

The signal in the moment 1 map is dominated by noise when the disc is face-on to the observer (middle left panel). This is due to the fact that the gas orbits in the plane of the disc with little vertical motion. However, when the disc is titled on the plane of the sky (22.5° in the centre panel and 45° in the middle right panel), we recover a signal. Examining the $v = 0$ iso-velocity line, that is the line of the material which has no line of sight velocity, we see a twist inside the cavity. To investigate this peculiar shape we consider the effects of the radial and azimuthal components of the gas velocity in the plane of disc. We remove the radial component of the velocity by setting the $v_r = 0$ in the final output of the fiducial `PHANTOM` simulation before recomputing the moment 1 map with `MCFOST`.

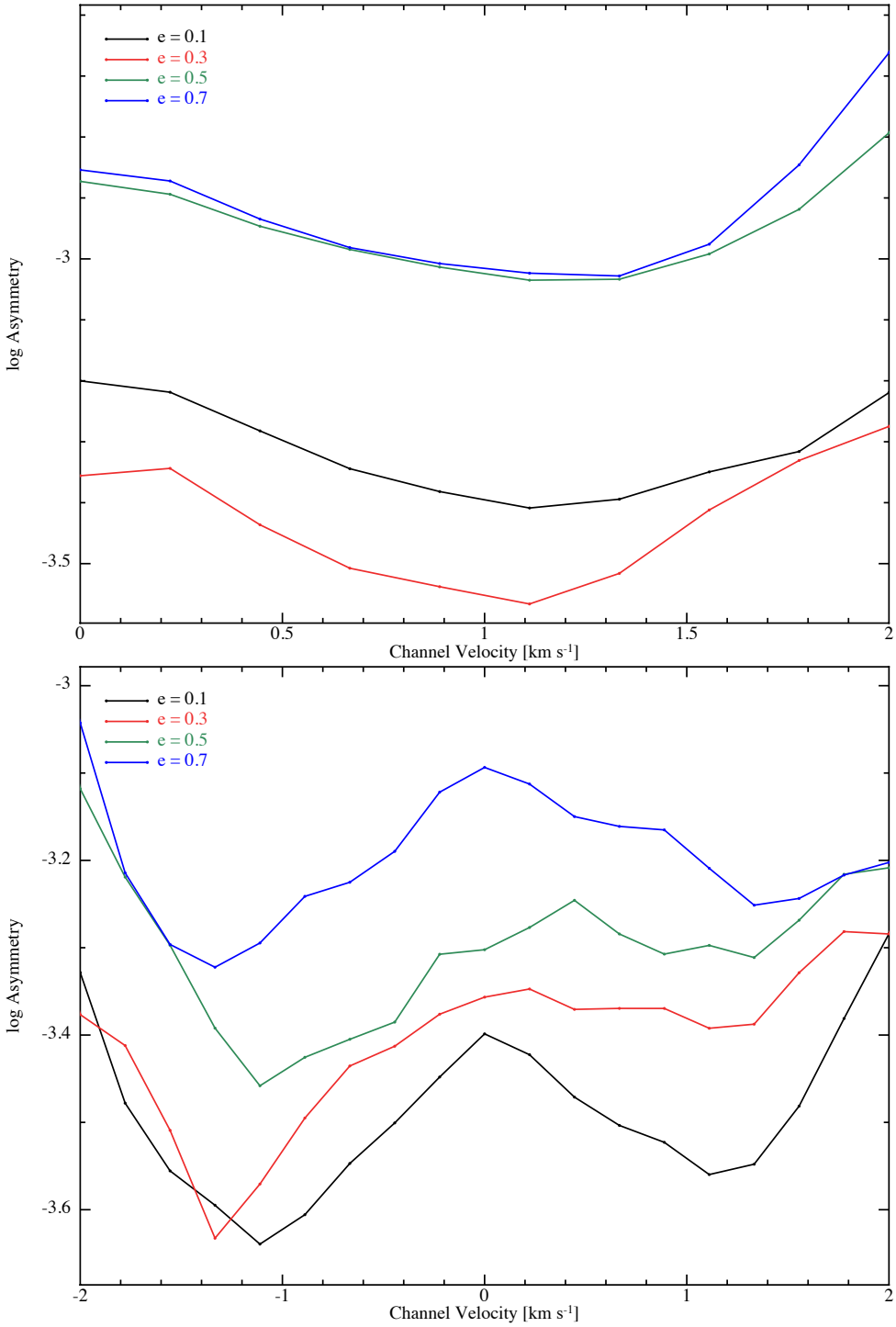

Figure 4.2: Asymmetry metric $\aleph_c$ as a function of channel velocity using the double channel metric (top) and single channel metric (bottom).

We then repeat this procedure, but keep the original v_r and instead set $v_\phi = v_\mathrm{k}$, that is the azimuthal velocity is that of a Keplerian orbit. Finally, we force the velocity to be fully Keplerian, that is $v_r = 0$ and $v_\phi = v_\mathrm{k}$. Figure 4.5 shows the effect of changing the radial and azimuthal velocity of the gas on the moment 1 map. The top-left panel is simply the

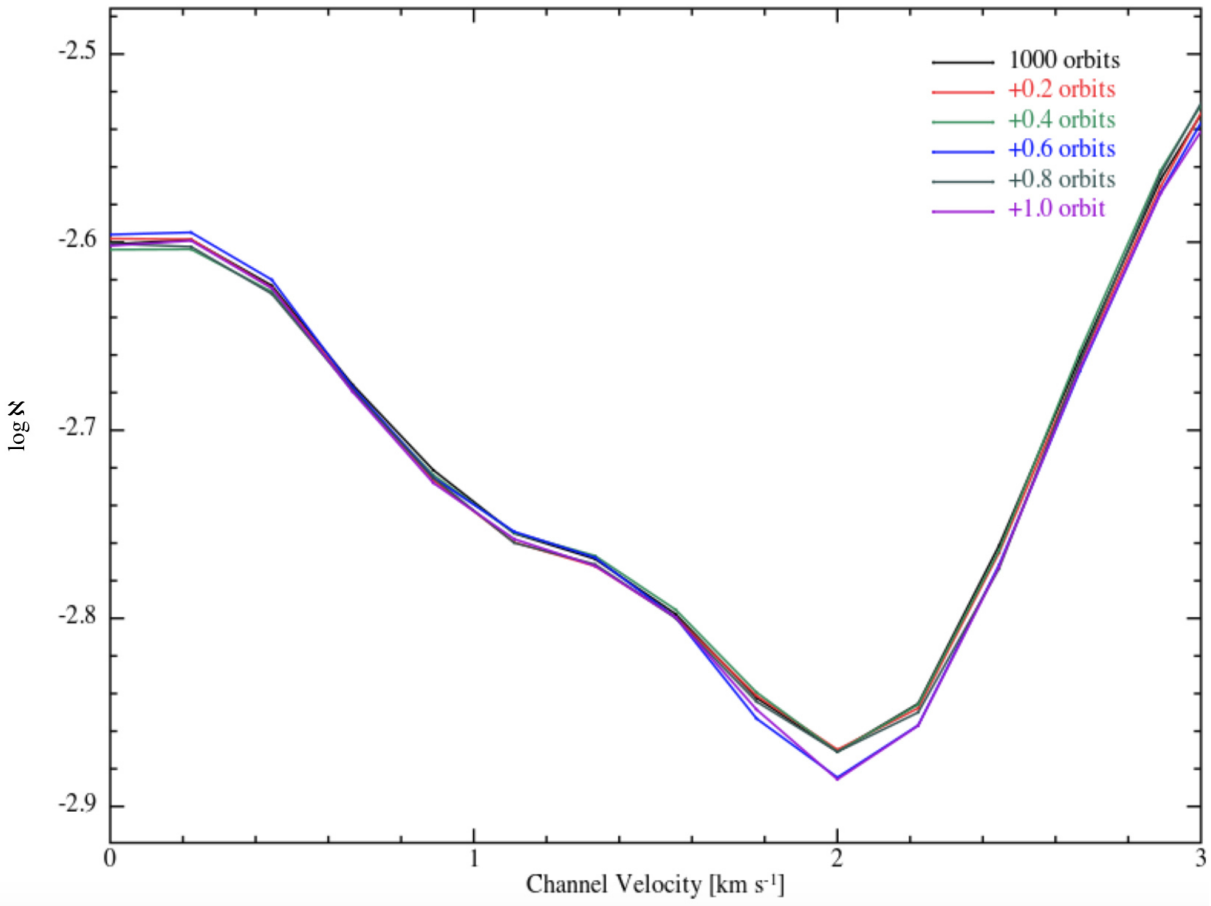

Figure 4.3: Asymmetry metric $\aleph_c$ as a function of channel velocity over one binary orbit for a coplanar disc with $(H/R)_{\rm in} = 0.05$ surrounding a circular binary with $q = 0.1$. Snapshots are taken every fifth of a binary orbit.

centre panel from Figure 4.4. When we remove the radial component of the velocity of the gas (top-right panel) this asymmetry largely vanishes, with the $v = 0$ line becoming much straighter. When we set the material to orbit with a Keplerian v_ϕ (bottom-left panel) the asymmetry remains. Finally, if we set the material on a purely Keplerian orbit (bottom-right panel) the shape resembles that of the observation with the radial velocity removed. This shows that the asymmetric shape of the moment 1 map is caused by the radial velocity of the material in the disc, while the deviations from Keplerian motion in the azimuthal direction have only a minor effect on the shape of the moment 1 map. The two most obvious sources of radial motion are binary-disc interactions and viscous accretion. Figure 4.6 compares the moment 1 maps of the fiducial disc with that of a disc with the same properties, but surrounding a single star. In the single star case the only source of radial motion is viscous accretion, and this is not strong enough to produce a twist in the moment 1 map. Therefore the source of the twist in the moment 1 maps of our discs is the companion.

The moment 2 map, being a map of velocity dispersion, has the strongest signal closest to the stars where velocities are highly perturbed by their strong gravitational influence. This allows us to probe inside the cavity despite the low densities that make the moment 0 signal vanish. When the disc is face-on to the observer (bottom left panel of Figure 4.4) two stars are clearly resolved. At the origin a strong signal is recovered, corresponding to the primary star, while a weaker signal from the secondary is seen slightly to the left. The signal becomes distorted, however, as the disc becomes inclined on the plane of the sky (middle-bottom and bottom-right panels). As the signal from the secondary is weaker, it is easily drowned out by the primary so we do not expect this to be a robust detection method and do not investigate it further.

4.4 Analysis of Asymmetry Metric

Figure 4.7 shows a selection of CO channel maps for our fiducial disc. Figure 4.8 shows the same selection of channel maps for a disc with the same properties surrounding a single star. Large asymmetries are visible in opposite channels of the fiducial disc which are not seen in the single star disc. We calculate $\aleph$ for the fiducial disc, as well as a suite of discs with increasing eccentricity up to $e = 0.9$, and for the single star disc. The variation of $\aleph$ with eccentricity is shown in Figure 4.9, plotted with the single star disc for comparison (note that the single-star disc is plotted as a horizontal line for ease of viewing, though binary orbital eccentricity has no physical meaning in this case). From this we can see that, with the exception of a circular binary, disc around binaries with $e > 0.4$ are more asymmetric than those around binaries with $e < 0.4$. Furthermore, even the least asymmetric circumbinary discs are roughly 3 times more asymmetric than a single star disc.

4.4.1 CO Isotopologues

Figure 4.10 shows channels maps for three different isotopologues of CO. When computing the channel maps we take an abundance relative to H_2 of 10^{-4} for CO, 1.4×10^{-6} for ^{13}CO, and 2×10^{-7} for C^{18}O. Naturally this leads to CO having the strongest signal due to the highest abundance. This high abundance, however, comes with a high optical thickness so CO traces the surface layers of the disc, while ^{13}CO and C^{18}O are closer to the disc midplane. All three isotopologues show similar asymmetric features, with the cavity extending further out in the positive branch than the negative. Figure 4.11 shows the variation of $\aleph$ with eccentricity for each isotopologue, and we see that the fainter

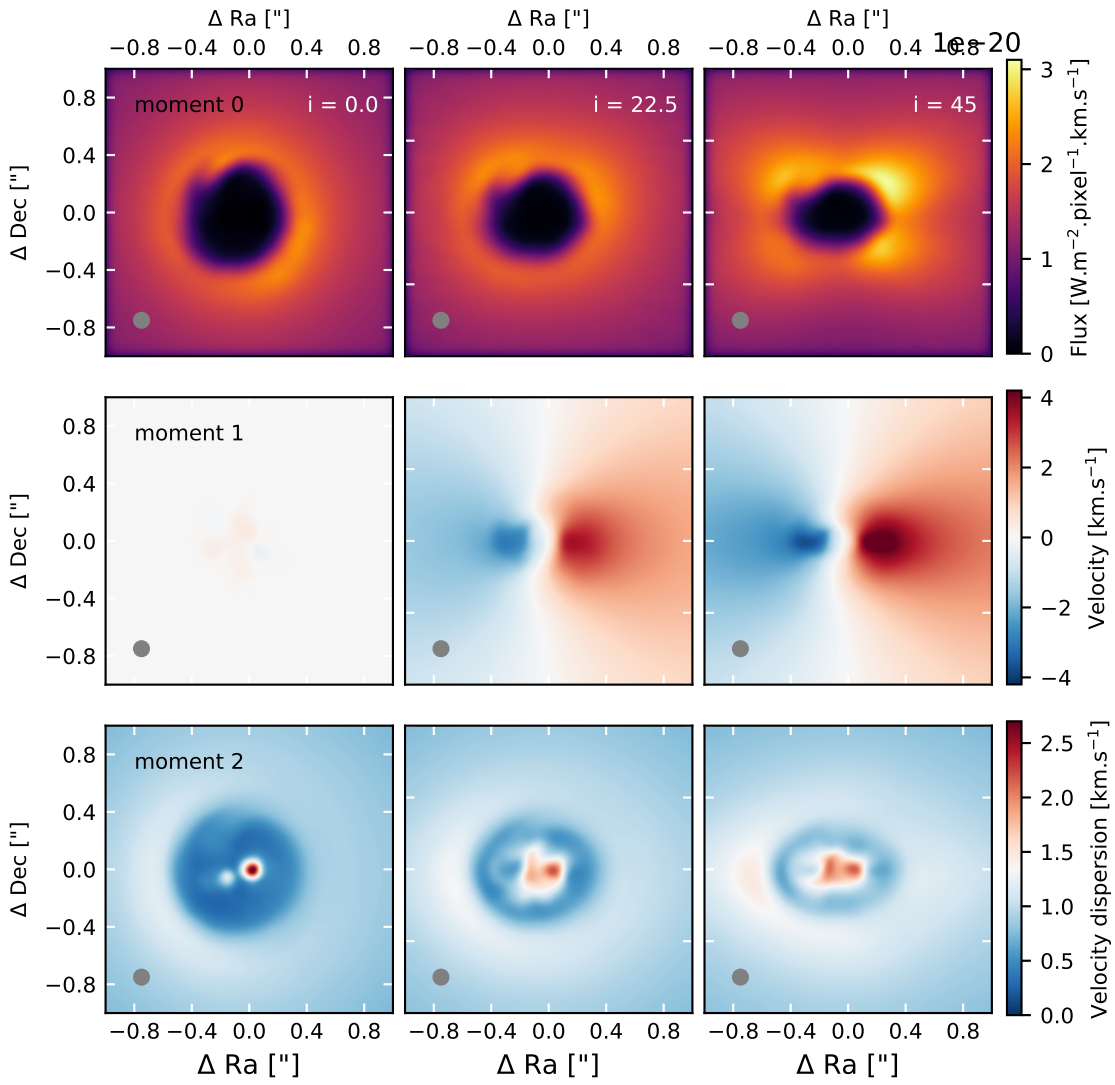

Figure 4.4: Moment maps of a coplanar disc with $(H/R)_{\rm in} = 0.05$ surrounding a binary with $q = 0.1$. Top row: moment 0 maps. Middle row: moment 1 maps. Bottom row: moment 2 maps. Left column is observed face on, middle column is inclined by 22.5° with respect to the plane of the sky, and right column is 45°.

signals are more asymmetric. This is due to the fact that binary-disc interactions are strongest in the disc midplane, thus the disruptive effects of these interactions will be most prominent in observations which probe the midplane. This behaviour is also seen in lowly inclined discs, in which a warp is present, but not in highly inclined discs which break (see Sections 4.4.3 and 4.5). The shape of the curves is largely the same for all three isotopologues, however, so the choice of which isotopologue to examine is largely arbitrary. As such we continue in this work to consider only the CO due to its higher signal strength.

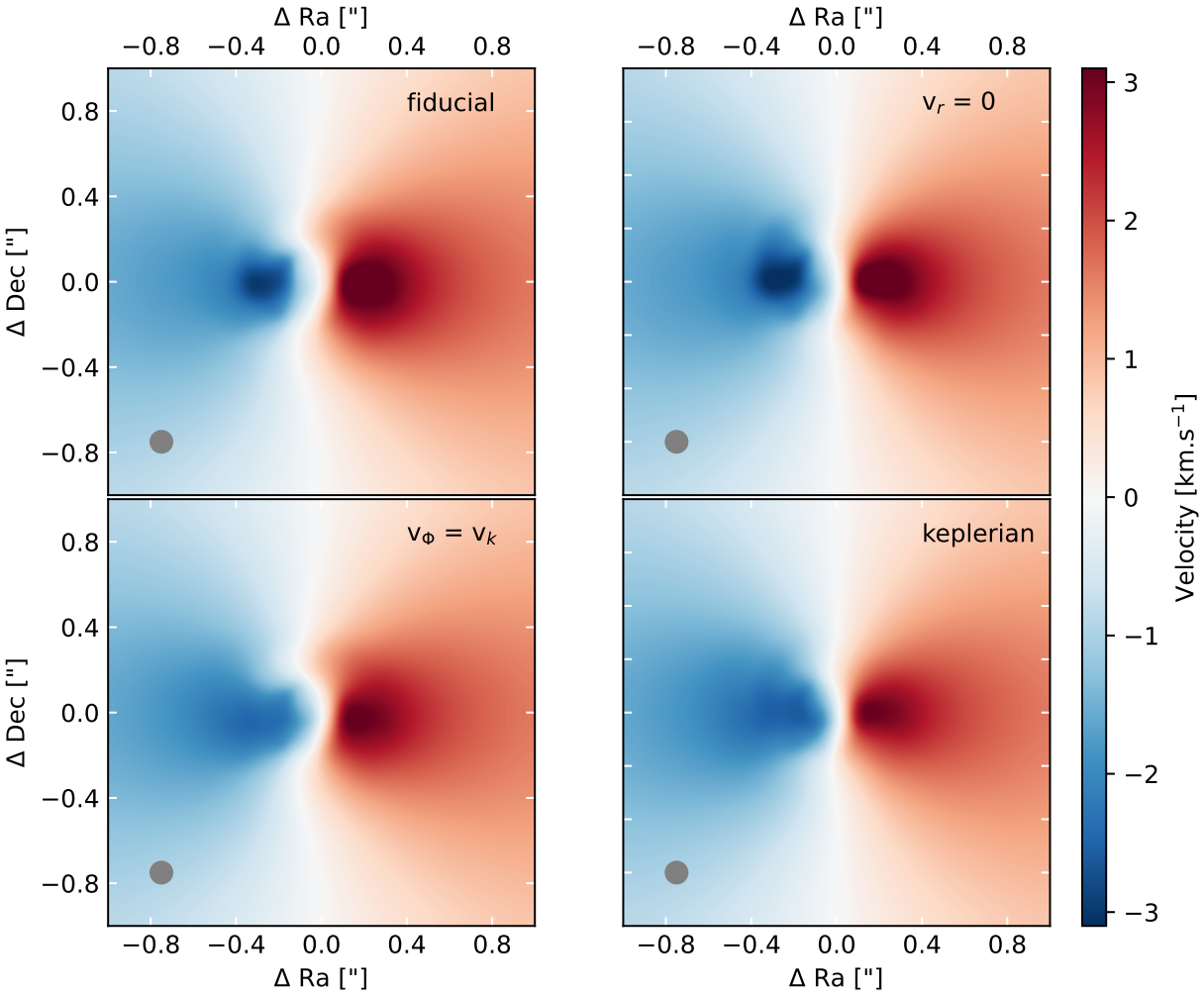

Figure 4.5: Top left panel: Moment 1 map of a coplanar disc with $(H/R)_{\rm in} = 0.05$ surrounding a binary with $q = 0.1$, oriented with an inclination of 22.5° on the plane of the sky (centre panel from Fig 4.4). Top right panel: Same, but with forcing $v_r = 0$. Bottom left panel: Same as top left, but with forcing $v_\phi = v_k$. Bottom right: Same as top left, but with forcing a fully Keplerian velocity.

4.4.2 Disc Scale Height

Figure 4.12 shows CO channel maps for discs with different scale heights. As the disc becomes thicker and therefore more viscous the cavity shrinks in the negative branch and becomes more rounded in the positive branch. Looking at Figure 4.13 we see that less viscous discs are more asymmetric. This is to be expected as viscosity acts to shrink and circularise the cavity, as seen in Section 3.3.3. This counteracts the dynamical effects from the binary which act to open a large, eccentric cavity, which leads to an increased ℵ.

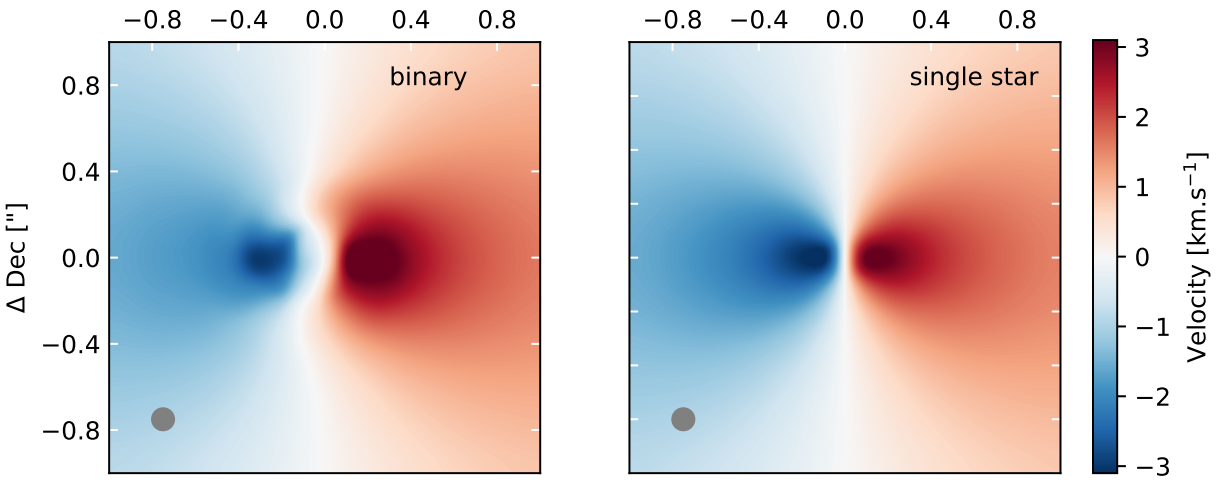

Figure 4.6: Left panel: Moment 1 map of a coplanar disc with $(H/R)_{\rm in} = 0.05$ surrounding a binary with $q = 0.1$, oriented with an inclination of 22.5° on the plane of the sky (centre panel from Fig 4.4). Right panel: Moment 1 map of a disc with the same properties, but surrounding a single star.

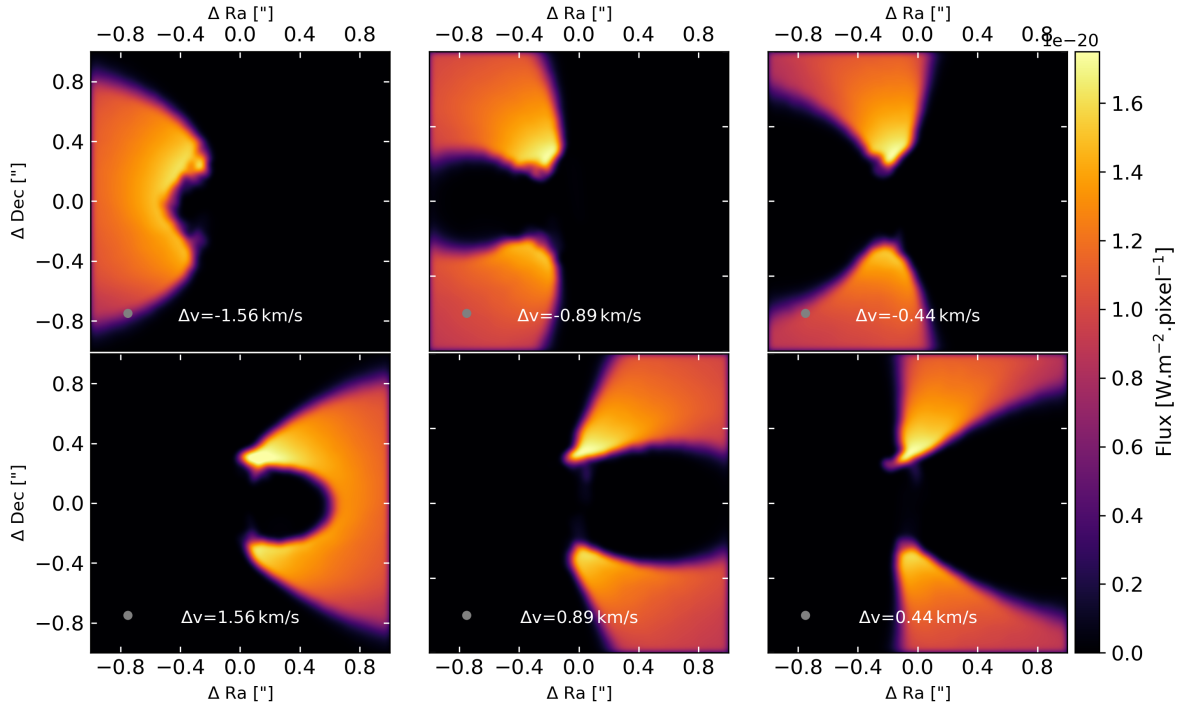

Figure 4.7: A selection of CO channel maps of a coplanar disc with $(H/R)_{\rm in} = 0.05$, surrounding a binary with $q = 0.1$, with an angle of 22.5° on the plane of the sky, after 1000 binary orbits. The top row shows only the negative branch and the bottom row shows the corresponding channels in the positive branch, highlighting the asymmetry in the disc.

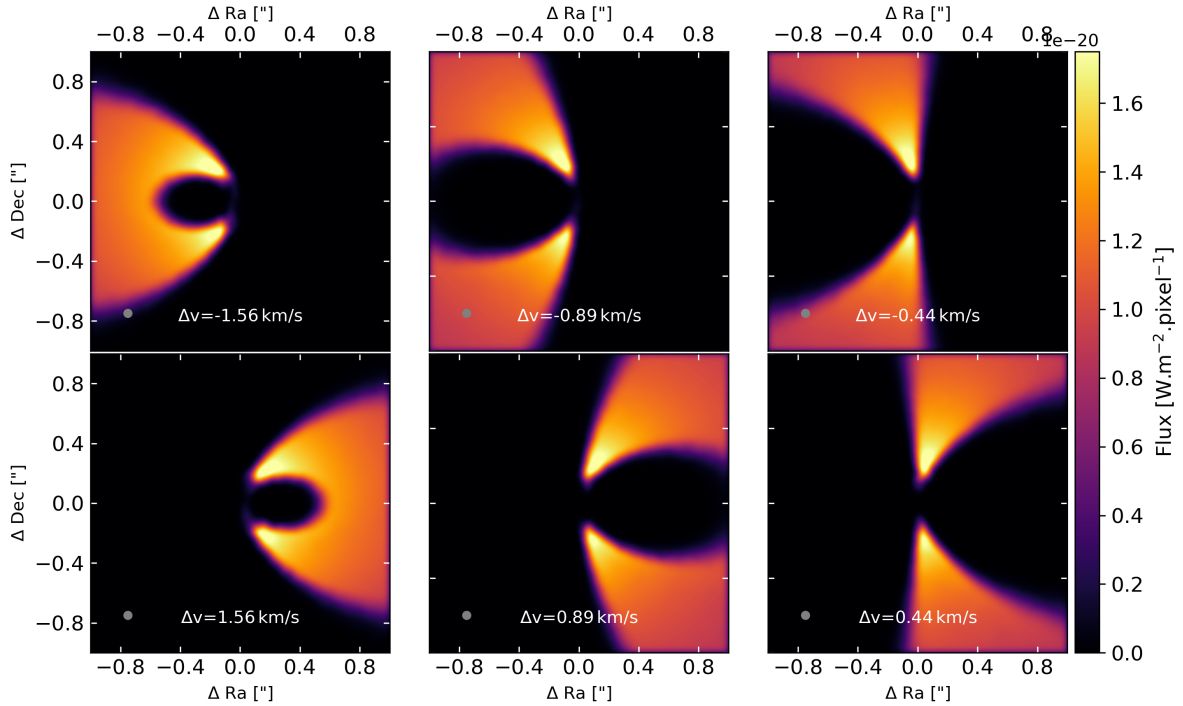

Figure 4.8: Same as Figure 4.7 but for a single star disc.

4.4.3 Disc Inclination

Figure 4.14 shows CO channel maps for discs with different initial inclinations between the binary and the disc. Of particular note is the structure in the $i = 45°$ case, which appears to not show a visible cavity. In this case the disc is strongly warping as it realigns with the binary (see Section 3.3.4, Figure 3.6). It is likely that this warp is obscuring the cavity and that at a later time the warp will have a different phase, allowing the cavity to be seen again. It is important to note, though, that the inner regions of the $i = 22.5°$ and $i = 45°$ discs are in a highly transient evolutionary stage as they settle into a coplanar or polar orbit. These discs are far from a steady state and their inclinations, cavity size, and asymmetry are constantly evolving. Indeed, figure 4.15 shows that there is no clear trend with $\aleph$ due to the mutual inclination between the binary and the disc during this volatile phase. In the long term, when the discs have reached a steady state we expect $\aleph$ of the initially inclined discs to follow that of an initially coplanar or polar disc, depending on their final configuration.

4.4.4 Binary Mass Ratio

Figure 4.16 shows CO channel maps for discs with different binary mass ratios. We can clearly see the smaller cavity in the $q = 0.01$ disc than in the other discs. Indeed, figure 4.17 reflects this dichotomy. Ignoring the equal mass binary for a moment we see that the $q = 0.1$ and $q = 0.3$ discs have a similar $\aleph$ while the $q = 0.01$ disc is roughly 0.5

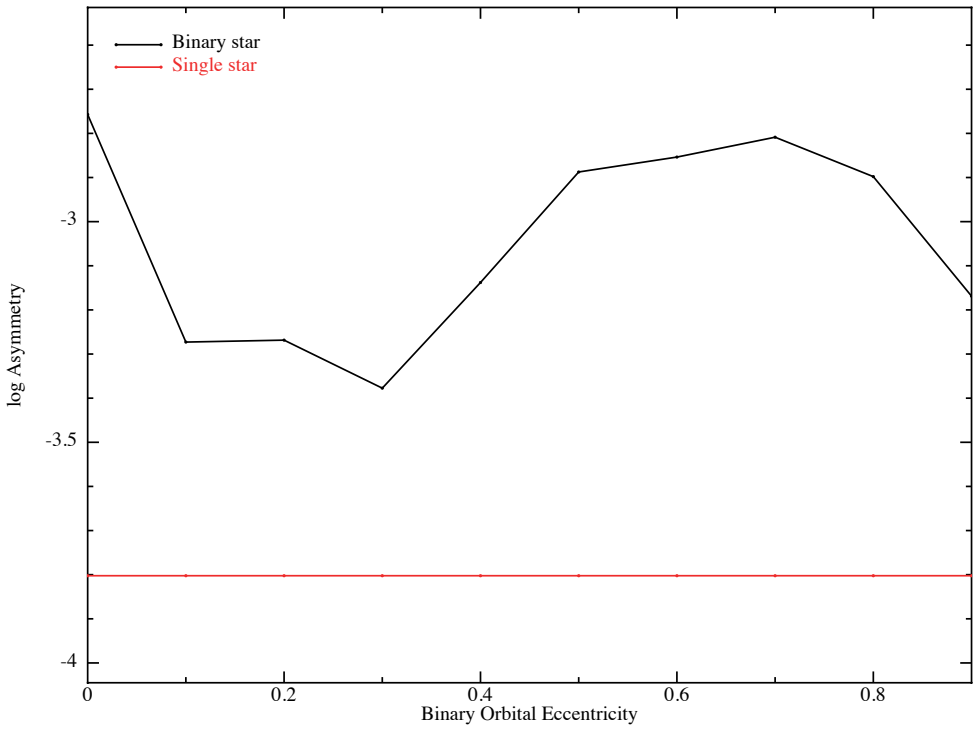

Figure 4.9: Black line: Asymmetry as a function of binary orbital eccentricity for a coplanar disc with $(H/R)_{\rm in} = 0.05$ surrounding a binary with $q = 0.1$ after 1000 binary orbits. Red line: Asymmetry of a single star disc with the same properties. Note that binary orbital eccentricity has no meaning for a single star disc, and this disc is only plotted as a horizontal line for ease of comparison with the suite of circumbinary discs.

dex lower. This implies that there is some mass ratio above which the asymmetry stops increasing, though a finer resolution in q would be needed to find that value. We note here that in the $q = 0.01$ simulations the secondary falls into the massive planet regime, due to the primary mass $M_1 = 1\ M_\odot$ that we take, though this would not be the case for a larger primary with the same mass ratio. The asymmetry of the equal mass binary discs varies greatly with binary eccentricity, showing no clear trend. One possible explanation for this is that the extra symmetry present in the system due to the stellar masses being equal makes א more sensitive to the orbital phase. Simulations with a higher temporal resolution would be needed in order to test this.

4.5 Discussion

In defining א, and while discussing the physical features present in the discs, we frequently refer to the positive and negative branches of the channel maps. It is important to stress that discussing these branches are unique to each individual disc. This is because which half of the disc appears in which branch is dependant on both the phase of the orbit and

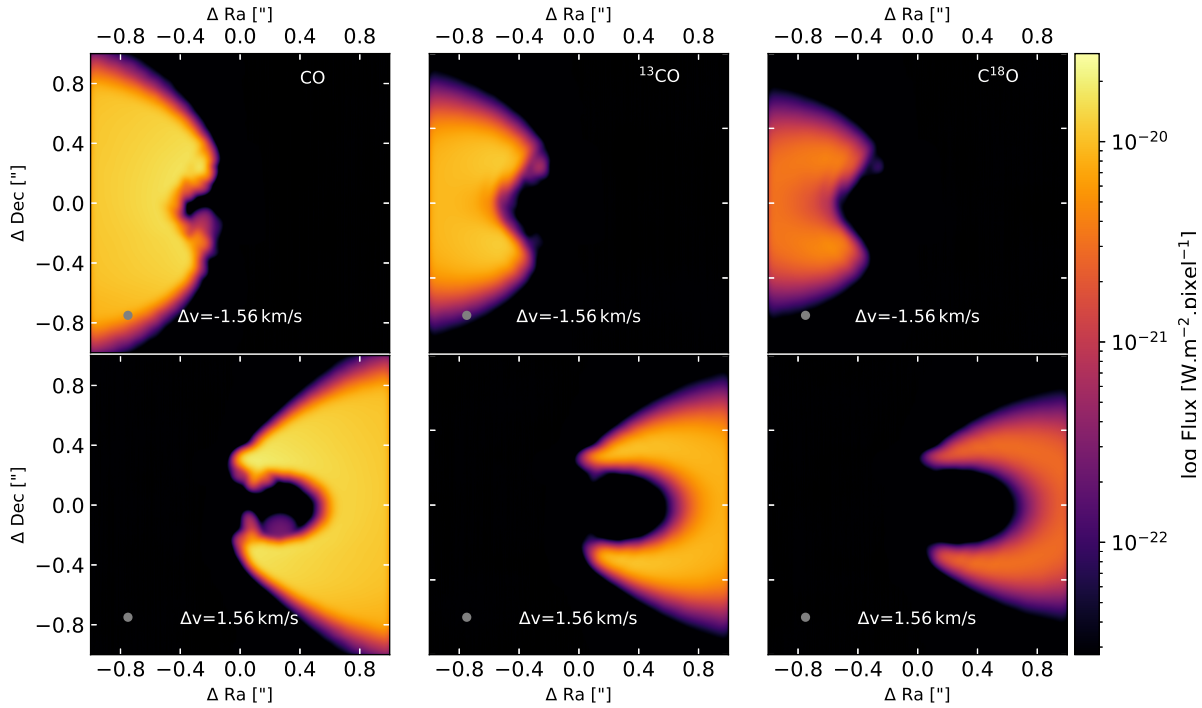

Figure 4.10: Channel maps for three different CO isotopologues in a coplanar disc with $(H/R)_{\rm in} = 0.05$, surrounding a binary with $q = 0.1$, with an angle of 22.5° on the plane of the sky, after 1000 binary orbits. Left column: CO. Middle column ^{13}CO. Right column C^{18}O. Note that the colour bar is in log scale, unlike all other channel maps in this work, which are in linear scale.

the position of the observer. For example, if the observer was positioned on the other side of the disc the positive and negative branches would be swapped. Therefore we caution the reader that a feature we see in, e.g., the positive branch is not constrained to only ever appear in the positive branch for all discs.

In Section 4.2 we mention that $\aleph_c$ is defined in a way that makes it insensitive to field of view, though this is not the case for a broken disc where the inner and outer discs are misaligned. Figure 4.18 shows some channel maps of one such disc. In the right hand column the outer disc is clearly visible and we can see that it has a different axis of symmetry to the inner disc. In the left hand column the outer disc is only slightly in frame, so $\aleph_c$ is only measuring the asymmetry of the inner disc. Increasing the field of view would make the outer disc visible. Since the outer disc has a different axis of symmetry this would necessarily introduce asymmetries in the image even in the case that the outer regions of the inner disc are highly symmetrical. Thus care must be taken when calculating $\aleph$ for broken discs to only consider the inner disc. In these cases, however, $\aleph$ as a method to infer the presence of an unseen companion may be unnecessary since the broken disc is visible in the channel maps and a broken disc is already a strong signature of a binary.

An obvious area for future work would be to perform similar analyses on real observa-

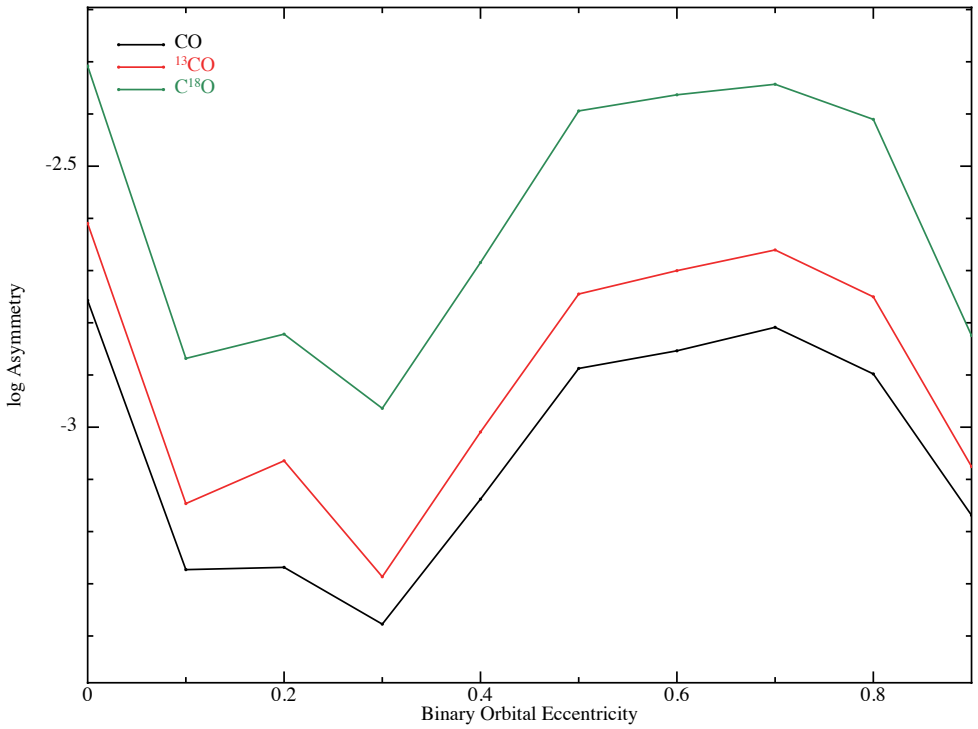

Figure 4.11: Asymmetry as a function of binary orbital eccentricity for a coplanar disc with $(H/R)_{\rm in} = 0.05$ surrounding a binary with $q = 0.1$ after 1000 binary orbits. Different lines depict discs with different CO isotopologues.

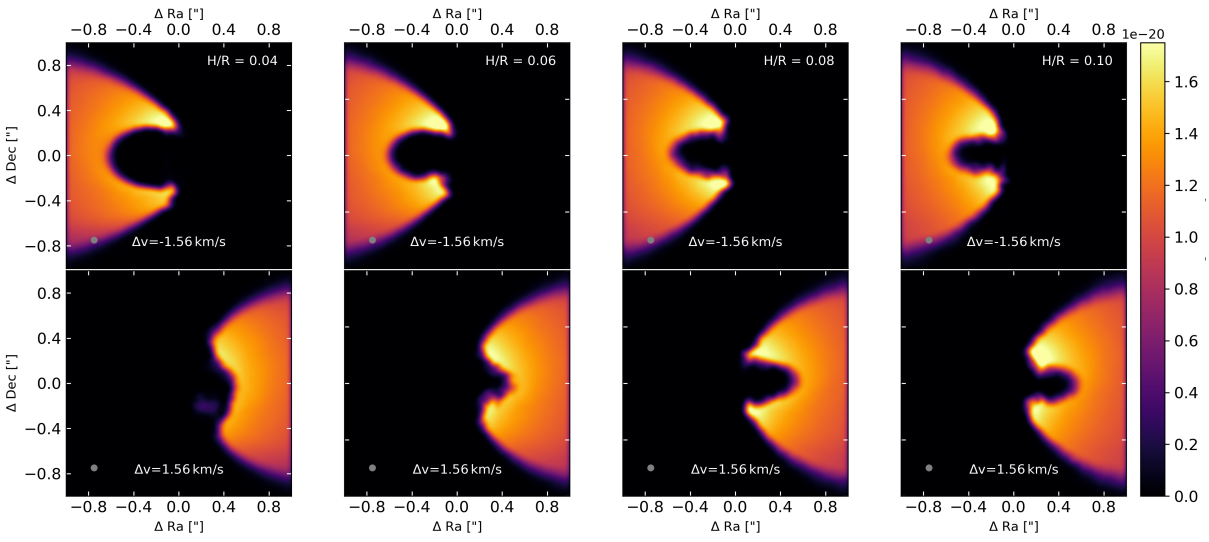

Figure 4.12: CO channel maps for coplanar discs surrounding a binary with $q = 0.1$, with an angle of 22.5° on the plane of the sky, after 1000 binary orbits. Each column has a different aspect ratio: $H/R = 0.04$, 0.0, 0.08, 0.10 from left to right.

tion, rather than the synthetic observations presented here. Calculating ℵ for a number of known circumbinary discs, such as HD 142527, would be an interesting way to test its validity in inferring the presence of a binary companion. A crucial question here is the

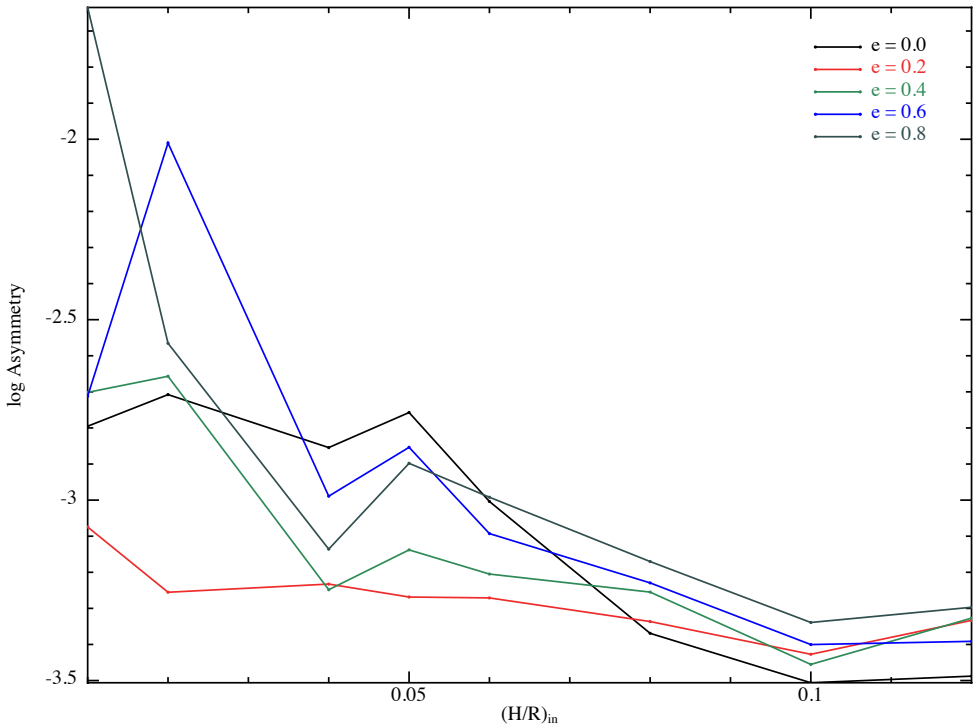

Figure 4.13: Asymmetry as a function of disc aspect ratio for coplanar discs surrounding a binary with q = 0.1 after 1000 binary orbits. Different lines depict discs with different binary orbital eccentricities.

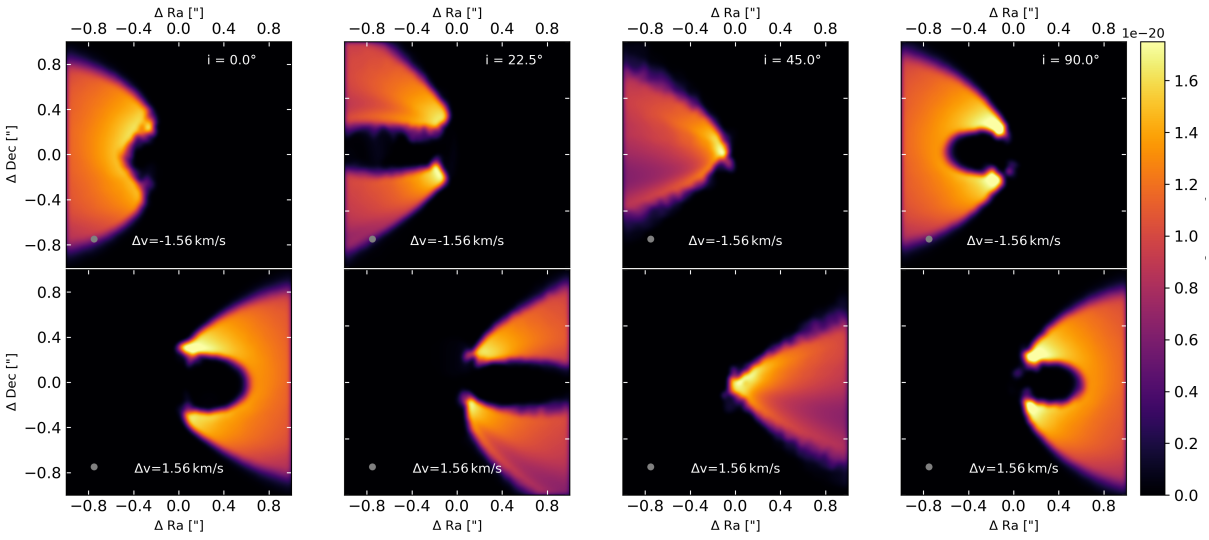

Figure 4.14: CO channel maps for discs with $(H/R)_{\rm in} = 0.05$ surrounding a binary with $q = 0.1$, with an angle of 22.5° on the plane of the sky, after 1000 binary orbits. Each column has a different binary-disc inclination: $i = 0.0°$, 22.5°, 45.0°, 90.0° from left to right.

smallest distinguishable difference in ℵ between two discs. While discs hosting large companions on highly eccentric orbits are over an order of magnitude more asymmetric than

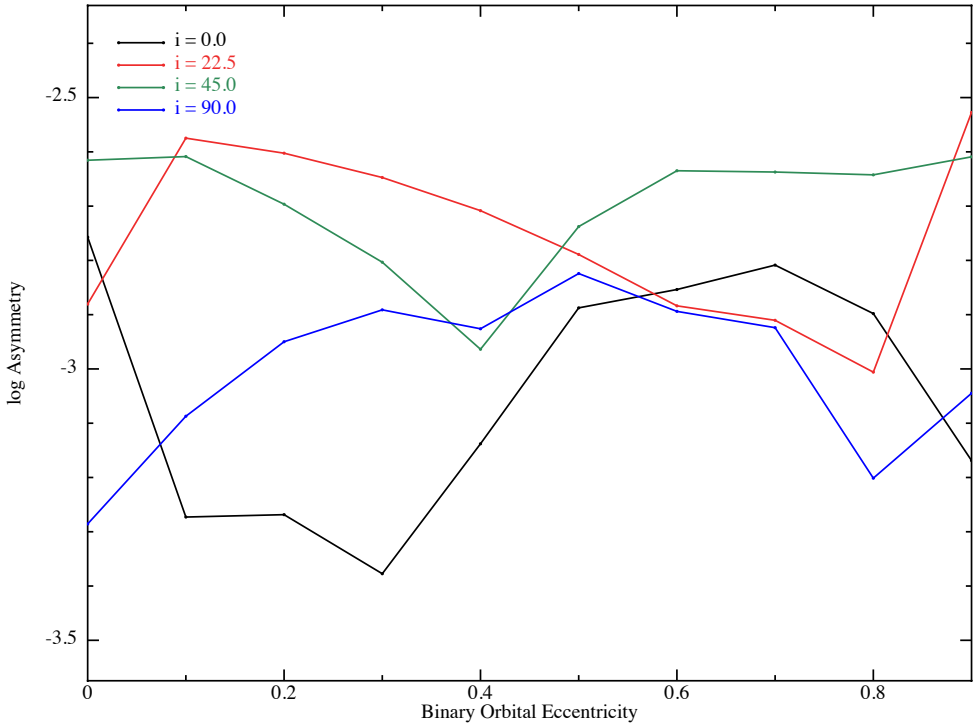

Figure 4.15: Asymmetry as a function of binary orbital eccentricity for discs with $(H/R)_{\rm in} = 0.05$ surrounding a binary with $q = 0.1$ after 1000 binary orbits. Different lines depict binaries with different inclinations.

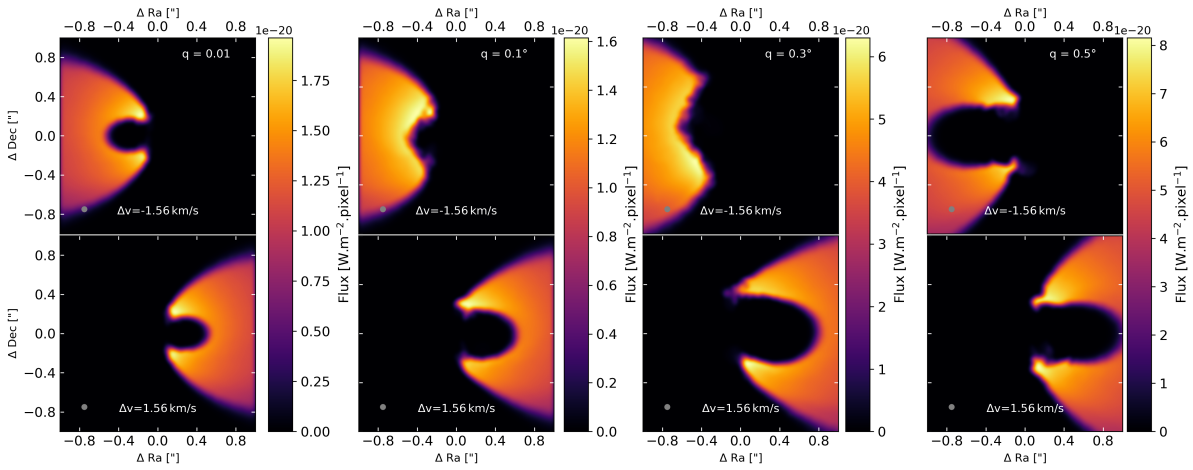

Figure 4.16: CO channel maps for coplanar discs with $(H/R)_{\rm in} = 0.05$ and an angle of 22.5° on the plane of the sky, after 1000 binary orbits. Each column has a different binary mass ratio: $q = 0.01$, 0.1, 0.3, 0.5 from left to right.

single star discs, planetary companions on near-circular orbits can be have a difference as low as 0.3 dex, the detectability of which needs to be tested. Once confirmed this could be applied to transitional discs without a known companion, such as IRS 48 or CQ Tau, to infer whether or not one is there.

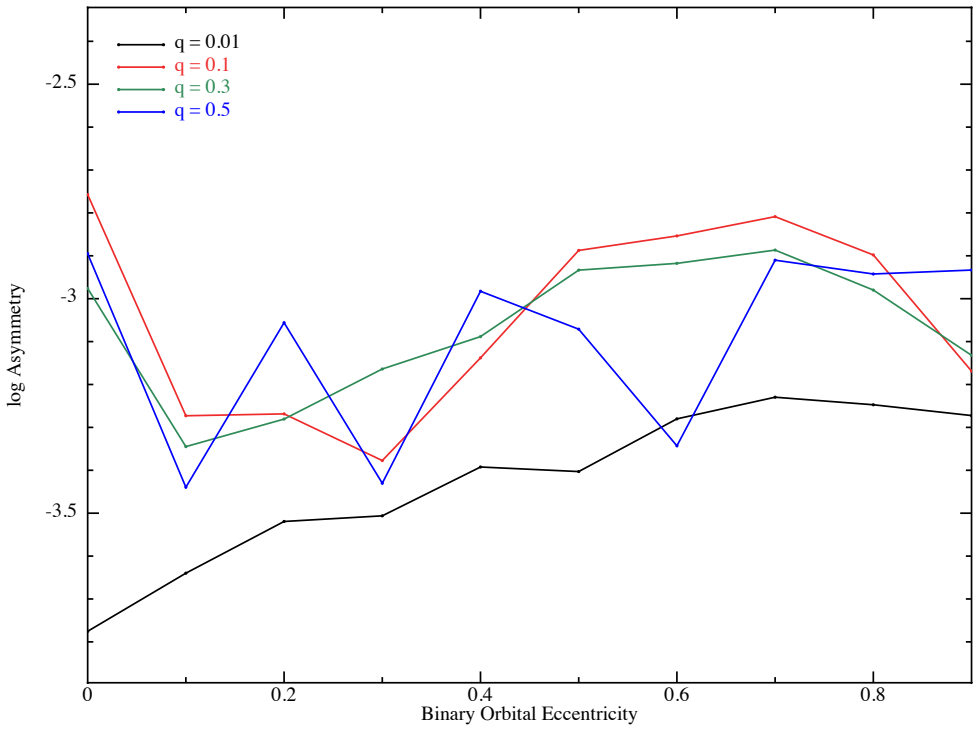

Figure 4.17: Asymmetry as a function of binary orbital eccentricity for a coplanar disc with $(H/R)_{\rm in} = 0.05$ after 1000 binary orbits. Different lines depict binaries with different mass ratios.

Similarly, investigating the moment 1 maps of known circumbinaries for the twist discussed in Section 2.3.4 could confirm its legitimacy, after which it too can be applied to other discs which may be hiding a second star. Moment 1 maps of HD 142527 were presented by Boehler et al. (2017) (Figure 5) and of IRS 48 by van der Marel et al. (2016a) (Figure 2). IRS 48 shows a clear twist, while HD 142527 shows almost none, implying that testing more parameters would be useful in determining when the twist is and isn't expected to be present. This is already an active area of interest as Calcino et al. (2019) modelled IRS 48 as a circumbinary using `PHANTOM` and found a twist in their moment 1 maps comparable to van der Marel et al. (2016a).

While we do not analyse the moment 2 maps we do note that under the right conditions a binary companion can be resolved. Computing a moment 2 map is no more computationally expensive than computing a moment 1 map. As such we recommend calculating moment 2 maps as a relatively cheap, though highly unlikely, way of detecting a binary companion.

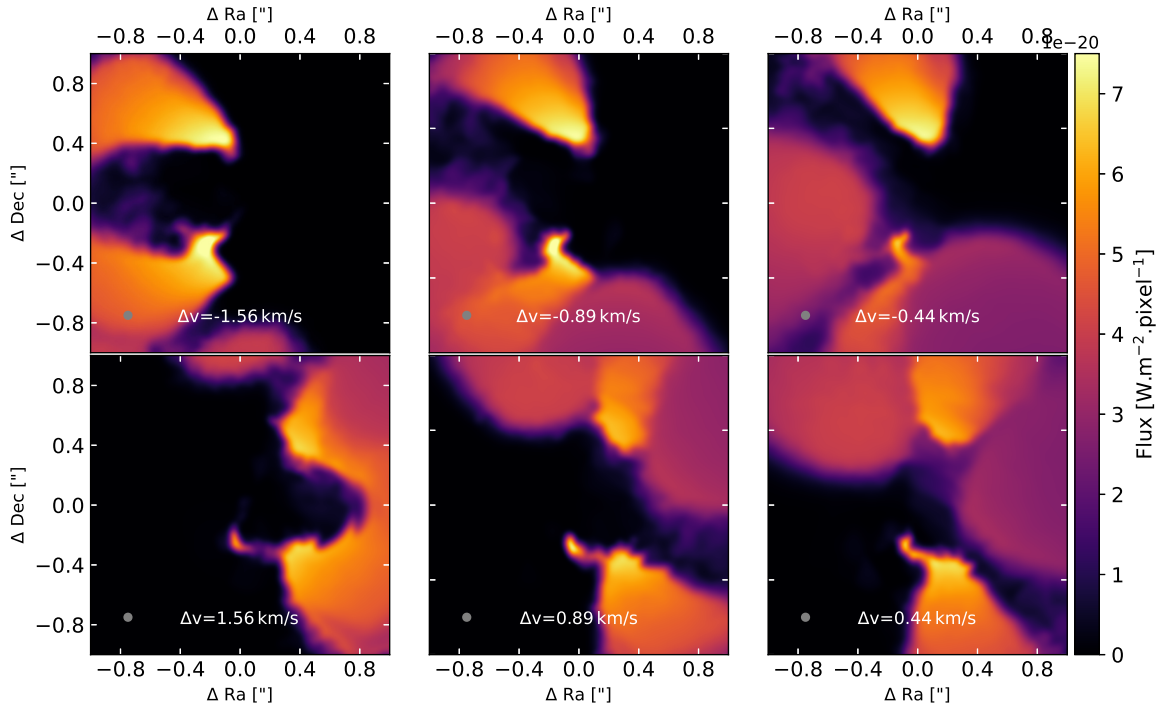

Figure 4.18: CO channel maps for a broken disc with a large misalignment between the inner and outer discs. At low Δv the outer disc is visible, and obscures parts of the inner disc.

4.6 Conclusion

We have generated a suite of synthetic observations of circumbinary discs, examining them to find signatures of the binary in these observations. We have also developed a metric to quantify the asymmetry, $\aleph$, in the channel maps and applied it to our synthetic CO channel maps. Our conclusions are:

1. The radial motion of the gas caused by binary-disc interactions leads to a twist in the moment 1 maps.

2. Single star discs have an asymmetry of $\log(\aleph) \sim -3.8$. The most symmetric circumbinary discs have a large scale height and low binary eccentricity. In these cases we find $\log(\aleph) \sim -3.5$. Conversely, thin discs around highly eccentric binaries can have asymmetries of $\log(\aleph) \sim -2$.

3. In discs that are face on to the observer moment 2 maps show a clearly resolved binary, though even small inclinations leaves the binary unresolved.

While a twisted moment 1 map, or an asymmetry of $\log(\aleph) \gtrsim -3.5$, do not constitute detections of a stellar companion, they do strongly hint towards their presence. As such, they can be used to identify systems that would make a good candidate for deeper observations with the intent of detecting a stellar companion.

Chapter 5

Conclusions

In this thesis we investigate the effects of a binary on the evolution and appearance of the surrounding disc. To this end we perform 3-dimensional Smoothed Particle Hydrodynamics simulations of circumbinary discs using the code `PHANTOM` in an attempt to understand their dynamical properties. We then compute synthetic observations of these discs using the radiative transfer code `MCFOST`.

We find two important timescales in the opening of a cavity in circumbinary discs. A cavity is quickly opened on a dynamical time, tens of binary orbits, while the long term cavity size is set on the viscous time, which varies from thousands to tens of thousands of binary orbits depending on the scale height of the disc.

We recover a cavity size that is $2 - 5$ times the binary semi-major axis. This is consistent with the analytical predictions of Artymowicz and Lubow (1994) and Miranda and Lai (2015). The cavity size is an increasing function of binary eccentricity and a decreasing function of disc scale height, that is to say that less viscous discs host larger cavities. The cavity size is an increasing function of binary mass ratio, with the exception of binaries with low eccentricity, $e \lesssim 0.2$, where a local maximum exists at $q \simeq 0.3$. These constraints on the cavity size can help to inform the potential orbits of an unresolved binary companion in a suspected circumbinary disc.

When simulating inclined circumbinary discs we find that the inner disc will always tend towards a polar of coplanar configuration and that this final configuration determines the cavity size. An initially polar disc has a cavity size that is nearly 50% smaller than that of an initially coplanar disc. An intermediately inclined disc that tend towards a coplanar alignment has a cavity slightly smaller than that of an initially coplanar disc, with cavity size decreasing as initial inclination increases. A disc that tends towards a polar alignment can either break or warp, greatly affecting the cavity size. A disc that

breaks aligns on the dynamical time, and has a cavity as big as an initially polar disc. A disc that warps stays inclined for longer, so opens a larger cavity which then closes due to viscous evolution as the inclination increases with time. A large number of our simulated discs remained in an inclined state even after 1,000 binary orbits, suggesting that inclined discs are not uncommon. Indeed, simulations of circumbinary discs need to take binary-disc inclination into account.

In our synthetic observations we find a twist in the moment 1 maps in the zero line of sight iso-velocity line. This twist is due to the radial motion of the material in the disc, induced by the presence of a binary in our simulations.

We developed a metric, ℵ, to measure the asymmetry in the channel maps. From this metric we found that circumbinary discs have $\log(\aleph) \gtrsim -3.5$. For the thinnest disc around an eccentric binary ℵ can be over an order of magnitude more asymmetric than an equivalent single star disc. This metric, as well as a visible twist in the moment 1 map, can be used to find discs with may be hiding a stellar companion and would be good candidates for further observations.

Finally, we find that the moment 2 map can reveal a resolved stellar companion in a close to face-on disc. While we do not expect this to be a robust detection method we note that computing a moment 2 map is no more computationally expensive than computing a moment 1 map, and thus can serendipitously be an easy method of detecting a companion in specific circumstances.

This work opens avenues for further exploration. We have considered gas only discs, not taking dust into account. Recently a number of works have simulated dusty discs in binary systems in order to compare with observations (e.g: Price et al., 2018a; Calcino et al., 2019; Gonzalez et al., 2020; Ragusa et al., 2021), however simulations of dusty circumbinary discs mimicking those in Chapter 3 would be useful in determining the cavity size in the dust phase.

In Chapter 4 we only consider synthetic observations. Searching for twists in the moment 1 maps of known circumbinary discs, as well as the lack thereof in known single star discs, would test its validity as a method of inferring the presence of a binary. Calculating ℵ from real observations would have similar benefits. Once confirmed, these methods could be used to infer the presence of currently unknown stellar companions and find candidate discs for deeper observations with the intent of detecting the companion.

Bibliography

Adams, F. C., Lada, C. J., and Shu, F. H. (1987). Spectral Evolution of Young Stellar Objects. ApJ, 312:788.

Alexander, R., Pascucci, I., Andrews, S., Armitage, P., and Cieza, L. (2014). The Dispersal of Protoplanetary Disks. In Beuther, H., Klessen, R. S., Dullemond, C. P., and Henning, T., editors, Protostars and Planets VI, page 475.

Aly, H., Dehnen, W., Nixon, C., and King, A. (2015). Misaligned gas discs around eccentric black hole binaries and implications for the final-parsec problem. MNRAS, 449:65–76.

Aly, H., Lodato, G., and Cazzoletti, P. (2018). On the secular evolution of GG Tau A circumbinary disc: a misaligned disc scenario. MNRAS, 480(4):4738–4745.

Andre, P. and Montmerle, T. (1994). From T Tauri Stars to Protostars: Circumstellar Material and Young Stellar Objects in the rho Ophiuchi Cloud. ApJ, 420:837.

Andrews, S. M., Chandler, C. J., Isella, A., Birnstiel, T., Rosenfeld, K. A., Wilner, D. J., Pérez, L. M., Ricci, L., Carpenter, J. M., Calvet, N., Corder, S. A., Deller, A. T., Dullemond, C. P., Greaves, J. S., Harris, R. J., Henning, T., Kwon, W., Lazio, J., Linz, H., Mundy, L. G., Sargent, A. I., Storm, S., and Testi, L. (2014). Resolved Multifrequency Radio Observations of GG Tau. ApJ, 787:148.

Andrews, S. M., Rosenfeld, K. A., Kraus, A. L., and Wilner, D. J. (2013). The Mass Dependence between Protoplanetary Disks and their Stellar Hosts. ApJ, 771:129.

Andrews, S. M., Wilner, D. J., Espaillat, C., Hughes, A. M., Dullemond, C. P., McClure, M. K., Qi, C., and Brown, J. M. (2011). Resolved Images of Large Cavities in Protoplanetary Transition Disks. ApJ, 732:42.

Armitage, P. J. (2007). Massive Planet Migration: Theoretical Predictions and Comparison with Observations. ApJ, 665(2):1381–1390.

Armitage, P. J. (2010). Astrophysics of Planet Formation.

Artymowicz, P. and Lubow, S. H. (1994). Dynamics of binary-disk interaction. 1: Resonances and disk gap sizes. ApJ, 421:651–667.

Ataiee, S., Pinilla, P., Zsom, A., Dullemond, C. P., Dominik, C., and Ghanbari, J. (2013). Asymmetric transition disks: Vorticity or eccentricity? A&A, 553:L3.

Avenhaus, H., Quanz, S. P., Schmid, H. M., Dominik, C., Stolker, T., Ginski, C., de Boer, J., Szulágyi, J., Garufi, A., Zurlo, A., Hagelberg, J., Benisty, M., Henning, T., Ménard, F., Meyer, M. R., Baruffolo, A., Bazzon, A., Beuzit, J. L., Costille, A., Dohlen, K., Girard, J. H., Gisler, D., Kasper, M., Mouillet, D., Pragt, J., Roelfsema, R., Salasnich, B., and Sauvage, J.-F. (2017). Exploring Dust around HD 142527 down to 0.025 (4 au) Using SPHERE/ZIMPOL. AJ, 154:33.

Avenhaus, H., Quanz, S. P., Schmid, H. M., Meyer, M. R., Garufi, A., Wolf, S., and Dominik, C. (2014). Structures in the Protoplanetary Disk of HD142527 Seen in Polarized Scattered Light. ApJ, 781(2):87.

Balbus, S. A. and Hawley, J. F. (1991). A Powerful Local Shear Instability in Weakly Magnetized Disks. I. Linear Analysis. ApJ, 376:214.

Balbus, S. A. and Hawley, J. F. (1998). Instability, turbulence, and enhanced transport in accretion disks. Reviews of Modern Physics, 70:1–53.

Baraffe, I., Chabrier, G., Allard, F., and Hauschildt, P. H. (1998). Evolutionary models for solar metallicity low-mass stars: mass-magnitude relationships and color-magnitude diagrams. A&A, 337:403–412.

Bate, M. R., Bonnell, I. A., and Price, N. M. (1995). Modelling accretion in protobinary systems. MNRAS, 277:362–376.

Begelman, M. C., McKee, C. F., and Shields, G. A. (1983). Compton heated winds and coronae above accretion disks. I. Dynamics. ApJ, 271:70–88.

Benisty, M., Stolker, T., Pohl, A., de Boer, J., Lesur, G., Dominik, C., Dullemond, C. P., Langlois, M., Min, M., Wagner, K., Henning, T., Juhasz, A., Pinilla, P., Facchini, S., Apai, D., van Boekel, R., Garufi, A., Ginski, C., Ménard, F., Pinte, C., Quanz, S. P., Zurlo, A., Boccaletti, A., Bonnefoy, M., Beuzit, J. L., Chauvin, G., Cudel, M., Desidera, S., Feldt, M., Fontanive, C., Gratton, R., Kasper, M., Lagrange, A.-M., LeCoroller, H., Mouillet, D., Mesa, D., Sissa, E., Vigan, A., Antichi, J., Buey, T., Fusco, T., Gisler, D., Llored, M., Magnard, Y., Moeller-Nilsson, O., Pragt, J., Roelfsema, R., Sauvage, J.-F., and Wildi, F. (2017). Shadows and spirals in the protoplanetary disk HD 100453. A&A, 597:A42.

Benz, W. (1990). Smooth Particle Hydrodynamics - a Review. In Buchler, J. R., editor, Numerical Modelling of Nonlinear Stellar Pulsations Problems and Prospects, page 269.

Biller, B., Lacour, S., Juhász, A., Benisty, M., Chauvin, G., Olofsson, J., Pott, J.-U., Müller, A., Sicilia-Aguilar, A., Bonnefoy, M., Tuthill, P., Thebault, P., Henning, T., and Crida, A. (2012). A Likely Close-in Low-mass Stellar Companion to the Transitional Disk Star HD 142527. ApJ, 753(2):L38.

Bjorkman, J. E. and Wood, K. (2001). Radiative Equilibrium and Temperature Correction in Monte Carlo Radiation Transfer. ApJ, 554(1):615–623.

Bodman, E. H. L. and Quillen, A. (2015). Infrared variability from circumbinary disc temperature modulations. MNRAS, 453(3):2387–2398.

Boehler, Y., Weaver, E., Isella, A., Ricci, L., Grady, C., Carpenter, J., and Perez, L. (2017). A Close-up View of the Young Circumbinary Disk HD 142527. ApJ, 840(1):60.

Boneberg, D. M., Panić, O., Haworth, T. J., Clarke, C. J., and Min, M. (2016). Determining the mid-plane conditions of circumstellar discs using gas and dust modelling: a study of HD 163296. MNRAS, 461(1):385–401.

Calcino, J., Price, D. J., Pinte, C., van der Marel, N., Ragusa, E., Dipierro, G., Cuello, N., and Christiaens, V. (2019). Signatures of an eccentric disc cavity: Dust and gas in IRS 48. MNRAS, 490(2):2579–2587.

Calvet, N., D'Alessio, P., Watson, D. M., Franco-Hernández, R., Furlan, E., Green, J., Sutter, P. M., Forrest, W. J., Hartmann, L., Uchida, K. I., Keller, L. D., Sargent, B., Najita, J., Herter, T. L., Barry, D. J., and Hall, P. (2005). Disks in Transition in the Taurus Population: Spitzer IRS Spectra of GM Aurigae and DM Tauri. ApJ, 630:L185–L188.

Canovas, H., Montesinos, B., Schreiber, M. R., Cieza, L. A., Eiroa, C., Meeus, G., de Boer, J., Ménard, F., Wahhaj, Z., Riviere-Marichalar, P., Olofsson, J., Garufi, A., Rebollido, I., van Holstein, R. G., Caceres, C., Hardy, A., and Villaver, E. (2018). DZ Chamaeleontis: a bona fide photoevaporating disc. A&A, 610:A13.

Casassus, S., Avenhaus, H., Pérez, S., Navarro, V., Cárcamo, M., Marino, S., Cieza, L., Quanz, S. P., Alarcón, F., Zurlo, A., Osses, A., Rannou, F. R., Román, P. E., and Barraza, M. (2018). An inner warp in the DoAr 44 T Tauri transition disc. MNRAS, 477:5104–5114.

Casassus, S., Marino, S., Pérez, S., Roman, P., Dunhill, A., Armitage, P. J., Cuadra, J., Wootten, A., van der Plas, G., Cieza, L., Moral, V., Christiaens, V., and Montesinos,

M. (2015a). Accretion Kinematics through the Warped Transition Disk in HD142527 from Resolved CO(6-5) Observations. ApJ, 811:92.

Casassus, S., Perez M., S., Jordán, A., Ménard, F., Cuadra, J., Schreiber, M. R., Hales, A. S., and Ercolano, B. (2012). The Dynamically Disrupted Gap in HD 142527. ApJ, 754(2):L31.

Casassus, S., van der Plas, G., M, S. P., Dent, W. R. F., Fomalont, E., Hagelberg, J., Hales, A., Jordán, A., Mawet, D., Ménard, F., Wootten, A., Wilner, D., Hughes, A. M., Schreiber, M. R., Girard, J. H., Ercolano, B., Canovas, H., Román, P. E., and Salinas, V. (2013). Flows of gas through a protoplanetary gap. Nature, 493:191–194.

Casassus, S., Wright, C. M., Marino, S., Maddison, S. T., Wootten, A., Roman, P., Pérez, S., Pinilla, P., Wyatt, M., Moral, V., Ménard, F., Christiaens, V., Cieza, L., and van der Plas, G. (2015b). A Compact Concentration of Large Grains in the HD 142527 Protoplanetary Dust Trap. ApJ, 812:126.

Chandrasekhar, S. (1960). Radiative transfer.

Clarke, C. J., Gendrin, A., and Sotomayor, M. (2001). The dispersal of circumstellar discs: the role of the ultraviolet switch. MNRAS, 328(2):485–491.

Courant, R., Friedrichs, K., and Lewy, H. (1928). Über die partiellen Differenzengleichungen der mathematischen Physik. Mathematische Annalen, 100:32–74.

Cuello, N. and Giuppone, C. A. (2019). Planet formation and stability in polar circumbinary discs. A&A, 628:A119.

Czekala, I., Chiang, E., Andrews, S. M., Jensen, E. L. N., Torres, G., Wilner, D. J., Stassun, K. G., and Macintosh, B. (2019). The Degree of Alignment between Circumbinary Disks and Their Binary Hosts. ApJ, 883(1):22.

D'Antona, F. and Mazzitelli, I. (1997). Evolution of low mass stars. Mem. Soc. Astron. Italiana, 68:807–822.

Dehnen, W. and Aly, H. (2012). Improving convergence in smoothed particle hydrodynamics simulations without pairing instability. MNRAS, 425(2):1068–1082.

Di Folco, E., Dutrey, A., Le Bouquin, J. B., Lacour, S., Berger, J. P., Köhler, R., Guilloteau, S., Piétu, V., Bary, J., Beck, T., Beust, H., and Pantin, E. (2014). GG Tauri: the fifth element. A&A, 565:L2.

Dong, R., Zhu, Z., Rafikov, R. R., and Stone, J. M. (2015). Observational Signatures of Planets in Protoplanetary Disks: Spiral Arms Observed in Scattered Light Imaging Can be Induced by Planets. ApJ, 809(1):L5.

Draine, B. T. (1988). The Discrete-Dipole Approximation and Its Application to Interstellar Graphite Grains. ApJ, 333:848.

Draine, B. T. (2003). Scattering by Interstellar Dust Grains. I. Optical and Ultraviolet. ApJ, 598(2):1017–1025.

Espaillat, C., Muzerolle, J., Najita, J., Andrews, S., Zhu, Z., Calvet, N., Kraus, S., Hashimoto, J., Kraus, A., and D'Alessio, P. (2014). An Observational Perspective of Transitional Disks. Protostars and Planets VI, pages 497–520.

Facchini, S., Juhász, A., and Lodato, G. (2018). Signatures of broken protoplanetary discs in scattered light and in sub-millimetre observations. MNRAS, 473(4):4459–4475.

Facchini, S., Lodato, G., and Price, D. J. (2013). Wave-like warp propagation in circumbinary discs - I. Analytic theory and numerical simulations. MNRAS, 433:2142–2156.

Fischer, O., Henning, T., and Yorke, H. W. (1994). Simulation of polarization maps. I. Protostellar envelopes. A&A, 284:187–209.

Fischer, O., Henning, T., and Yorke, H. W. (1996). Simulation of polarization maps. II. The circumstellar environment of pre-main sequence objects. A&A, 308:863–885.

Flaherty, K., Hughes, A. M., Simon, J. B., Qi, C., Bai, X.-N., Bulatek, A., Andrews, S. M., Wilner, D. J., and Kóspál, Á. (2020). Measuring Turbulent Motion in Planet-forming Disks with ALMA: A Detection around DM Tau and Nondetections around MWC 480 and V4046 Sgr. ApJ, 895(2):109.

Fukagawa, M., Tamura, M., Itoh, Y., Kudo, T., Imaeda, Y., Oasa, Y., Hayashi, S. S., and Hayashi, M. (2006). Near-Infrared Images of Protoplanetary Disk Surrounding HD 142527. ApJ, 636(2):L153–L156.

Fulk, D. A. and Quinn, D. W. (1996). An Analysis of 1-D Smoothed Particle Hydrodynamics Kernels. Journal of Computational Physics, 126(1):165–180.

Gaia Collaboration, Brown, A. G. A., Vallenari, A., Prusti, T., de Bruijne, J. H. J., Mignard, F., Drimmel, R., Babusiaux, C., Bailer-Jones, C. A. L., Bastian, U., and et al. (2016). Gaia Data Release 1. Summary of the astrometric, photometric, and survey properties. A&A, 595:A2.

Gammie, C. F. (1996). Layered Accretion in T Tauri Disks. ApJ, 457:355.

Garcia Lopez, R., Natta, A., Testi, L., and Habart, E. (2006). Accretion rates in Herbig Ae stars. A&A, 459(3):837–842.

Gingold, R. A. and Monaghan, J. J. (1977). Smoothed particle hydrodynamics - Theory and application to non-spherical stars. MNRAS, 181:375–389.

Gingold, R. A. and Monaghan, J. J. (1982). Kernel estimates as a basis for general particle methods in hydrodynamics. Journal of Computational Physics, 46:429–453.

Goldreich, P. and Tremaine, S. (1978). The excitation and evolution of density waves. ApJ, 222:850–858.

Goldreich, P. and Tremaine, S. (1979). The excitation of density waves at the Lindblad and corotation resonances by an external potential. ApJ, 233:857–871.

Goldreich, P. and Ward, W. R. (1973). The Formation of Planetesimals. ApJ, 183:1051–1062.

Gonzalez, J.-F., van der Plas, G., Pinte, C., Cuello, N., Nealon, R., Ménard, F., Revol, A., Rodet, L., Langlois, M., and Maire, A.-L. (2020). Spirals, shadows, and precession in HD 100453 - I. The orbit of the binary. MNRAS, 499(3):3837–3856.

Guilloteau, S., Dutrey, A., and Simon, M. (1999). GG Tauri: the ring world. A&A, 348:570–578.

Günther, R. and Kley, W. (2002). Circumbinary disk evolution. A&A, 387:550–559.

Henyey, L. G. and Greenstein, J. L. (1941). Diffuse radiation in the Galaxy. ApJ, 93:70–83.

Hirsh, K., Price, D. J., Gonzalez, J.-F., Ubeira-Gabellini, M. G., and Ragusa, E. (2020). On the cavity size in circumbinary discs. MNRAS, 498(2):2936–2947.

Hollenbach, D., Johnstone, D., Lizano, S., and Shu, F. (1994). Photoevaporation of Disks around Massive Stars and Application to Ultracompact H II Regions. ApJ, 428:654.

Hong, S. S. (1985). Henyey-Greenstein representation of the mean volume scattering phase function for zodiacal dust. A&A, 146(1):67–75.

Ireland, M. J. and Kraus, A. L. (2008). The Disk Around CoKu Tauri/4: Circumbinary, Not Transitional. ApJ, 678(1):L59.

Jeans, J. H. (1902). The Stability of a Spherical Nebula. Philosophical Transactions of the Royal Society of London Series A, 199:1–53.

Joy, A. H. (1945). T Tauri Variable Stars. ApJ, 102:168.

Kattawar, G. W. (1975). A three-parameter analytic phase function for multiple scattering calculations. J. Quant. Spectrosc. Radiative Transfer, 15:839–849.

Lacour, S., Biller, B., Cheetham, A., Greenbaum, A., Pearce, T., Marino, S., Tuthill, P., Pueyo, L., Mamajek, E. E., Girard, J. H., Sivaramakrishnan, A., Bonnefoy, M., Baraffe, I., Chauvin, G., Olofsson, J., Juhasz, A., Benisty, M., Pott, J. U., Sicilia-Aguilar, A., Henning, T., Cardwell, A., Goodsell, S., Graham, J. R., Hibon, P., Ingraham, P., Konopacky, Q., Macintosh, B., Oppenheimer, R., Perrin, M., Rantakyrö, F., Sadakuni, N., and Thomas, S. (2016). An M-dwarf star in the transition disk of Herbig HD 142527. Physical parameters and orbital elements. A&A, 590:A90.

Lada, C. J. and Wilking, B. A. (1984). The nature of the embedded population in the rho Ophiuchi dark cloud : mid-infrared observations. ApJ, 287:610–621.

Laibe, G. and Price, D. J. (2012). Dusty gas with smoothed particle hydrodynamics - I. Algorithm and test suite. MNRAS, 420:2345–2364.

Lattanzio, J. C. J., J., M., H., P., and M., S. (1986). Controlling penetration. SIAM Journal on Scientific and Statistical Computing, 7(2):591–598.

Lin, D. N. C. and Papaloizou, J. (1986). On the tidal interaction between protoplanets and the primordial solar nebula. II - Self-consistent nonlinear interaction. ApJ, 307:395–409.

Lodato, G. and Price, D. J. (2010). On the diffusive propagation of warps in thin accretion discs. MNRAS, 405:1212–1226.

Lucy, L. B. (1977). A numerical approach to the testing of the fission hypothesis. AJ, 82:1013–1024.

Lucy, L. B. (1999). Improved Monte Carlo techniques for the spectral synthesis of supernovae. A&A, 345:211–220.

Lynden-Bell, D. and Pringle, J. E. (1974). The evolution of viscous discs and the origin of the nebular variables. MNRAS, 168:603–637.

Mamajek, E. E. (2009). Initial Conditions of Planet Formation: Lifetimes of Primordial Disks. In Usuda, T., Tamura, M., and Ishii, M., editors, American Institute of Physics Conference Series, volume 1158 of American Institute of Physics Conference Series, pages 3–10.

Manara, C. F., Testi, L., Natta, A., Rosotti, G., Benisty, M., Ercolano, B., and Ricci, L. (2014). Gas content of transitional disks: a VLT/X-Shooter study of accretion and winds. A&A, 568:A18.

Marino, S., Perez, S., and Casassus, S. (2015). Shadows Cast by a Warp in the HD 142527 Protoplanetary Disk. ApJ, 798(2):L44.

Martin, R. G. and Lubow, S. H. (2018). Polar alignment of a protoplanetary disc around an eccentric binary - II. Effect of binary and disc parameters. MNRAS, 479(1):1297–1308.

Martin, R. G. and Lubow, S. H. (2019). Polar alignment of a protoplanetary disc around an eccentric binary - III. Effect of disc mass. MNRAS, 490(1):1332–1349.

Meru, F. and Bate, M. R. (2012). On the convergence of the critical cooling time-scale for the fragmentation of self-gravitating discs. MNRAS, 427(3):2022–2046.

Min, M., Hovenier, J. W., and de Koter, A. (2005). Modeling optical properties of cosmic dust grains using a distribution of hollow spheres. A&A, 432(3):909–920.

Min, M., Stolker, T., Dominik, C., and Benisty, M. (2017). Connecting the shadows: probing inner disk geometries using shadows in transitional disks. A&A, 604:L10.

Miranda, R. and Lai, D. (2015). Tidal truncation of inclined circumstellar and circumbinary discs in young stellar binaries. MNRAS, 452:2396–2409.

Miranda, R. and Rafikov, R. R. (2019). On the Planetary Interpretation of Multiple Gaps and Rings in Protoplanetary Disks Seen By ALMA. ApJ, 878(1):L9.

Mizuno, H. (1980). Formation of the Giant Planets. Progress of Theoretical Physics, 64(2):544–557.

Monaghan, J. J. (1992). Smoothed particle hydrodynamics. ARA&A, 30:543–574.

Monaghan, J. J. (1997). SPH and Riemann Solvers. Journal of Computational Physics, 136:298–307.

Monaghan, J. J. (2002). SPH compressible turbulence. MNRAS, 335:843–852.

Monaghan, J. J. (2005). Smoothed particle hydrodynamics. Reports on Progress in Physics, 68:1703–1759.

Monaghan, J. J. and Lattanzio, J. C. (1985). A refined particle method for astrophysical problems. A&A, 149:135–143.

Morris, J. P. and Monaghan, J. J. (1997). A Switch to Reduce SPH Viscosity. Journal of Computational Physics, 136(1):41–50.

Mulders, G. D. and Dominik, C. (2012). Probing the turbulent mixing strength in protoplanetary disks across the stellar mass range: no significant variations. A&A, 539:A9.

Muro-Arena, G. A., Benisty, M., Ginski, C., Dominik, C., Facchini, S., Villenave, M., van Boekel, R., Chauvin, G., Garufi, A., Henning, T., Janson, M., Keppler, M., Matter, A., Ménard, F., Stolker, T., Zurlo, A., Blanchard, P., Maurel, D., Moeller-Nilsson, O., Petit, C., Roux, A., Sevin, A., and Wildi, F. (2019). Shadowing and multiple rings in the protoplanetary disk of HD 139614. arXiv e-prints, page arXiv:1911.09612.

Muro-Arena, G. A., Ginski, C., Dominik, C., Benisty, M., Pinilla, P., Bohn, A. J., Moldenhauer, T., Kley, W., Harsono, D., Henning, T., van Holstein, R. G., Janson, M., Keppler, M., Ménard, F., Pérez, L. M., Stolker, T., Tazzari, M., Villenave, M., Zurlo, A., Petit, C., Rigal, F., Möller-Nilsson, O., Llored, M., Moulin, T., and Rabou, P. (2020). Spirals inside the millimeter cavity of transition disk SR 21. A&A, 636:L4.

Murray, N. (2011). Star Formation Efficiencies and Lifetimes of Giant Molecular Clouds in the Milky Way. ApJ, 729(2):133.

Mutter, M. M., Pierens, A., and Nelson, R. P. (2017). The role of disc self-gravity in circumbinary planet systems - I. Disc structure and evolution. MNRAS, 465(4):4735–4752.

Nagel, E., D'Alessio, P., Calvet, N., Espaillat, C., Sargent, B., Hernández, J., and Forrest, W. J. (2010). Wall Emission in Circumbinary Disks: the Case of Coku Tau/4. ApJ, 708(1):38–50.

Nealon, R., Cuello, N., Gonzalez, J.-F., van der Plas, G., Pinte, C., Alexander, R., Ménard, F., and Price, D. J. (2020). Spirals, shadows & precession in HD 100453 - II. The hidden companion. MNRAS, 499(3):3857–3867.

Nixon, C., King, A., and Price, D. (2013). Tearing up the disc: misaligned accretion on to a binary. MNRAS, 434(3):1946–1954.

Ogilvie, G. I. and Lubow, S. H. (2002). On the wake generated by a planet in a disc. MNRAS, 330(4):950–954.

Ohashi, N. (2008). Observational signature of planet formation: The ALMA view. Ap&SS, 313(1-3):101–107.

Owen, J. E. (2016). The Origin and Evolution of Transition Discs: Successes, Problems, and Open Questions. Publ. Astron. Soc. Australia, 33:e005.

Owen, J. E. and Clarke, C. J. (2012). Two populations of transition discs? MNRAS, 426:L96–L100.

Papaloizou, J. C. B. (2005). Global numerical simulations of differentially rotating disks with free eccentricity. A&A, 432(3):757–769.

Perez, S., Casassus, S., Ménard, F., Roman, P., van der Plas, G., Cieza, L., Pinte, C., Christiaens, V., and Hales, A. S. (2015). CO Gas Inside the Protoplanetary Disk Cavity in HD 142527: Disk Structure from ALMA. ApJ, 798(2):85.

Pierens, A., McNally, C. P., and Nelson, R. P. (2020). Hydrodynamical turbulence in eccentric circumbinary discs and its impact on the in situ formation of circumbinary planets. MNRAS, 496(3):2849–2867.

Pinte, C., Harries, T. J., Min, M., Watson, A. M., Dullemond, C. P., Woitke, P., Ménard, F., and Durán-Rojas, M. C. (2009). Benchmark problems for continuum radiative transfer. High optical depths, anisotropic scattering, and polarisation. A&A, 498(3):967–980.

Pinte, C., Ménard, F., Duchêne, G., and Bastien, P. (2006). Monte Carlo radiative transfer in protoplanetary disks. A&A, 459(3):797–804.

Pollack, J. B., Hubickyj, O., Bodenheimer, P., Lissauer, J. J., Podolak, M., and Greenzweig, Y. (1996). Formation of the Giant Planets by Concurrent Accretion of Solids and Gas. Icarus, 124(1):62–85.

Price, D. J. (2012). Smoothed particle hydrodynamics and magnetohydrodynamics. Journal of Computational Physics, 231:759–794.

Price, D. J., Cuello, N., Pinte, C., Mentiplay, D., Casassus, S., Christiaens, V., Kennedy, G. M., Cuadra, J., Sebastian Perez, M., Marino, S., Armitage, P. J., Zurlo, A., Juhasz, A., Ragusa, E., Laibe, G., and Lodato, G. (2018a). Circumbinary, not transitional: on the spiral arms, cavity, shadows, fast radial flows, streamers, and horseshoe in the HD 142527 disc. MNRAS, 477:1270–1284.

Price, D. J., Wurster, J., Tricco, T. S., Nixon, C., Toupin, S., Pettitt, A., Chan, C., Mentiplay, D., Laibe, G., Glover, S., Dobbs, C., Nealon, R., Liptai, D., Worpel, H., Bonnerot, C., Dipierro, G., Ballabio, G., Ragusa, E., Federrath, C., Iaconi, R., Reichardt, T., Forgan, D., Hutchison, M., Constantino, T., Ayliffe, B., Hirsh, K., and Lodato, G. (2018b). Phantom: A Smoothed Particle Hydrodynamics and Magnetohydrodynamics Code for Astrophysics. Publ. Astron. Soc. Australia, 35:e031.

Pringle, J. E. (1981). Accretion discs in astrophysics. ARA&A, 19:137–162.

Purcell, E. M. and Pennypacker, C. R. (1973). Scattering and Absorption of Light by Nonspherical Dielectric Grains. ApJ, 186:705–714.

Ragusa, E., Dipierro, G., Lodato, G., Laibe, G., and Price, D. J. (2017). On the origin of horseshoes in transitional discs. MNRAS, 464:1449–1455.

Ragusa, E., Fasano, D., Toci, C., Duchêne, G., Cuello, N., Villenave, M., van der Plas, G., Lodato, G., Ménard, F., Price, D. J., Pinte, C., Stapelfeldt, K., and Wolff, S. (2021). Circumbinary and circumstellar discs around the eccentric binary IRAS 04158+2805 - a testbed for binary-disc interaction. MNRAS, 507(1):1157–1174.

Rosswog, S. (2009). Astrophysical smooth particle hydrodynamics. New Astron. Rev., 53(4-6):78–104.

Rybicki, G. B. and Lightman, A. P. (1979). Radiative processes in astrophysics.

Schmidt, T. (1973). Elliptical Polarization by Light Scattering by Submicron Spheroids. In Greenberg, J. M. and van de Hulst, H. C., editors, Interstellar Dust and Related Topics, volume 52, page 131.

Schoenberg, I. J. (1946). Contributions to the problem of approximation of equidistant data by analytic functions. a. on the problem of smoothing or graduation – a 1st class of analytic approximation formulae. Quarterly of Applied Mathematics, 4(1):45–99.

Shakura, N. I. and Sunyaev, R. A. (1973). Black holes in binary systems. Observational appearance. A&A, 24:337–355.

Siess, L., Dufour, E., and Forestini, M. (2000). An internet server for pre-main sequence tracks of low- and intermediate-mass stars. A&A, 358:593–599.

Solc, M. (1989). Polarized light from circumstellar dust - Observations and models. Astronomische Nachrichten, 310(4):329–332.

Steinacker, J., Baes, M., and Gordon, K. D. (2013). Three-Dimensional Dust Radiative Transfer*. ARA&A, 51(1):63–104.

Thun, D., Kley, W., and Picogna, G. (2017). Circumbinary discs: Numerical and physical behaviour. A&A, 604:A102.

Toomre, A. (1964). On the gravitational stability of a disk of stars. ApJ, 139:1217–1238.

Ubeira Gabellini, M. G., Miotello, A., Facchini, S., Ragusa, E., Lodato, G., Testi, L., Benisty, M., Bruderer, S., T. Kurtovic, N., Andrews, S., Carpenter, J., Corder, S. A., Dipierro, G., Ercolano, B., Fedele, D., Guidi, G., Henning, T., Isella, A., Kwon, W.,

Linz, H., McClure, M., Perez, L., Ricci, L., Rosotti, G., Tazzari, M., and Wilner, D. (2019). A dust and gas cavity in the disc around CQ Tau revealed by ALMA. MNRAS, 486(4):4638–4654.

van der Marel, N., van Dishoeck, E. F., Bruderer, S., Andrews, S. M., Pontoppidan, K. M., Herczeg, G. J., van Kempen, T., and Miotello, A. (2016a). Resolved gas cavities in transitional disks inferred from CO isotopologs with ALMA. A&A, 585:A58.

van der Marel, N., van Dishoeck, E. F., Bruderer, S., Pérez, L., and Isella, A. (2015). Gas density drops inside dust cavities of transitional disks around young stars observed with ALMA. A&A, 579:A106.

van der Marel, N., Verhaar, B. W., van Terwisga, S., Merín, B., Herczeg, G., Ligterink, N. F. W., and van Dishoeck, E. F. (2016b). The (w)hole survey: An unbiased sample study of transition disk candidates based on Spitzer catalogs. A&A, 592:A126.

van der Marel, N., Williams, J. P., Ansdell, M., Manara, C. F., Miotello, A., Tazzari, M., Testi, L., Hogerheijde, M., Bruderer, S., van Terwisga, S. E., and van Dishoeck, E. F. (2018). New Insights into the Nature of Transition Disks from a Complete Disk Survey of the Lupus Star-forming Region. ApJ, 854(2):177.

Verlet, L. (1967). Computer "Experiments" on Classical Fluids. I. Thermodynamical Properties of Lennard-Jones Molecules. Physical Review, 159:98–103.

Von Neumann, J. and Richtmyer, R. D. (1950). A Method for the Numerical Calculation of Hydrodynamic Shocks. Journal of Applied Physics, 21(3):232–237.

Voronoï, G. (1908). Nouvelles applications des paramètres continus à la théorie des formes quadratiques. deuxième mémoire. recherches sur les parallélloèdres primitifs. Journal für die Reine und Angewandte Mathematik, 134:198–287.

Wendland, H. (1995). Piecewise polynomial, positive definite and compactly supported radial functions of minimal degree. Advances in Computational Mathematics, 4(1):389–396.

White, R. J., Ghez, A. M., Reid, I. N., and Schultz, G. (1999). A Test of Pre-Main-Sequence Evolutionary Models across the Stellar/Substellar Boundary Based on Spectra of the Young Quadruple GG Tauri. ApJ, 520(2):811–821.

Yu, S.-Y., Ho, L. C., and Zhu, Z. (2019). A Tight Relation between Spiral Arm Pitch Angle and Protoplanetary Disk Mass. ApJ, 877(2):100.